# The dynamical effects of the bar on the Galactic thin and thick disks

Monari, Giacomo

rijksuniversiteit
groningen

# The dynamical effects of the bar on the Galactic thin and thick disks

**Proefschrift**

ter verkrijging van de graad van doctor aan de
Rijksuniversiteit Groningen
op gezag van de
rector magnificus prof. dr. E. Sterken
en volgens besluit van het College voor Promoties.

De openbare verdediging zal plaatsvinden op

vrijdag 19 september 2014 om 12:45 uur

door

**Giacomo Monari**

geboren op 4 december 1984
te Porretta Terme, Italië

**Promotor**
Prof. dr. A. Helmi

**Copromotor**
Dr. M.T. Antoja Castelltort

**Beoordelingscommissie**
Prof. dr. P.C. van der Kruit
Prof. dr. K.H. Kuijken
Prof. dr. M.A.W. Verheijen

ISBN 978-90-367-7170-2
ISBN 978-90-367-7169-6 (electronic version)

This Thesis is dedicated to my Family
and to all those who financed it.

*Dem höchsten Gott allein zu Ehren,*
*Dem Nächsten draus sich zu belehren.*

*Would it have been worth while,*
*To have bitten off the matter with a smile,*
*To have squeezed the universe into a ball*
*To roll it toward some overwhelming question,*
*To say: "I am Lazarus, come from the dead,*
*Come back to tell you all, I shall tell you all"*

---

T.S. Eliot

# Contents

Chapter 1

# Introduction

*Est via sublimis, caelo manifesta sereno:*
*lactea nomen habet, candore notabilis ipso.*
*Hac iter est superis ad magni tecta Tonantis*
*regalemque domum.*

OVIDIUS

## 1.1 Historical notes on the Milky Way

The Sun and the Earth are part of the "Milky Way", our Galaxy. From Earth the Milky Way appears at night as a band of feeble light, delineating close to a great circle on the sky on which the stars and the planets that the human eye can distinguish are superimposed (Fig. 1.1).

The name "Milky Way" comes from the Western classical world, that used to associate constellations and asterisms to episodes of the Olympian mythology. According to the Latin author Hyginus (*De Astronomia*, Book 2), Greeks and Romans believed that the Milky Way was milk lavished from the breasts of the goddesses Hera/Juno or Rhea/Ops, shining between the stars[1]. Hence, the Greek name γαλαξιας (pr. *galaxias*, "milky one") and the Latin name *Via Lactea* ("milky way").

From the Greek world came also, for the first time, the idea that the Milky Way could be composed by distant and faint stars that the human eye cannot distinguish individually. In his treaty *Meteorologia*, Aristotle reports that this was indeed the idea of the philosophers Anaxagoras and Democritus. Aristotle instead associated the Milky Way to

> ... the ignition of the fiery exhalation of some stars which were large, numerous and close together ... [T]he ignition takes place in the upper part of the atmosphere, in the region of the world which is continuous with the heavenly motions (Aristotle, *Meteorologia*, 346b 11-12).

[1] The Milky Way is also described as the road to Mount Olympus, as in the opening quote of this Chapter.

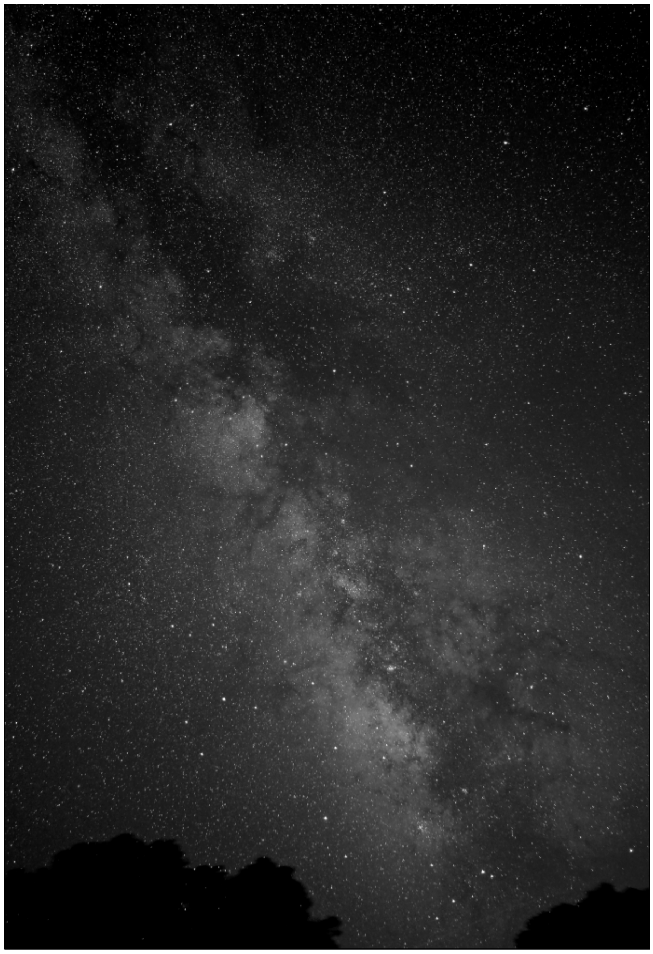

**Figure 1.1:** Milky Way on July 13, 2013 from Jadwin, Missouri. Credit: Victor Rogus. Courtesy: Victor Rogus.

Only much later, in the early Middle Ages, the hypothesis that the Milky Way could be composed by stars was reconsidered by analysts of Aristotle's work, in the Byzantine (e.g. Olympiodorus the Younger) and Islamic world (e.g. al-Bīrūnī and Avempace, see Montada 2012). In 1610 Galileo Galilei pointed his telescope to the Milky Way, and finally demonstrated that

> ... the galaxy is nothing else than a congeries of innumerable stars (Galilei, *Sidereus Nuncius*).

The astronomical use of the telescope, first introduced by Galileo, disclosed a Universe full of variety and unknowns. In the 17th, 18th and 19th century the construction of more powerful telescopes led astronomers (e.g., Charles Messier, William Herschel and Lord Rosse) to the discovery of new and mysterious objects in the sky: open and globular clusters, diffuse nebulae, elliptical and spiral "nebulae" (the latter distinction did not apply until 1845, when Lord Rosse discovered spiral structures in M51).

From the 17th century date also the first measurements of the photometric distances of stars[2], by astronomers such as Huygens and Newton (McCormmach 2012), which soon revealed the incredible vastness of the heavens (e.g., Newton estimated that the brightest stars are about 1 million times more distant from Earth than the Sun). To help with the interpretation of these discoveries came Isaac Newton's laws of mechanics and gravity (Newton 1687), already successful in describing the motion of the planets in the Solar System. These laws were believed to apply everywhere in the Universe. Newton himself believed that the stars were static, placed by God at immense distances or in such a way to balance exactly their gravitational attraction,

> ... lest the systems of the fixed stars should, by their gravity, fall on each other mutually (Newton 1687, *Naturalis Philosophiae Principia Mathematica*).

However his friend and colleague Edmund Halley discovered in 1718 a significant angular difference ("proper motion") between the position on the sky of the stars Sirius, Arcturus and Aldebaran and those recorded by the ancient Greek astronomer Hypparcus (Aitken 1942). The discovery of proper motions showed that the stars are not "fixed" on the sky, as it was previously believed, but they rather move relatively to each other.

The German philosopher Immanuel Kant was aware of these discoveries when in 1755 he wrote his treaty *Allgemeine Naturgeschichte und Theorie des Himmels*[3] (Universal Natural History and Theory of Heaven, inspired by Thomas Wright's earlier work). In this work Kant came to the impressive conclusion that

> ... [t]he shape of the heaven of fixed stars thus has no cause other than the same systematic arrangement on a grand scale as the cosmic structure of the planetary system on a small scale, since all the suns make up one system, whose common interconnecting plane is the Milky Way. Those which are the least related to this plane will be seen to the side; for that very reason, however, they are less dense, more widely scattered, and less frequent.

[2] The first measure of a star's distance using parallaxes was performed by Bessel (1838).

[3] Subtitle: *Versuch von der Verfassung und dem mechanischen Ursprunge des ganzen Weltgebäudes, nach Newtonischen Grundsätzen abgehandelt* (An Essay on the Constitution and the Mechanical Origin of the Entire Structure of the Universe Based on Newtonian Principles).

**Figure 1.2:** Map of the Milky Way derived by Herschel (1785).

> They are, so to speak, comets among the suns. (Kant 1755, *Allgemeine Naturgeschichte und Theorie des Himmels*).

In his view, this huge stellar system was kept together by gravitational forces and the stars were provided a net rotational motion, undetectable from Earth (because of the large distances and the time scales). Interestingly, in his hypothesis on the formation of the Solar System and the Milky Way, he imagined that both could have formed from a nebula flattened by its rotation and fragmented by gravity into single stars and planets. Finally, Kant noticed that a disk-like star structure, seen on the sky from great distance

> ... will appear in a small angle as a tiny and weakly lit area, with a circular shape if its plane is oriented directly in the line of sight and elliptical if it is viewed from the side (Kant 1755, *Allgemeine Naturgeschichte und Theorie des Himmels*).

Kant identified such structures with the nebular objects with elliptical shapes that were first discovered in the sky in those years. He proposed that they

> ... should be taken as [...] world systems and, so to speak, as Milky Ways (Kant 1755, *Allgemeine Naturgeschichte und Theorie des Himmels*),

i.e., he speculated that these were galaxies themselves, with similar structure and origin than the Milky Way (the "island universes" hypothesis). Evidence for the island universes hypothesis came first when astronomers were able to resolve single stars in the observed nebulae (observations of Lord Rosse, in the middle of 19th century) and then estimated for the first time their distances (Hubble 1925).

Herschel (1785) obtained the first determination of the Milky Way's structure. His method, dubbed "star gauging", consisted in the diligent counting of the number of stars in bins of apparent magnitude and in different directions on the sky. He then derived the star's distances assuming that all have the same absolute magnitude. This information was enough to obtain the Galaxy's 3D distribution and to draw the first Galactic map (Fig. 1.2). In Herschel's map the distribution of stars is indeed flattened (the ratio between the horizontal and vertical size is approximately 5 : 1) but the Sun is in the center, which, as we know now, is not correct.

An updated version of Herschel's map came at the beginning of the 20th century, with the work of Jacobus Kapteyn and collaborators (Kapteyn & van Rhijn 1920; Kapteyn 1922; see also van der Kruit & van Berkel 2001). Like Herschel, Kapteyn faced the "Sidereal Problem" (the determination of the distribution of stars in the Universe) by counting the number of stars of different brightness, this time on both the Northern and Southern hemispheres. He did this using the great technological advance of the

epoch, namely the astronomical use of photography. Photography and spectroscopy (the latter discovered by Father A. Secchi in the 1860s) allowed Kapteyn to complement his information with kinematic data, namely the proper motions and the line-of-sight velocities of the stars. In his derivation of the photometric distances of the stars he used a formula that accounted both for the magnitude and the proper motions of the stars. The premise of this formula is that, statistically speaking, stars following approximately a random velocity distribution have smaller proper motions if they are located farther away[4]. In the spatial and kinematical model resulting from Kapteyn's work ("Kapteyn's Universe"), the Milky Way looks like an oblate spheroid 100 times more dense in the center than at a distance $\sim 8.5$ kpc on the Galactic plane. As in Herschel's work, the Sun was located near to the center of the Galaxy and the axis ratio of the spheroid was approximately $5:1$. The main problem with Kapteyn's (and Herschel's) Universe was the unknown effect of light absorption due to the Milky Way's interstellar dust[5], so that the distance of obscured stars was overestimated and the Sun appeared to lie near the center of the Galaxy.

While studying the kinematics of stars in the Milky Way, Kapteyn (1905) found that the proper motion of the stars he observed were not completely random, but rather in two preferential directions. The behavior found by Kapteyn (and already noticed in smaller stellar samples before by Proctor, Kovalsky, Monck and Kobold; see van der Kruit & van Berkel 2001) was the discovery of Galactic rotation for stars the Solar Neighborhood, that was later formalized by Lindblad and Oort (see below). In the same years Schwarzschild (1907) suggested that the random velocities of the stars near the Sun were well described by a triaxial Gaussian[6].

At the end of the First World War, Harlow Shapley presented a completely different view of the Milky Way (Shapley 1917 and following papers), after detailed studies of the globular clusters carried out at Mount Wilson observatory. Shapley estimated the distance to several of the known globular clusters[7] and found these to concentrate at $\sim 15$ kpc, in the direction of the constellation of Sagittarius. Since he believed the globular clusters to be spherically distributed in the Milky Way (as they are not confined on the Galactic plane), he deduced that the concentration indicated the center of the Milky Way and that the Sun was located in the outskirts of the Galaxy (Binney & Merrifield 1998). Shapley's conclusions extended also to the interpretation of spiral nebulae. In his view, spiral nebulae had to be Galactic objects and not island universes for a number of reasons (Shapley & Shapley 1919), but mainly because their angular sizes implied an immense distance, if they were as large as he estimated the Milky Way to be. Instead the supporters of Kapteyn's Universe were generally accepting that spiral nebulae were extra-Galactic. This disagreement eventually led to the so-called "Great Debate" (Shapley & Curtis 1921).

During the 1920s, Bertil Lindblad and Jan Oort (Lindblad 1927; Oort 1927, 1928)

[4] Kapteyn previously also discovered a correlation between proper motions and spectral types of stars (Kapteyn 1892).

[5] Kapteyn actually knew obscuration effects, but only due to reddening (Binney & Merrifield 1998), which he estimated to be very modest in his observations (Kapteyn 1909).

[6] Still nowadays, Schwarzschild's distribution is used as the simplest approximation to describe the gross properties of the kinematics of disk stars, that are complicated in detail by the presence of stellar streams (Section 1.5.3).

[7] Shapley used the period-luminosity relation of RR Lyrae and W Virginis variable stars as a distance estimator. However he mistook the former class of stars in globular clusters with Classical Cepheids (Fernie 1969).

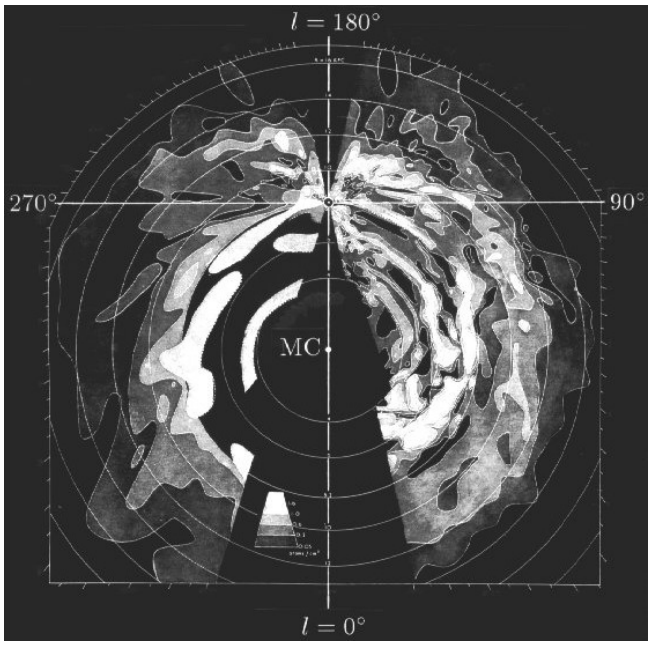


**Figure 1.3:** Distribution of HI in the Milky Way disk, inferred by Oort et al. (1958).

developed a complete theoretical model of the phase-space distribution of stars in the Milky Way, that accounted for the almost circular motion of the disk stars around the Galactic center. The observed kinematics of stars would be interpreted as a differential rotation around a center that was approximately corresponding, on the sky, with the center of the globular clusters found by Shapley. In particular, the expected velocity distribution of stars calculated relatively to the circular speed in a point of the Galaxy, was similar to a Schwarzschild's ellipsoid. However, the circular speed outer in the Galaxy is slower than inner: for this reason, an observer near the Sun measures two opposite streaming motions (Kapteyn's two "streams"), corresponding to stars moving inside or outside the position of the Sun in the Milky Way. Lindblad and Oort's estimate of the distance to the Galactic center was smaller than Shapley's ($\sim 6$ kpc), with an enclosed mass of at least $8 \times 10^{10} M_{\odot}$ (in order to support a circular velocity between 200 and 300 km s$^{-1}$).

However the interstellar absorption (discovered by Trumpler 1930) was still preventing a clear understanding of the large scale structure of the Milky Way. The situation improved after the discovery that the Milky Way radiates radio waves (Jansky 1933). In particular it was found that HI hydrogen emits in the 21 cm spectral line (van de Hulst 1945; Ewen & Purcell 1951), which is almost unaffected by absorption (Binney & Merrifield 1998). Thanks to this discovery, astronomers (Oort et al. 1958) produced the first map of the distribution of HI in the Milky Way, where it was possible to recognize the same spiral features observed in external nebulae (Fig. 1.3). The 21 cm line allowed also the first direct measurements of the circular speed $v_c$ of the Milky Way (Kwee et al.

1954), that appeared to be constant with $R$ across the Galaxy. These measurements, together with the discovery that the stars with the lowest metal abundances have more eccentric orbits (Sandage & Eggen 1959), influenced the first modern theories of Galactic formation (Eggen et al. 1962; Mestel 1963), as both $v_c$ and the kinematics of metal poor stars had to be predicted by the gravitational collapse models.

The increasing quality and resolution power of radio detectors (mostly due the development of interferometry) permitted the study of HI in external disk galaxies and their outskirts. The notorious result (Bosma 1978) was that the circular speed of HI did not decrease at large distances from the centers of the galaxies, as expected from the distribution of luminous matter, but rather it stayed constant. The rest of the mass necessary to produce such rotation was attributed to an unknown form of "dark matter" that interacts through gravitational forces but whose electromagnetic emission is undetectable[8]. This matter is expected to contribute to most of the mass of galaxies (and of course, also in the case of the Milky Way, see Section 1.2.3). What constitutes dark matter is still one of the greatest enigmas of Astronomy and Physics.

We come finally to the modern times and surveys. The technological advances, that allow nowadays to make use of e.g. infrared telescopes or high precision astrometry from space, are mostly responsible of our modern understanding of the Milky Way's structure. A special part of this Introduction (Section 1.4) is dedicated to the description of the modern surveys, which have led to a much more complete view of the Milky Way, and have revealed its great complexity. At the same time, the great discoveries in the field of Cosmology, require the models of formation and evolution of galaxies like the Milky Way to be inserted in a more general context (see Section 1.3).

## 1.2 The Structure of the Milky Way

### 1.2.1 The Galactic disks

The "Galactic disk" is the main stellar component of the Milky Way and it is roughly axisymmetric and extremely flattened on its midplane, the "Galactic plane". We can establish a cylindrical coordinate system $(R, \phi, z)$, with origin in the center of the Milky Way and $z$ perpendicular to the Galactic plane.

Assuming that the density of stars in the Milky Way is similar to that of external disk galaxies (Freeman 1970; van der Kruit & Searle 1981), we can describe the volume density of the Galactic disk $\rho(R, z)$ as a double exponential function of $R$ and $z$:

$$\rho(R, z) = \rho(0, 0) \mathrm{e}^{-R/R_\mathrm{d}} \mathrm{e}^{-|z|/z_\mathrm{d}}. \tag{1.1}$$

In external galaxies the vertical scale length $z_\mathrm{d}$ is almost constant over a large range of $R$ (van der Kruit & Searle 1981).

For stars younger than $\sim 4$ Gyr (Freeman 1991; Aumer & Binney 2009), each age population (i.e., the stars in age bins of $\sim 0.1$ Gyr, Quillen & Garnett 2000) can be best represented by Eq. (1.1) assuming a different $z_\mathrm{d}$ and $R_\mathrm{d}$ for each population. In particular, the older the stars the larger $z_\mathrm{d}$ (Binney & Tremaine 2008; for $R_\mathrm{d}$ the trend is more controversial). Some theoretical models (e.g., Saha et al. 2010) in part account

[8] This idea was already introduced by Zwicky (1937), while applying the virial theorem on the Coma cluster of galaxies.

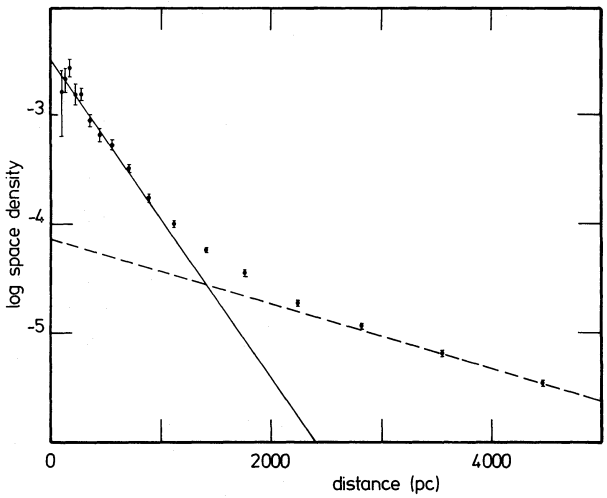


**Figure 1.4:** Density distribution for stars with $4 \leq M_V \leq 5$ as a function of distance from the Galactic plane. The solid line correspond to the thin disk fit and the dashed line to the thick disk. After Gilmore & Reid (1983). Courtesy: Gerry Gilmore.

for this phenomenon, as due to spiral arms and molecular clouds that gradually increase the vertical random velocities of disk stars. However very good fits can be obtained assuming that the *whole* disk density is the sum of only two components of the kind given by Eq. (1.1). These two components, called "thin disk" and "thick disk", have $z_\mathrm{d} \sim 300$ pc and $z_\mathrm{d} \sim 1$ kpc respectively (Gilmore & Reid 1983; see Fig. 1.4). The density of the thick disk is about 10% of that of the thin disk on the Galactic plane (Jurić et al. 2008). The value of $R_\mathrm{d}$ for both disks is poorly constrained, with values ranging from 2 to 4 kpc (e.g., Jurić et al. 2008; de Jong et al. 2010; Bovy et al. 2012d).

The thin and the thick disks also differ in their kinematics. The stars of the thin disk move on nearly circular orbits around the Galactic center. For example, near the Sun, the radial velocity dispersion of the oldest (i.e., hottest) thin disk stars is $\sim 50$ km s$^{-1}$ (Holmberg et al. 2007), only $\sim 20\%$ of the circular speed at the Sun (see Section 1.2.1.1). Although being still a system dominated by its rotation, the thick disk's kinematics have much larger random motions. For example Ojha et al. (1999) report $67 \pm 4$ km s$^{-1}$ for the thick disk radial velocity dispersions in the Solar Neighborhood, with a mean $v_\phi$ of $167 \pm 10$ km s$^{-1}$.

Finally, thin disk and thick disk stars also differ in their chemical composition and age. Thick disk stars have lower metallicities and higher abundances of $\alpha$ nuclides, a proxy for age (e.g., Fuhrmann 2011; see Fig. 1.5). Bensby et al. (2014) estimate that 70% of thin disk stars are younger than $\sim 7$ Gyr, while 70% of the thick disk stars are younger than $\sim 13$ Gyr. Whether the two disks are really physically distinct or not is still a matter of active research and debate. The separated chemical sequences seen in Fig. 1.5 would seem to support this view, however this idea was questioned by some groups (Schönrich & Binney 2009; Bovy et al. 2012b) that favor instead a more continuous sequence of

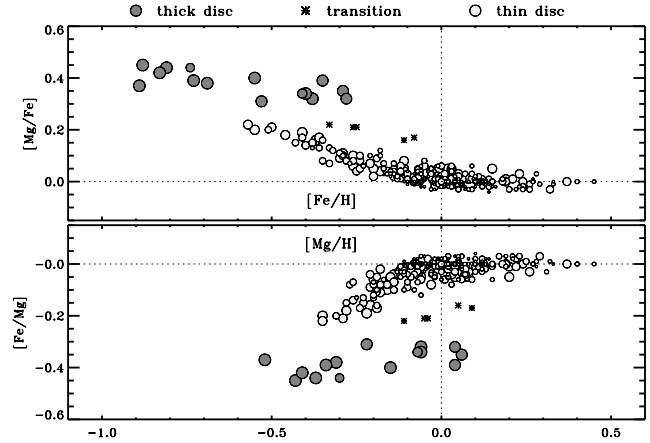


**Figure 1.5:** Abundance distribution of the thin and thick disks. After Fuhrmann (2011). Courtesy: Klaus Fuhrmann.

monoabundance subpopulations with increasing scale height when decreasing [Fe/H] and increasing [$\alpha$/H]. Very recent results (Recio-Blanco et al. 2014) seem to favor a clear separation in abundance space between thin and thick disk (as seen in Fig. 1.5).

#### 1.2.1.1 The Sun's position and velocity

The Sun's Galactocentric distance on the plane is $R_0$. The circular velocity of a star at radius $R$ in the Galactic plane is $v_c(R)$. The Local Standard of Rest (LSR) is an inertial reference frame centered on the Sun and traveling at speed $v_0 \equiv v_c(R_0)$ in the direction of Galactic rotation (Binney & Tremaine 2008). Constraints on the Sun's angular speed around the Galactic center are quite robust. They can be obtained directly, measuring the angular motion on the sky of the radio source Sgr A* (which is assumed to correspond to a black hole at rest in the center of the Milky Way; Reid & Brunthaler 2004), or indirectly, e.g. fitting models for the Galactic rotation to parallaxes and proper motions of water masers, whose orbits are estimated to be very circular (Reid et al. 2014). The angular speed of the Sun derived with these methods is $(v_0+V_\odot)/R_0 \simeq 30$ km s$^{-1}$ kpc$^{-1}$, with errors smaller than 0.5 km s$^{-1}$ kpc$^{-1}$ ($V_\odot$ is the tangential component of the Sun's peculiar velocity with respect of the LSR). However, $V_\odot$, $R_0$ and, in consequence $v_0$ are known with much less precision. Constraints on these parameters come from a variety of methods. The most recent determinations (e.g., Bovy et al. 2012a; Reid et al. 2014) place the Sun[9] at 8 kpc $\lesssim R_0 \lesssim$ 9 kpc and 210 km s$^{-1}$ $\lesssim v_0 \lesssim$ 250 km s$^{-1}$. Estimates of the Sun's peculiar motion $V_\odot$ range from 3 km s$^{-1}$ (Golubov et al. 2013, lower than the classical value of 5 km s$^{-1}$ derived by Dehnen & Binney 1998b from *Hipparcos*), to 12 km s$^{-1}$ (Schönrich et al. 2010), up to 24 km s$^{-1}$ (Bovy et al. 2012c).

[9] The distance of the Sun from the Galactic plane $z_0$ is somewhere between 5 and 30 pc (e.g., Majaess et al. 2009).

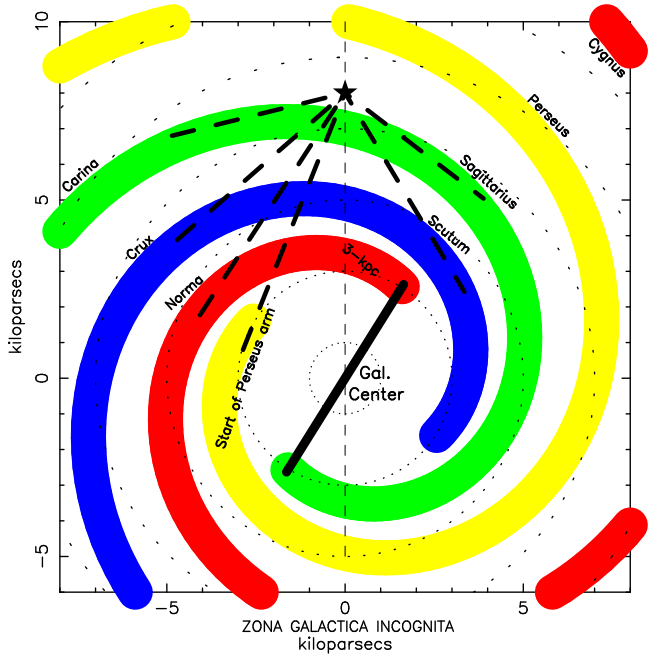


**Figure 1.6:** Two dimensional map of the Milky Way spiral arms, according to the mean cartographic model by Vallée (2014), summarizing observations of gas, dust and stars. The dashed lines show the arms tangents. "Zona Galactica Incognita" represents the part of the Galaxy that is not revealed by observations, because it lies beyond the bulge. Courtesy: Jacques Vallée.

#### 1.2.1.2 The spiral arms

As we mentioned above, the Galactic disk is only roughly axisymmetric. In reality, the disk contains spiral arms which are non-axisymmetric overdensities of gas and young stars with a filamentary appearance. Some of the spiral arms are also seen in the distribution of old stars (Drimmel & Spergel 2001; Churchwell et al. 2009). In fact, the spiral arms of the Milky Way have been observed in the radio 21 cm line of HI, giant HII regions, CO emission, infrared observations, optical data of young stars in clusters, water masers, etc. (for an exhaustive summary see Vallée 2008). For example, Cepheids, open clusters younger than 30 Myr and HII regions tend to be distributed along the so-called Sagittarius-Carina arm, the Orion-Cygnus arm and the Perseus arm (Lyngå 1987; Binney & Merrifield 1998). A schematic view of our current knowledge of the Milky Way spiral arms is depicted in Fig. 1.6.

Despite the efforts, the spiral arm properties, such as pattern speed, strength, orientation and even the number of arms or their stellar or gaseous structure, are not well known. Furthermore, the nature of the spiral arms themselves, i.e. their origin or their lifetime, are nowadays a matter of debate (Efremov 2011).

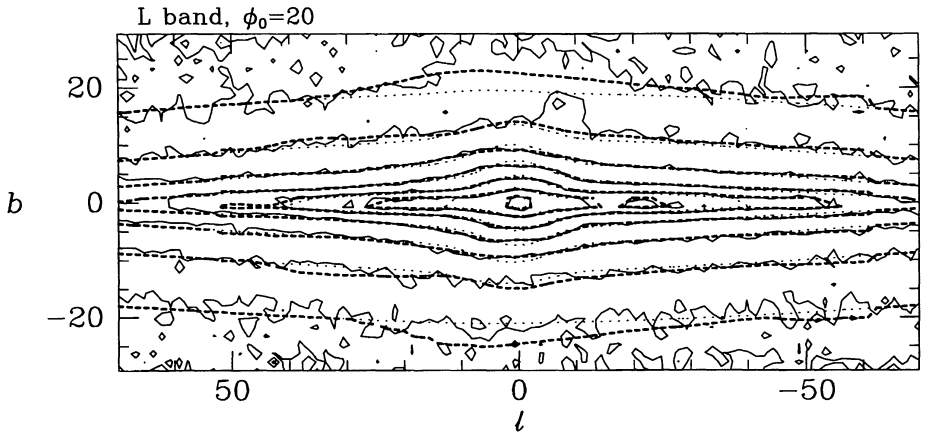


**Figure 1.7:** *L*-band *COBE* data corrected from absorption using the stellar luminosity models of Spergel et al. (1996). After Binney et al. 1997. Courtesy: James Binney.

### 1.2.2 The bulge/bar

The inner part of the Milky Way is occupied by a small (scale length $\sim 1$ kpc, Dehnen & Binney 1998a) and bulb-shaped stellar structure called "bulge". The bulge is thicker than the disk, and its kinematics are much hotter (velocity dispersion between 65 and 100 km s$^{-1}$ according to Ness et al. 2013). The bulge stars are also peculiar as they are $\alpha$-enhanced but relatively metal-rich. Bulge stars metallicities peak at about [M/H] $\sim -0.1$, with a sharp cutoff just above solar metallicity and a tail towards lower metallicity that does not appreciably extend below [M/H] $\sim -1.5$ (Zoccali et al. 2003).

Our knowledge of the bulge remains, to date, quite limited, as it is strongly obscured by the interstellar dust, except for few transparent "holes" (e.g., the notorious Baade's Window). Because of this, it is not clear whether the Galaxy has a significant "classical" bulge (resembling an elliptical galaxy; Renzini 1999). What seems clear is that the Galaxy has a "pseudobulge" (Kormendy & Kennicutt 2004), because it appears to be triaxial. Direct evidence of this comes from the study of the infrared sky in the direction of the Galactic center (Binney et al. 1997), microlensing (Zhao et al. 1996) and distribution of Red Clump stars (Stanek et al. 1994). For example, infrared data from the *COBE* satellite (Fig. 1.7) shows a clear asymmetry of the isophotes between $l < 0$ and $l > 0$, for $|l| < 20°$ (the "Galactic longitude" $l$ is equal to 0 at the Galactic center). This implies that much (if not all) of the bulge is a "bar", which is brighter and thicker at positive $l$ because that side is closer to the Sun (Binney & Tremaine 2008). The angle of the bar is still poorly constrained. Current determinations range between 15° and 45° from the line between the Galactic center and the Sun.

Models based on *COBE* data usually present the bar as a short triaxial system with principal axes of the bar approximately in the ratio $3 : 1 : 1$ (Stanek et al. 1994; Stanek 1995; Stanek et al. 1997; Bissantz & Gerhard 2002; López-Corredoira et al. 2005), extending to about 3.5 kpc from the center. However, in the last decade, star counts from new infrared data (*2MASS*, Skrutskie et al. 2006) suggest the existence of a second and

longer bar component, at higher longitudes ($l \sim 28°$; Hammersley et al. 2000; Benjamin et al. 2005; López-Corredoira et al. 2007; Cabrera-Lavers et al. 2007, 2008), with axes ratios about $4 : 0.5 : 0.1$. Therefore, it is still not clear if there is one dominant bar component, or if the Milky Way rather contains two bars. Martinez-Valpuesta & Gerhard (2011) attempted to unify the long and short bars with a dynamical $N$-body model, explaining that they are a single structure that is the result of secular evolution and buckling instability, and whose properties are consistent with observations.

### 1.2.3 The stellar halo and the dark matter halo

The Galactic disks are surrounded by a very extended (at least 50 kpc) cloud of stars and globular clusters forming the so-called "stellar halo". The stellar halo appears to be spheroidal, with the density usually described as decreasing with radius following a power-law (Morrison 1993) and contributing to only $\sim 1\%$ of the Milky Way total mass (Bell et al. 2008). The net rotation of halo stars, if any, is very slow (Fermani & Schönrich 2013). Moreover, the stars of the stellar halo are very old (Helmi 2008). Current cosmological models propose that the halo is formed by the debris of disrupted stellar systems (globular clusters and satellite galaxies) and there is increasing evidence that this may well be the case (e.g., Belokurov et al. 2006).

The existence of a dark matter component contributing to most of the mass of the Milky Way comes from the measurements e.g., of the total gravitational pull that satellite galaxies must experience to be bound to the Milky Way, or from the rotation curve of the Galaxy (e.g., Sofue 2012), which cannot be accounted for by the stellar mass present in the Milky Way. It is likely that dark matter is composed by elementary particles (Krauss 2011). Another possibility however is that Newton's law of gravity needs to be modified to account for the additional acceleration that stars and satellites experience as they orbit around the Milky Way (Famaey & McGaugh 2012).

## 1.3 The formation of the Milky Way disks

A reasonable modern description for the formation of galactic disks was put forward by Mo et al. (1998) (see also Fall & Efstathiou 1980). These authors considered the collapse of a spherical gas cloud embedded in a dark matter halo. Since the halo has some angular momentum, and if the gas conserves its angular momentum as it collapses, it spins up, leading to the formation of a gaseous cold disk in which star formation can proceed. This simple idea works relatively well in describing the properties of disk galaxies in a hierarchical Universe and is at the basis of most semi-analytic models of galaxy formation (Baugh 2006).

Nowadays computational power allows to actually simulate the formation of disk galaxies from first principles, where the aim is to reproduce the evolution of their stellar, gaseous and dark components at the same time. These simulations are useful both to test models and assumptions and to formulate predictions. Despite the progress since the first simulations (e.g., Katz & Gunn 1991), the problems are still many, as the challenge is to model simultaneously processes on the scales of 100 kpc to 10 Mpc (the growth of dark matter halos) down to the scales of star formation ($< 1$ pc, Mayer et al. 2008). Particularly delicate is the interplay between the stellar and gaseous components (and in particular the role of "feedback"), that has still to be solved with somewhat ad hoc

techniques (Scannapieco et al. 2012). Some authors (e.g., Agertz et al. 2011; Guedes et al. 2011; Martig et al. 2012; Stinson et al. 2013), with clever recipes for multiscale physics feedback processes, recently simulated galaxies similar to the Milky Way in some properties like the ratio between bulge and disk mass or scaling relations between mass and luminosity.

Some important and yet unanswered questions about the Milky Way formation are related to its chemical evolution e.g., why we observe radial and vertical abundance gradients in the Milky Way (Hayden et al. 2014)? Simulations of the chemical evolution of the Milky Way were performed by numerous authors, matching some of the observed properties (e.g., Kobayashi et al. 2007 reproduced the mass-metallicity relation, Tissera et al. 2012 the trends in abundances for the different components of the Milky Way and Minchev et al. 2013a the chemo-dynamical properties of the Solar Neighborhood). A related problem is how the star formation rate of the Milky Way evolved and can be mantained, given the current amount of gas. Current explanations involve cosmological gas accretion (Fraternali & Binney 2008) and "galactic fountains" (enriched hot gas expelled from the Galactic disk through supernovae explosions that cools down and falls back on the disk in the form of clouds, Marinacci et al. 2011; Marasco et al. 2012).

The main models for the formation of the thick disk can roughly be grouped in two categories:

- those where the thick disk is formed via an external agent and as a consequence of the cosmological formation of the Milky Way e.g., the disruption of accreted galaxies on co-planar orbits (Abadi et al. 2003), the vertical heating of a pre-existing disk through a minor merger, (Quinn et al. 1993; Kazantzidis et al. 2008; Villalobos & Helmi 2008) or as a consequence of a burst of star formation triggered during a merger (Brook et al. 2004);

- mechanisms that involve internal processes in the Milky Way, such as that the disk was born with larger velocity dispersions than what it has now (Bournaud et al. 2009) or the radial migration of stars through interactions with the spiral arms and bar, which preferentially moves outwards stars coming from the inner part of the Galaxy, with an intrinsically hotter vertical kinematics that is conserved during the migration (Schönrich & Binney 2009; Loebman et al. 2011; Minchev et al. 2013b).

The debate as to which one of these processes was more influential in the formation of the thick disk is still open. There are however recent constraints that disfavor some hypotheses e.g., the eccentricity distributions of orbits of stars in the thick disk is not compatible with it being fully accreted (Wilson et al. 2011); or the presence of distinct and well-separated chemical abundances sequences, as observed for the thin and thick disks, is not compatible with a process such as radial migration, which continuously acts to redistribute stars in the disk.

### 1.3.1 The formation of bar and spiral arms

Since Lindblad's work of the late 1920s, the main principle of the modern understanding of spiral arms and bars is that these features arise because of the gravitational forces and the particular displacement of orbits in the galactic disks (Binney & Tremaine 2008).

In particular, to date the consensus is that spiral arms are waves of star and gas density propagating in a differentially rotating disk (Lin & Shu 1964, 1966). They cannot

simply be an accumulation of material that moves on almost circular orbits ("material arms"), because otherwise, for $v_c(R) \sim$ const, they would wind up too fast if compared with the galactic timescales.

Lin and Shu's original idea was that the density waves forming spiral arms were stationary i.e., keeping the same characteristics, like amplitude and pattern speed, over very long times. However, it was shown (Toomre 1964; Goldreich & Lynden-Bell 1965) that disks can be very responsive to small disturbances and that spiral arms, even weak and *loosely wound*, can increase their amplitude dramatically, together with their trailing or leading appearance, in a self-induction process called "swing amplification", where the amplified arms are the trailing arms (that are therefore predicted to be more evident than leading arms in observations).

The longstanding debate about the nature of the spiral arms (also for the Milky Way) is still open. These could be long lived features with a defined pattern speed, as in the Lin and Shu theory (Bertin & Lin 1996), like some observations suggest (e.g., Feng et al. 2014). Or instead they could be transient, growing by swing amplification and then dissolving (thus requiring a continuous source of perturbation to keep existing in galaxies, e.g. the effect of tidal interactions or giant molecular clouds). All spiral structures formed in $N$-body simulations with cold and differentially rotating disks have been, so far, transient. Some of the most recent simulations show how the longevity of the transient spiral arms depends on the disk characteristics (D'Onghia et al. 2013) and how spiral arms can result from the superposition of few transient modes (Sellwood & Carlberg 2014). New theories on the spiral arm formation relate it also to the orbital structure induced by the bar ("invariant manifolds", Romero-Gómez et al. 2007). Finally recent simulations show how some transient spirals rotate at the same speed compared to the stellar disk (they are in practice material arms) and how stars migrate along these arms (Grand et al. 2014); the formation of such corotating spiral arms is influenced by the presence of a bar (Roca-Fàbrega et al. 2013).

The instability of disks to the formation of bars naturally arises in the framework of the swing amplification theory. Here bars can be considered as long lived modes, made by the superposition of leading and trailing waves (co-existing during the amplification process), forming a growing standing wave (Toomre 1981; Binney & Tremaine 2008; Sellwood 2014). A stronger interference to form the standing wave occurs when the amplitude of leading and trailing waves is similar. This mechanism and the ways to stabilize/inhibit the bar proposed by Toomre (1981) have been confirmed by several numerical works (e.g., Sellwood 1985; Sellwood & Moore 1999; Sellwood & Evans 2001). The formation of a bar-like non-axisymmetric mode induces orbits inside the corotation (the radius where the circular frequency of the Galaxy is equal to the pattern speed of the bar) that can be seen as the "skeleton" of the bar structure, as they are stretched in the direction of the long axis of the bar. Outside the corotation these orbits do not exist, and therefore the bar extends only inside corotation (Contopoulos & Papayannopoulos 1980).

The question that several modern studies try to answer is what can trigger processes like the bar instability in galaxies. For example, several studies of tidal interactions of satellite galaxies with disks have shown that often bar instability can be started by such encounters (e.g., Byrd et al. 1986; Noguchi 1987; Gerin et al. 1990; Salo 1991; Weinberg 1996; Mayer & Wadsley 2004; Romano-Díaz et al. 2008). Skibba et al. (2012) confirm that in the observations there seem to be an excess of bars to galaxies with a companion.

Another unanswered question concerns the evolution of the bar after its formation. As for the spiral arms, the longevity of the bar is also unknown and it could even be a recurrent phenomenon. For example, according to Bournaud et al. (2005) and Combes (2008), even though the formation and dissolution of a bar leaves a kinematically hot disk, therefore less responsive to perturbations, a new cold and responsive disk can be created if fresh gas is accreted and settles on circular orbits from which new stars can form. Particularly interesting are the mechanisms of evolution of the bar connected with the buckling instability (forming a peanut-shaped bulge; Athanassoula 2005; Martinez-Valpuesta & Gerhard 2011; Di Matteo et al. 2014), as they can explain more than one observed property of the Milky Way bar at the same time, such as the boxy shape and the second bar.

## 1.4 Recent surveys

We present below a short summary of some the most influential recent surveys of the stellar content of the Galactic disk over the past two decades. Because of the large number of surveys, we focus on those that we believe to be most relevant for the topics treated in this Thesis. Some of these surveys are not collecting data anymore, some others are not yet in activity but expected to influence strongly our understanding of the Milky Way. We choose to divide the surveys in three broad classes: astrometric satellites, imaging surveys and spectroscopic surveys.

### 1.4.1 Astrometric satellites

Astrometric surveys are dedicated to the precise measurement of the positions, parallaxes and proper motions of a large number of stars. Because of the precision that such measurements require, blurring of images due to the atmospheric turbulence can have an important effect and the use of satellites is preferred. Since the strength of these satellite missions is to measure the distances and transversal velocities of the stars, typically the measurements of the line-of-sight velocities have received a lower priority (and sometimes have been completely absent) but these are needed to complete the phase-space information. Therefore, spectroscopic follow-up surveys are often a necessary complement.

*Hipparcos* was a satellite launched in 1989, the first built explicitly for astrometric measurements. It operated for 3 years, collecting astrometry for $118,200$ stars with $V < 13$ and $\sim 1$ mas precision. The results of the *Hipparcos* mission were published in the *Hipparcos* Catalogue of parallaxes and proper motions (Perryman & ESA 1997), together with the less precise ($\sim 20 - 30$ mas) but larger *Tycho*-1 and *Tycho*-2 Catalogues. One of *Hipparcos* remarkable findings in the context of this Thesis is the first highly detailed map of the kinematics of the stars in the Solar Neighborhood (Fig. 1.8).

*Gaia* is a cornerstone astrometric space mission of ESA that was launched on 19 December 2013 and that is starting its 5 years operations while this Thesis is being written. *Gaia*'s data comprises all-sky absolute astrometry, broad-band $G(\simeq V)$ photometry and low-resolution spectro-photometry. Parallaxes will be measured with a standard error $< 10$ $\mu$as for stars brighter than $G < 12$, $< 25$ $\mu$as for $G < 15$ and 300 $\mu$as for $G = 20$ (de Bruijne 2012). For stars with $G < 17$ *Gaia* will also provide radial velocities with errors in the range $1 - 15$ km s$^{-1}$ and [M/H] with errors in the range $0.1 - 0.2$ dex. These stars will be approximately 400 million (Robin et al. 2012). The highly precise astrometry

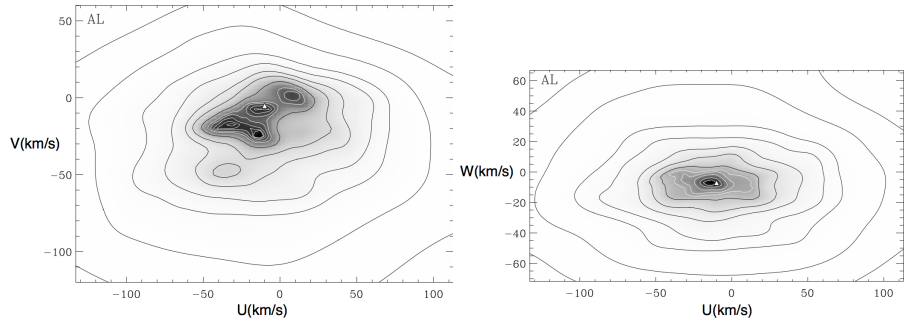


**Figure 1.8:** Velocity distribution of stars in the Solar Neighborhood from *Hipparcos*, in the $U$ vs. $V$ velocity plane (left) and in the $U$ vs. $W$ plane (right). After Dehnen (1998). Courtesy: Walter Dehnen.

from *Gaia* for a significant fraction of the Galaxy will provide an enormous improvement over the current data, and hence *Gaia* is expected to revolutionize our understanding of the Milky Way.

### 1.4.2 Imaging surveys

Imaging (ground based) surveys return the photometry and the distribution of stars on the sky (and, for multi-epoch surveys, their proper motions). From them we can derive photometric distances and sometimes abundance estimates. Therefore, the main aim of these surveys is to map the spatial distribution of stars in the Milky Way.

Amongst the imaging surveys and in the context of this Thesis it is worth mentioning *2MASS* (Skrutskie et al. 2006), the only near-infrared survey that has mapped the whole sky ($\sim$ 500 million stars). The near-infrared is almost free from interstellar absorption effects and *2MASS* was capable to unveil the distribution of luminous matter even on the Galactic plane, up to $\sim$ 10 kpc in distance from the Sun.

To some degree complementary to *2MASS* is the Sloan Digital Sky Survey (*SDSS*, York et al. 2000). This optical survey's main goal was the study of the extragalactic universe[10] and, in order to avoid the Galactic plane its footprint was restricted to Galactic latitudes $|b| > 30°$. Because of this, *SDSS* has had its greatest impact on our view of the Milky Way's "high latitude" components. For example, *SDSS* greatly improved our understanding the structure of the thick disk (Jurić et al. 2008) and offered the clearest picture of stellar streams in the Milky Way halo (thanks to the panoramic stellar maps, Belokurov et al. 2006).

Finally we mention here *SkyMapper* (Keller et al. 2007) that will provide Southern sky coverage in the optical down to magnitudes $g \leq 21$, and derive also metallicities and surface gravities (thanks to filters like the Strömgren system-like $u$ and the narrow $v$ at 4000 Å). This survey will be similar to *SDSS* with several improvements, including temporal coverage, more precise measurements of stellar properties because of the careful selection of photometric filters and coverage of large parts of the plane of the Galaxy.

[10] For example, *SDSS* produced a detailed map of the large scale structure up to redshift $z \sim 0.7$.

### 1.4.3 Spectroscopic surveys

The analysis of spectra of stars provides line-of-sight velocities, photospheric parameters and abundance determinations. Unfortunately, spectroscopy is a laborious and time-consuming enterprise. Moreover, multi-object spectroscopy with fibers requires these to be pointed. Therefore spectroscopic surveys can only target subsamples of the astrometric or and photometric surveys, completing their information in "follow-up" mode.

The Geneva-Copenhagen Survey (*GCS*, Nordström et al. 2004) collected for the first time an homogeneous sample of spectra in the Solar Neighborhood (inside $\sim$ 200 pc from the Sun). *GCS* included Strömgren photometry, line-of-sight velocities and [Fe/H] estimates for $\sim 14,000$ stars with *Hipparcos* astrometry. Together with *Hipparcos*, it has shaped much of our modern understanding of the kinematics of the Solar Neighborhood and moving groups (see Section 1.5.3).

The *RAVE* survey (Steinmetz et al. 2006) extended the spectroscopic studies beyond the Solar Neighborhood: it collected spectra in the CaII-triplet region for nearly $500,000$ (bright) stars in the Southern hemisphere, and has allowed the mapping of kinematics and elemental abundances for stars up to $\sim 2$ kpc from the Sun.

*SDSS* had also its spectroscopic follow-up: *SEGUE* (Yanny et al. 2009). With $\sim$ $350,000$ spectra *SEGUE* collected the largest sample of kinematic and abundance data for fainter stars in the high-latitude sky, with distance uncertainties on the single stars typically $\lesssim 10\%$ (Bovy et al. 2012c). It was used recently to model the thin and thick disks' scale heights and lengths (e.g., Bovy et al. 2012c; Bovy & Rix 2013).

The *ARGOS* survey (Freeman et al. 2013) has also become very influential in recent times for studies of the bulge/bar. In particular, one of its science cases is to understand the nature of the boxy shape of the Galactic bulge.

The *HERMES-GALAH* survey (Freeman 2012) is an Australian spectroscopic survey that has the ambition to measure the abundances of 30 elements for about a million of stars in the Galactic disk, down to $V \sim 14$.

A number of spectroscopic follow-up surveys are planned to be complementary to *Gaia*. In this context it is worth mentioning the *Gaia-ESO* survey (Gilmore et al. 2012) that is currently ongoing and its focus is on stellar evolution, clusters and formation of the Milky Way components, *4MOST* (de Jong 2011) that will study the inner part of the Galaxy, the halo and a fair fraction of the disk from the Southern hemisphere and *WEAVE* (Dalton et al. 2012) that will focus on the outer disk and halo from the Northern hemisphere.

## 1.5 Notions of Milky Way disk kinematics and dynamics

As mentioned earlier, disk stars follow nearly circular orbits but they also experience deviations driven by the spiral arms and bar. We will discuss separately how the motion in an axisymmetric flat system like the disk can be described, and then focus on what happens when the symmetry is broken and what are its imprints on the kinematics of disk stars.

### 1.5.1 Motions in an axisymmetric disk

Most of the stars in the Galactic disk rotate near its midplane on almost circular orbits. In the first instance, we can describe the Milky Way potential $\Phi(R,z)$ as roughly axisymmetric[11]. The equations of motion in such a potential read

$$\ddot{R} = -\frac{\partial \Phi_{\rm eff}}{\partial R}, \quad \dot{\phi} = \frac{L_z}{R^2}, \quad \ddot{z} = -\frac{\partial \Phi_{\rm eff}}{\partial z}, \tag{1.2}$$

where $\Phi_{\rm eff}(R,z) = \Phi(R,z) + L_z^2/(2R^2)$ and $L_z \equiv R^2\dot{\phi}$ is the angular momentum on the $z$ axis (a conserved quantity in this potential).

Unfortunately Eq. (1.2) does not have an analytic solution, except for a few simple potentials. However, when we describe the motion of stars near the Galactic plane and for orbits with low eccentricity, we can simplify the problem, following Lindblad's version of the epicyclic theory. In this case $\Phi_{\rm eff}$ can be conveniently expanded around $(R,z) = (R_{\rm g}, 0)$ as

$$\Phi_{\rm eff} = \Phi_{\rm eff}(R_{\rm g},0) + \frac{1}{2}\left(\frac{\partial^2 \Phi_{\rm eff}}{\partial R^2}\right)_{(R_{\rm g},0)} (R-R_{\rm g})^2 + \frac{1}{2}\left(\frac{\partial^2 \Phi_{\rm eff}}{\partial z^2}\right)_{(R_{\rm g},0)} z^2 + ..., \tag{1.3}$$

where $R_{\rm g} v_{\rm c}(R_{\rm g}) = L_z$ ($R_{\rm g}$ is the "guiding center radius") and the cross terms are null because the potential is assumed to be symmetric about $z = 0$. If we keep only the first two terms of Eq. (1.3), Eq. (1.2) become the equations of motion of two decoupled harmonic oscillators in $R$ and $z$:

$$\ddot{R} = -\kappa^2 (R - R_{\rm g}), \quad \ddot{z} = -\nu^2 z, \tag{1.4}$$

where

$$\kappa^2(R_{\rm g}) = \left(R\frac{{\rm d}\Omega^2}{{\rm d}R} + 4\Omega^2\right)_{R_{\rm g}}, \quad \nu^2(R_{\rm g}) = \left(\frac{\partial^2 \Phi_{\rm eff}}{\partial z^2}\right)_{(R_{\rm g},0)}. \tag{1.5}$$

$\Omega(R) = \sqrt{|\partial\Phi(R,0)/\partial R|\,/R}$ is the frequency of the circular orbit at $R$. Therefore, in this approximation the orbit consists of the superposition of the two decoupled harmonic motions at frequencies $\kappa(R_{\rm g})$ and $\nu(R_{\rm g})$, on a circular orbit with frequency $\Omega(R_{\rm g})$.

### 1.5.2 Resonances and non-axisymmetries

Non-axisymmetric perturbations representing the Galactic bar or spiral arms may be described by a potential $\Phi_{\rm b}(R,\phi,z) = U(R,z)\cos[m\phi - \Omega_{\rm b} t]$ (where $m$ is a positive integer and $\Omega_{\rm b}$ is the pattern speed of the perturbation) and affect especially certain locations in the Galaxy. These are the corotation radius $R_{\rm CR}$, where

$$\Omega(R_{\rm CR}) = \Omega_{\rm b}, \tag{1.6}$$

and the Lindblad Resonances radii, $R_{\rm OLR}$ and $R_{\rm ILR}$, where

$$m\,[\Omega(R_{\rm ILR}) - \Omega_{\rm b}] = \kappa(R_{\rm ILR}), \quad m\,[\Omega(R_{\rm OLR}) - \Omega_{\rm b}] = -\kappa(R_{\rm OLR}). \tag{1.7}$$

[11] We describe in detail what happens when the bar is added in Chapter 3, but note that for the Milky Way, this may simply be considered a small perturbation.

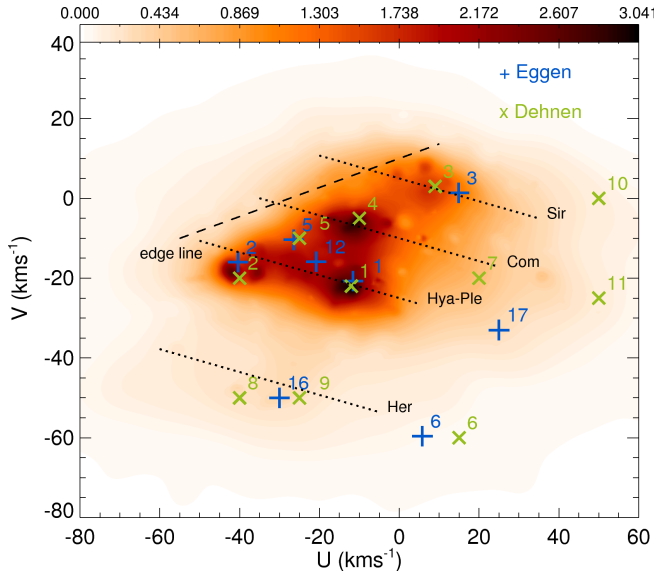


**Figure 1.9:** Moving groups in the $U$ vs. $V$ velocity plane of the Solar Neighborhood, resulting from a compilation of kinematic data for $\sim$ 24000 stars, mainly from *Hipparcos*, and the spectroscopic *Geneva-Copenhagen* and *CORAVEL* (Fehrenbach et al. 1987) surveys. After Antoja et al. (2008). Courtesy: Teresa Antoja.

In general, every time we have a resonance $l_R\Omega_R + l_\phi\left[\Omega_\phi - \Omega_\mathrm{b}\right] + l_z\Omega_z = 0$ (where $\Omega_R$, $\Omega_\phi$ and $\Omega_z$ are the radial, azimuthal and vertical frequencies in the axisymmetric background potential) the perturbation is more influential.

It is possible to show (Chapter 3 of this Thesis; Binney & Tremaine 2008, Section 3.3.3) that in the vicinity of the Lindblad Resonances of a bar, the effect of the perturbation is to stretch orbits, even of low eccentricity, in the direction parallel or perpendicular to the bar's long axis. Moreover, a significant number of orbits are trapped to the resonances and chaotic motions may also be present.

### 1.5.3 Moving groups

The velocity distribution of stars in the Solar Neighborhood is far from being smooth, but rather full of clumps and substructures, as can be seen from Fig. 1.9. The "moving groups" are groups of stars in the Milky Way that share similar kinematics and therefore appear clumped in velocity space. After the pioneering work of Olin Eggen (1960s - 1990s), *Hipparcos* gave the first clear picture of the moving groups present in the Solar Neighborhood (Dehnen 1998).

The classical hypothesis on the formation of moving groups is that they stem from the disruption of clusters by the Galactic differential rotation that, neglecting the cluster's self-gravity, spreads the stars in space but not in velocity[12] may well be the case for

[12] This is a consequence of the conservation of the density of stars along the trajectories in phase-space,

some stellar streams, or some parts of them. For example, part of Pleiades and Hyades moving groups are notorious open clusters, coherent in spacial distribution, kinematics, abundances and even easily recognizable on the sky. However, especially after spectroscopic follow-ups of *Hipparcos*, it was possible to recognize (Famaey et al. 2005; Bensby et al. 2007; Pompéia et al. 2011) that several moving groups were formed by stars with a large spread of ages and abundances, therefore making it unlikely that they could be disrupted open clusters. The hypothesis that some moving groups could have a purely dynamical origin has therefore to be taken in consideration.

Kalnajs (1991) proposed for the first time a dynamical model where the moving groups were formed by resonant effects of the non-axisymmetric components of the Milky Way. In particular he explained the formation of the Hyades and Sirius groups as a consequence of the Sun being near the Outer Lindblad Resonance of the Galactic bar, where the orbits are stretched in different directions from the bar gravitational forces (Chapter 3). Later Weinberg (1994), using analytic methods, showed that the bar can cause a clear signature on the Milky Way kinematics (average, dispersion), without focusing on the formation of moving groups. However, the result that triggered most significantly the interest of authors for the search of dynamical models that explained the moving groups in the Solar Neighborhood, was the success in explaining the Hercules moving group. The Hercules moving group is a group of stars that move outwards in the Galaxy and that had been already identified by Eggen (1958) and Blaauw (1970). Dehnen (2000) and Fux (2001), by means of simple simulations of the Milky Way disk, demonstrated that, assuming reasonable parameters for the Galactic bar, this can account for the formation of Hercules. Following this work other authors have attempted to describe also the other moving groups with the resonant effects of the bar, of the spiral arms, or both (De Simone et al. 2004; Quillen & Minchev 2005; Antoja et al. 2009, 2011), with alternate success.

Together with internal mechanisms, like resonant interactions and disruption of open clusters, there are other hypothesis for the formation of moving groups, especially in the thick disk. In fact, the origin of some moving groups could be external. Helmi & White (1999) have shown how disrupted satellites in the Milky Way potential and their tidal streams (Majewski 2002) are expected to leave imprints in the kinematics of stars in the Galaxy, especially in the halo, detectable also in the Solar Neighborhood. These imprints look similar to the classical moving groups, even if they usually have large velocities relative to the LSR and hence they are unlikely to be confused with the cold thin disk moving groups. The Arcturus group (a group that would generally be associated to the thick disk because of its kinematics and chemistry) lags considerably the LSR velocity and was interpreted as the remnant of an accretion event (Navarro et al. 2004), and other streams were identified in the existing catalogs (Newberg et al. 2002; Dinescu 2002; Helmi et al. 2006).

Finally, a new explanation for some of the moving groups has been presented recently. They could be kinematic manifestations of a phase-space distribution of stars unrelaxed in the Milky Way potential. Minchev et al. (2009) have shown that the evolution of such unrelaxed distribution (caused for example by an external perturbation) can create arc-shaped kinematic overdensities lagging the Sun's rotation and that could explain the Arcturus moving group. Quillen et al. (2009) have shown that also the perturbation by

described by Boltzmann's equation (Binney & Tremaine 2008). Since the Galactic gravitational tidal field leads to the cluster stars to spread out in space these will clump more and more in velocity space.

a satellite in an eccentric orbit can induce stellar streams on the disk.

## 1.6 This Thesis

In this Thesis we study the effects of the Galactic bar on the kinematics and orbital structure of the thin and thick disks of the Milky Way. The goal of this research is to establish if moving groups in the hotter and thicker disk components of the Milky Way can arise from internal mechanisms. In particular we wish to characterize the amount of resonant trapping and relation to kinematic substructures induced by the Galactic bar. This characterization is motivated by our desire to disentangle such substructures from those arising from accretion events. The largest difference with respect to previous works is a full 3D treatment of the problem, with numerical models that include also a representation of the Milky Way thick disk.

In Chapter 2 we perform test particle numerical simulations of the thin and thick disks in a 3D Galactic potential including a dark halo, a bulge, thin and thick disks, and a Ferrers bar. The resulting velocity distributions of populations corresponding to both disks are analyzed for different positions in the Galaxy and for different structural parameters of the bar. We find that the velocity distributions of both thin and thick disk are significantly affected by the bar and that it is possible to trace the imprints of the bar also vertically and at least up to $z \sim 1$ kpc for the thin disk and $z \sim 2$ kpc for the thick disk, for stars in the (extended) Solar Neighborhood.

As briefly discussed earlier in this Introduction, the non-axisymmetric components of the Milky Way, like the bar and the spiral arms, perturb the Galactic potential and induce trapping near the resonances. In the immediate neighborhood of resonances one often finds chaotic orbits. In Chapter 3 we analyze the amount of resonant trapping and chaotic motion induced by the bar onto the Galactic disks. We first approach the problem analytically and use simple 2D models with a flat circular velocity curve and a quadrupole bar. This allows us to perform a first order perturbation analysis and to study the regions of the velocity space where resonant trapping may be expected and to get insight into the dynamics of the problem. We then analyze the 3D simulations presented in Chapter 2, which allows us to study what happens to both thin and thick disks in a more complex gravitational potential. In this case we quantify the amount of resonant trapping through a Fourier analysis of the orbits of the particles in the simulations, that is by determining the basic frequencies. We study the amount of trapping per orbital family, as a function of $R$, $\phi$ and $z$, and how the trapped orbits are associated to groups and features in the particles' velocity distributions. For our default bar model, we find that roughly 16% of orbits are trapped to resonances in our simulations and that they create features in velocity space. The fraction of orbits trapped to horizontal ($\Omega_R : \Omega_\phi = n : m$) resonances and their characteristics do not depend on height above the Galactic plane but rather on the angle from the bar and distance from the Galactic center. The fraction of orbits trapped to the vertical resonances ($\Omega_R : \Omega_z = n : m$, $\Omega_\phi : \Omega_z = n' : m'$) instead grows as the height above the Galactic plane increases. We explore two additional bar models and find that the main difference resides in the number of trapped and irregular orbits, and this is directly related to the strength of the perturbation.

If we compare our findings in 3D with the predictions of the 2D model on the Galactic plane, we find qualitatively similar results for the position of the trapped orbits on the velocity plane as a function of the angle from the Galactic bar and distance from the Galactic center.

In Chapter 4 we propose a new explanation for the recent discovery (Siebert et al. 2011a; Williams et al. 2013) of a negative $R$ gradient of the (galactocentric) radial velocity $v_R$ of the stars of the Milky Way in the neighborhood of the Sun. We compare the results of test particle simulations of the Milky Way presented in Chapter 2 with observations from the *RAVE* survey. To this end we apply the *RAVE* selection function to the simulations, and convolve these with the characteristic *RAVE* errors. We explore different positions relative to the bar in the simulations as well as different bar models.

We find that the bar induces a negative radial velocity gradient even high from the Galactic plane, outside the Outer Lindblad Resonance, and for angles from the long axis of the bar compatible with the current estimates. The *RAVE* selection function and typical errors do not wash away the gradient, but often make it steeper, especially near the Galactic plane. The value for the $v_R$ gradient that we find for our default bar model varies from $-4$ km s$^{-1}$ kpc$^{-1}$ to $-1.5$ km s$^{-1}$ kpc$^{-1}$ depending on height from the Galactic plane. These values are similar to the average value found in *RAVE*, but they are too shallow if we consider only stars at certain heights. No gradient in the vertical velocity is present in our simulations, from which we may conclude that the observed gradient is unlikely to have been induced by the bar.

## 1.7 Conclusions and future work

The most important result of this Thesis work is that the Galactic bar is expected to have a significant impact on the kinematics of both thin and thick disks, even far away from the Galactic midplane. Our analysis shows that the bar affects the velocity distribution of stars in the radial and azimuthal directions, while it leaves no signature on the distribution of vertical velocities in our models.

For stars near the Sun, the strongest manifestation of the bar is due to the Outer Lindblad Resonance. This resonance splits the velocity distribution in two main modes (OLR and LSR Mode), and traps, in the models that we explored, $\sim 14\%$ of the orbits. A large fraction of these orbits define an easily recognizable horn-like feature in the LSR Mode which is associated to the $\Omega_R : \Omega_\phi = 2 : 1$ resonance. The average velocity of the orbits that form the OLR Mode and Horn may point inwards or outwards in the Galaxy depending on the angle from the bar. Their net rotational velocity depends instead on the distance from the center of the Galaxy and on the height from the Galactic plane.

Our work implies that these features should be recognizable also in the thick disk. Indeed, if we analyze the velocity distribution of stars in the Milky Way thick disk (e.g., using the *RAVE* survey data, Fig. 1.10), these features are apparent, where the OLR Mode is coincident with the Hercules moving group ($(v_R, v_\phi) \sim (-25, 230)$ km s$^{-1}$ in Fig. 1.10) and the Horn is visible at $(v_R, v_\phi) \sim (75, 230)$ km s$^{-1}$.

In the future it could be possible to use both the Hercules moving group and the Horn-like distortion to obtain a stronger constraint on the properties of the bar, possibly more sensitive than the measurements obtained to date using only Hercules (e.g., Antoja

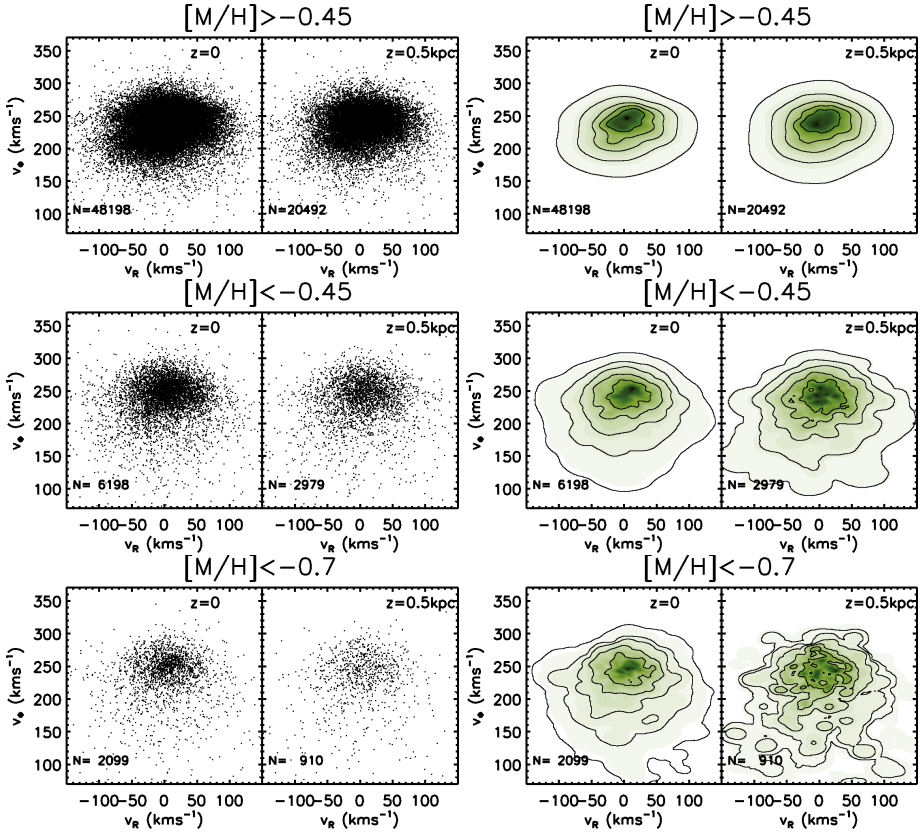


**Figure 1.10:** $v_R$ vs. $v_\phi$ distribution of disk stars from the *RAVE* survey (DR4) inside cylindrical volumes of radius 300 pc and height 600 pc, centered at $X = 0$, $Y = 0$ and $|Z| = 0, 0.5$ kpc. Top row: stars with [M/H] $> -0.45$. Center row: stars with [M/H] $< -0.45$. Bottom row: stars with [M/H] $< -0.7$. Right panels: density distribution obtained from the same kernel estimator used in Chapter 2. The selection of stars with [M/H] $< -0.45$ and especially [M/H] $< -0.7$ tries to maximize proportion of thick disk stars, while [M/H] $> -0.45$ likely is more representative of the thin disk population.

et al. 2014). Assuming that with better data quality it would be easier to tag the stars belonging to Hercules/OLR Mode and to the Horn-like distortion, one could compute the frequencies and the guiding center radii $R_g$ for stars in different small volumes of the Galaxy for a variety of potentials including a bar component. In the best fit model the Hercules/OLR Mode would be formed only by stars with $R_g < R_{OLR}$, and the Horn-like feature only by stars trapped to the Outer Lindblad Resonance (see Chapter 3). The more volumes where we can trace the features, the better the constraint. Moreover, it could be possible to relate the rotational velocity of these features with the height of the stars above the Galactic plane, obtaining therefore also a constraint on the vertical variation of the Milky Way potential.

The method just outlined would require the identification of features induced by the bar in the velocity distribution of stars in the Milky Way disks, and to tag the associated stars. However, this identification might be difficult for low quality data. In that case it could be easier to obtain a constraint using the moments of the velocity distribution of stars inside small volumes in the Galaxy. It is possible to write down analytic expressions for the average velocity (and higher moments) stars at different positions in the Galaxy, depending on the bar potential characteristic parameters (Kuijken & Tremaine 1991). In this case, the best fit model would match the average velocity of stars at different positions in the Galaxy. For example, the best fit model would have to match the negative gradient of average radial velocity measured by the *RAVE* survey and discussed in Chapter 4, and the oscillations with angle that we discuss in Chapters 2 and 3. The recent finding by Faure et al. (2014) that the effects induced by spiral arms are quantitatively consistent with the observed velocity gradients in the Solar Neighborhood should also be taken into account. In fact, a proper model for the velocity moments at different locations of the Milky Way disks should consider both bar and spiral arms. Naturally, the increase in free parameters in the models has to go together with an improvement in the quality of the data, to break the degeneracies. In this sense, the *Gaia* mission constitutes the great hope of the Milky Way modelers, because of the extent and quality of the data, together with the full phase-space information that will be available for many stars.

Another important point is that the effects induced by the bar can create biases in the estimates of the fundamental Galactic parameters, like the LSR velocity and the peculiar motion of the Sun. In fact, most of the measurements of these parameters have been done so far by fitting axisymmetric models to the data and assuming that the residuals are due to the non axisymmetric features (Bovy et al. 2012a). However, the risk with this procedure is to include non-axisymmetric features (e.g., the Hyades and Hercules moving groups) in a fit with the axisymmetric model. We believe, therefore, that good measurements of such fundamental parameters have to be done taking in account the non-axisymmetric features in the models, for example by extending the asymmetric drift relation to include higher order terms (e.g., Kuijken & Tremaine 1991).

Finally, kinematic substructures in the thick disk have been in most cases associated with external causes, like accretion events. Instead, we show in this Thesis that internal mechanisms (like the effect of the non-axisymmetric components) as a cause of kinematic substructure in the thick disk cannot be ruled out. However, the effects of the bar that we find in our study consist more in distortions of the velocity distribution than in well separated overdensities. Furthermore, most of these features are asymmetric in $v_R$ because of the location of the Solar Neighborhood with respect to the bar. This is not usually the case for accreted streams, that tend to have a symmetric appearance in $v_R$

(especially if well mixed) and become visible as overdensities in regions of the velocity space that are typically less populated by disk stars. In conclusion this work hints at a way to disentangle the Galactic or extra-Galactic origin of kinematic substructure in the thick disk. Such a task is of crucial importance, since the census of accretion events in the Milky Way has important implications for our understanding of the formation of the Galaxy in a cosmological context.

Chapter 2

# 3D test particle simulations of the Galactic disks I. The kinematical effects of the bar.

Based on Monari, Antoja & Helmi (2013).
Submitted to A&A, arXiv:1306.2632.

## Abstract

We study the imprints of a rotating bar on the kinematics of stars in the thin and thick disks throughout the Galaxy.

We perform test particle numerical simulations of the thin and thick disks in a 3D Galactic potential that includes a halo, a bulge, thin and thick disks, and a Ferrers bar. We analyze the resulting velocity distributions of populations corresponding to both disks, for different positions in the Galaxy and for different structural parameters of the bar.

We find that the velocity distributions of the disks are affected by the bar, and that strong transient effects are present for approximately 10 bar rotations after this is introduced smoothly in time. On long (more realistic) timescales, the effects of the bar are strong on the kinematics of thin disk stars, and weaker on those in the thick disk, but in any case significant. Furthermore, we find that it is possible to trace the imprints of the bar also vertically and at least up to $z \sim 1$ kpc for the thin disk and $z \sim 2$ kpc for the thick disk.

## 2.1 Introduction

The study of kinematic groups in the Solar Neighborhood dates back to the work of Proctor (1869) and Kapteyn (1905), with the discovery of the Hyades and Ursa Major groups. In modern times, the analysis of *Hipparcos* data and other surveys (Dehnen 1998; Famaey et al. 2005; Antoja et al. 2008) revealed the presence of many other local kinematic structures with varying properties, some of which are composed by stars of a wide range of age. More recently, Antoja et al. (2012) using *RAVE* data demonstrated that some of the known local kinematical groups extend beyond the Solar Neighborhood at least as far as $\sim 1$ kpc from the Sun on the plane, and $\sim 0.7$ kpc below it.

These main kinematic groups are in the thin disk. Their spread in age and metallicity indicates that they are unlikely to be remnants of disrupted clusters (Eggen 1996). However, they can be explained in terms of the influence of the non-axisymmetric components of the Galaxy (bar and spiral arms) on the orbits of stars (Dehnen 2000; Fux 2001; De Simone et al. 2004; Quillen & Minchev 2005; Antoja et al. 2009, 2011). For instance, the existence of the Hercules stream, a local group of stars moving outwards in the disk and lagging the circular rotation, has been related to the bar's Outer Lindblad Resonance (Dehnen 2000).

On the other hand, much of the past work on the kinematics of the thick disk has explored the presence of phase-space substructure due to minor mergers and accretion events (Helmi et al. 2006; Villalobos & Helmi 2008, 2009). For example it has been suggested that the Arcturus stream (Eggen 1971) may have an extra-Galactic origin (Navarro et al. 2004). However, it has also been advocated that this stream could have a Galactic origin (Williams et al. 2009; Minchev et al. 2009), and be a signature of a bar's resonance (Antoja et al. 2009; Gardner & Flynn 2010). Yet this proposal may be considered somewhat speculative, as it is based on simulations of the kinematics on the plane of the Galaxy, that is ignoring the vertical motion, and it is a priori not so clear whether a resonance could affect stars of the thick disk that spend so much time far from the Galactic plane.

We thus currently have a limited understanding as to whether the non-axisymmetric components (bar and spiral arms) can induce kinematic structure in the thick disk, and how to distinguish this from the substructures associated to accretion events. It is only recently that Solway et al. (2012), using controlled N-Body simulations to study radial migration, quantified that transient spiral arms can change the angular momentum of stars in the thick disk almost as much as they do in the thin disk.

The main motivation of this Chapter is to study the influence of the Galactic bar on the thin and thick disk in 3D, paying special attention to the vertical dimension. Our final aim is to establish if kinematic groups or other signatures of the bar may be present far from the Galactic plane, that is for orbits with large vertical oscillations, both in the thin and thick disk. To this end, we perform controlled test particle orbit integrations in a Galactic potential that includes a bar. Our simulations present a number of improvements with respect to previous studies, mainly that the integrations are done in a potential that is 3D, and that we study both the thin and thick disks.

In Sect. 2.2 we give details of the simulation techniques and choice of initial conditions. In Sect. 2.3 we analyze the resulting velocity distributions of the thin and thick disks in localized volumes around the Sun, both in the Galactic plane as well as away from it. In Sect. 2.4 we present the implications of our results and our conclusions.

## 2.2 Simulation methods

Our approach to study the characteristics of the velocity distribution across the Galaxy is based on a "forward integration technique". First we make discrete realizations of specific distribution functions, then we integrate these initial conditions forward in time, using an adaptive sizestep Bulirsch-Stoer (Press et al. 1992). Finally we analyze the resulting coarse grained distribution inside finite volumes.

This approach may be contrasted to the "backward integration technique" (e.g., Dehnen 2000; Gardner & Flynn 2010)[1], where the velocity distribution at a single point in configuration space is obtained. Our method instead requires a large number of particles and is computationally more expensive, but it may be considered more realistic in reproducing how the phase-space is populated and is possibly more appropriate for comparison to the observations, which always probe a finite volume.

All the particles of our simulations are integrated in a potential composed by two parts: an axisymmetric part (formed by a bulge, a thin disk, a thick disk and a dark halo) and a non-axisymmetric part (the bar). The bar is introduced in the potential gradually with time and replaces the bulge. The mass of the bulge is continuously transferred to the bar, and becomes null when the bar has grown completely, so that the total mass of the system remains unchanged (see details in Sect. 2.2.2).

Here and in the rest of the Chapter $r$ and $R$ are the Galactocentric spherical and cylindrical radial coordinate respectively, $\phi$ is the polar angle measured from the long axis of the bar in the direction of Galactic rotation, and $z$ the vertical coordinate. Moreover, $v_R \equiv -\dot{R}$ is the radial Galactocentric velocity (positive towards the center of the Galaxy), $v_\phi \equiv R\dot{\phi}$ is the azimuthal velocity (positive in the direction of Galactic rotation) and $v_z \equiv \dot{z}$.

### 2.2.1 Axisymmetric part of the potential

Below we give a detailed description of the individual components contributing to the axisymmetric part of the potential. Table 2.1 lists their characteristic parameters.

The bulge follows a Hernquist (1990) potential,

$$\Phi_{\rm b}(r) = -\frac{GM_{\rm b}}{a_{\rm b}+r}, \tag{2.1}$$

with $a_{\rm b} = 1$ kpc. We choose two different values for the mass of the bulge (and, therefore, of the bar): $M_{\rm b} = 10^{10} M_\odot$ (B1) and $M_{\rm b} = 2\times10^{10} M_\odot$ (B2, see Sect. 2.2.2).

We represent the thin and thick disk with Miyamoto & Nagai (1975) potentials,

$$\Phi_{{\rm d},i}(R,z) = -\frac{GM_i}{\sqrt{R^2+\left(a_i+\sqrt{z^2+b_i^2}\right)^2}}, \tag{2.2}$$

[1] Starting from a time $t = t_{\rm f}$, a point in space $\mathbf{x}$ and a grid of velocities $\mathbf{v}^j$, the orbits are integrated backward in time. At the end of each integration, each orbit reaches a point $(\mathbf{x}_0^j, \mathbf{v}_0^j)$, associated with the value of an analytic phase-space distribution function $f(\mathbf{x}_0^j, \mathbf{v}_0^j, t = t_0)$ corresponding to the unbarred potential. The collisionless Boltzmann equation states that the fine grained distribution function remains constant along the orbits. It is then possible to associate to each point of the grid of velocities a value of the phase-space density, since $f(\mathbf{x}, \mathbf{v}^j, t = t_{\rm f}) = f(\mathbf{x}_0^j, \mathbf{v}_0^j, t = t_0)$, and to see how the velocity space is populated at the point $\mathbf{x}$ of the Galaxy.

**Table 2.1:** Parameters of the two axisymmetric models A0+B1 and A0+B2.

| Parameter | |
|---|---|
| $M_{\rm b}(M_\odot)$ | $1\times10^{10}$ (B1) |
| | $2\times10^{10}$ (B2) |
| $a_{\rm b}$(kpc) | 1 |
| $M_{\rm h}(M_\odot)$ | $8\times10^{11}$ |
| $a_{\rm h}$(kpc) | 15.84 |
| $c$ | 18 |
| $M_{\rm thin}(M_\odot)$ | $5.76\times10^{10}$ |
| $M_{\rm thick}(M_\odot)$ | $1.14\times10^{10}$ |
| $a_{\rm thin}$(kpc) | 3.30 |
| $a_{\rm thick}$(kpc) | 3.05 |
| $b_{\rm thin}$(kpc) | 0.13 |
| $b_{\rm thick}$(kpc) | 0.98 |

where "$i$" stands for "thin" or "thick". The mass ratio between the two disks is 20% and this gives a thick-to-thin disk density normalization of $\sim 10\%$ near the Sun, similarly to what is observed in our Galaxy (Jurić et al. 2008). We have chosen the Miyamoto-Nagai functional form to represent the disks because of their mathematical simplicity which results in computational convenience. Since in reality the Galactic disks follow more closely an exponential form in the density (Binney & Tremaine 2008), we set the characteristic parameters of the Miyamoto-Nagai model to resemble the *gravitational potential* of two exponential disks with radial scale lengths $R_h = 3$ kpc (for both disks) and vertical scale lengths $z_{\rm thin} = 0.3$ kpc and $z_{\rm thick} = 1$ kpc. Although the potentials are similar, the forces differ. At $R = 8$ kpc the Miyamoto-Nagai thin disk overestimates the exponential disk vertical force $f_z$ up to 30% at $|z| \lesssim 0.3$ kpc, while it underestimates the force by $\sim 15\%$ at $|z| \gtrsim 0.3$ kpc. The exponential thick disk force in the Miyamoto-Nagai model is underestimated $\sim 10-15\%$ at all heights we consider. These differences in the force field can be regarded as being smaller than the uncertainties in the true form and values of the characteristic parameters of the Milky Way gravitational field (Fig. 9 of Rix & Bovy 2013 shows the discrepancy between different recent estimates of the Milky Way's vertical force at the Sun, e.g. $\sim 30\%$ at $z = 0.3$ kpc).

The dark halo follows the NFW potential (Navarro et al. 1997)

$$\Phi_{\rm h}(r) = -\frac{GM_{\rm h}}{\ln(1+c) - c/(1+c)} \frac{\ln(1+r/a_{\rm h})}{r}, \tag{2.3}$$

with $M_{\rm h} = 8\times10^{11} M_\odot$, $a_{\rm h} = 15.84$ and $c = 18$ (Battaglia et al. 2005).

The axisymmetric potential consisting of halo, thin and thick disks is referred as "A0" (and is the same for all models explored), while when the bulge is added we refer to A0+B1 or A0+B2 depending on the mass of the bulge.

**Table 2.2:** Parameters of the bar and location of the main resonances.

| Parameter | GB | LB |
|---|---|---|
| $M_{\rm bar}(M_\odot)$ | $1\times10^{10}$ (GB1) | $1\times10^{10}$ (LB1) |
| | $2\times10^{10}$ (GB2) | $2\times10^{10}$ (LB2) |
| $a$(kpc) | 3.5 | 3.9 |
| $b$(kpc) | 1.4 | 0.6 |
| $c$(kpc) | 1.0 | 0.1 |
| $R_{\rm CR}$(kpc) | 4.54 (A0+GB1) | 4.57 (A0+LB1) |
| | 4.91 (A0+GB2) | 4.94 (A0+LB2) |
| $R_{\rm OLR}$(kpc) | 7.40 (A0+GB1) | 7.40 (A0+LB1) |
| | 7.69 (A0+GB2) | 7.69 (A0+LB2) |
| $R_{-1:1}$(kpc) | 9.91 (A0+GB1) | 9.91 (A0+LB1) |
| | 10.22 (A0+GB2) | 10.22 (A0+LB2) |

### 2.2.2 Bar potential

The 3D bar used in our simulations is a Ferrers (1870) bar, whose density profile is given by

$$\rho_{\rm bar}(m^2) = \begin{cases} \rho_0(1-m^2/a^2)^n & m \le a \\ 0 & m > a, \end{cases} \tag{2.4}$$

where $m^2 \equiv a^2\left(x^2/a^2 + y^2/b^2 + z^2/c^2\right)$. We choose $n = 2$ and explore two sets of axis lengths taken from Bissantz & Gerhard (2002) and López-Corredoira et al. (2007), respectively. We dub them "Galactic Bar" (GB) and "Long Bar" (LB), in the same fashion as Gardner & Flynn (2010). The bar parameters are listed in Table 2.2.

For the pattern speed of the bar we use the value $\Omega_{\rm b} = 50$ km s$^{-1}$ kpc$^{-1}$, i.e. in the range of current determinations, which is between 35 and 60 km s$^{-1}$ kpc$^{-1}$ (Gerhard 2011). It is important to notice that the effects on the velocity distribution in a certain volume are mainly set by the proximity to the main resonances. This implies that a faster (slower) pattern speed yields similar effects as the original bar in outer (inner) volumes.

As anticipated, the bar potential grows smoothly in time in the simulations. Specifically, each simulation starts with an axisymmetric potential (either A0+B1 or A0+B2), and the mass of the bulge is transferred to the bar using the function

$$\eta(t) = \left(\frac{3}{16}\xi^5 - \frac{5}{8}\xi^3 + \frac{15}{16}\xi + \frac{1}{2}\right), \quad \xi = 2\frac{t}{t_1} - 1, \tag{2.5}$$

which runs smoothly from $\eta(0) = 0$ to $\eta(t_1) = 1$ (Dehnen 2000). In particular:

- for $t \in [0, t_1]$, $M_{\rm bar}(t) = \eta(t)M_{\rm b}(0)$ and $M_{\rm b}(t) = [1-\eta(t)]M_{\rm b}(0)$,
- for $t > t_1$, $M_{\rm bar}(t) = M_{\rm b}(0)$ and $M_{\rm b}(t) = 0$.

In our models $M_{\rm b}(0) = M_{\rm bar}(t \ge t_1) = 10^{10}M_\odot$ (B1) and $M_{\rm b}(0) = M_{\rm bar}(t \ge t_1) = 2\times10^{10}M_\odot$ (B2), which is consistent with the mass estimates by Dwek et al. (1995) and Zhao & Mao (1996), respectively.

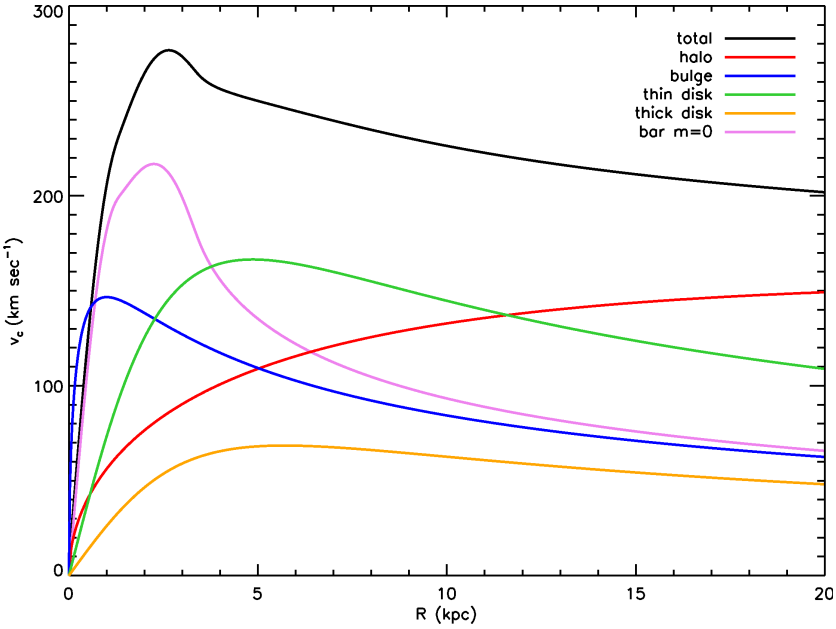


**Figure 2.1:** Circular velocity curves of the components of A0 (halo, thin and thick disk), bulge B2 and the $m = 0$ Fourier component of the bar GB2. The solid black line is the resulting circular velocity for model A0+GB2.

In all our simulations the bar grows following Eq. (2.5), up to time $t_1$. The choice of $t_1$ is not particularly relevant, as it was shown in Minchev et al. (2010) that a longer growth time of the bar only linearly delays the effects of the bar (in this case, the formation of the kinematic structures). Throughout this paper we always use $t_1 = 2T_{\rm bar} \simeq 246$ Myr as in Fux (2001), where $T_{\rm bar} = 2\pi/\Omega_{\rm b}$.

In Fig. 2.1 we show the circular velocity curves of the components of A0 and of the bulge B2. In the same figure we plot the circular velocity of the $m = 0$ term of the Fourier decomposition of the bar potential GB2 (GB with $M_{\rm bar} = 2 \times 10^{10} M_{\odot}$). Note that, although the total mass of the bulge and the bar are the same, inside $R = 20$ kpc their velocity curves (blue and purple lines, respectively) differ because the enclosed masses are different. While the Hernquist bulge extends to infinity, all the bar's mass is confined inside a radius equal to its semi-major axis (see Eq. 2.4). As a consequence, when the bar growth has been completed, the resulting circular velocity curve has changed. For this reason, for our analysis we use the circular velocity curve $v_{\rm c}(R)$ obtained by adding the contributions of the dark halo, thin and thick disk and $m = 0$ component of the bar potential (A0+GB2). This curve is represented by the black line in Fig. 2.1. We see how the total rotation curve is mostly influenced by the bar for approximately $R < 5$ kpc, by the thin disk for 5 kpc $< R <$ 10 kpc and by the dark halo for $R >$ 10 kpc. The value of the circular velocity at Solar radius, and for $z = 0$ is $v_{\rm c}(8\ {\rm kpc}) \simeq 222$ km s$^{-1}$ for A0+GB1 and $v_{\rm c}(8\ {\rm kpc}) \simeq 234$ km s$^{-1}$ for A0+GB2.

### 2.2.3 Initial conditions

We use two sets of initial conditions for our simulations: ICTHIN and ICTHICK. ICTHIN mimics the typical kinematics and density distribution of the intermediate age population of the thin disk, while ICTHICK represents the thick disk. We generate low (LR) and high resolution (HR) realizations, that have $N = 5 \times 10^7$ and $N = 10^9$ particles respectively. We perform HR simulations for our standard Galactic model (A0+GB2, see below), to help to distinguish the resonant features that are in the wings of the distribution and often hidden in the noise.

The positions $(R, \phi, z)$ of the particles in both disks are distributed following Miyamoto-Nagai densities, corresponding to the potentials described in Sect. 2.2.1. The density distribution of each disk, $\rho_{\mathrm{d},i}$, is derived from Eq. (2.2) through Poisson's equation (for the complete expression see Miyamoto & Nagai 1975). The $(R, z)$ positions of the particles are randomly drawn from these profiles with a method based on the Von Neumann's rejection technique (Press et al. 1992) and $\varphi$ is generated uniformly between 0 and $2\pi$.

Once the positions are generated, the velocities are assigned in the following way. We describe the radial velocity dispersion $\sigma_{R,i}$, as

$$\sigma^2_{R,i}(R) = \sigma^2_{0,i} \exp\left(-\sqrt{R^2 + 2a_{\mathrm{s}}^2}/R_{\mathrm{h}}\right), \tag{2.6}$$

(Hernquist 1993), which implies that, far enough from the center, $\sigma^2_{R,i} \propto \exp(-R/R_{\mathrm{h}})$. In the center the smoothing parameter $a_{\mathrm{s}}$ reduces the velocity dispersion. Hernquist (1993) uses $a_{\mathrm{s}} = R_{\mathrm{h}}/4$. We prefer $a_{\mathrm{s}} = R_{\mathrm{h}}$, which makes the smoothing much more gradual. We relate the tangential velocity dispersion $\sigma_{\phi,i}$ to the radial $\sigma_{R,i}$ through the epicyclic approximation, i.e.,

$$\sigma^2_{\phi,i}(R) = \sigma^2_{R,i}(R) \frac{\kappa^2(R)}{4\Omega^2(R)}, \tag{2.7}$$

where $\Omega(R)$ and $\kappa(R)$ are the circular and epicyclic frequencies. This relation is not very accurate even for moderate velocity dispersions (Kuijken & Tremaine 1991), but because of its simplicity it is a good starting point, as the initial conditions are later relaxed (see below).

Finally, the vertical velocity dispersion $\sigma_{z,i}$ is obtained by solving the following Jeans equation for an axisymmetric system

$$\frac{1}{R}\frac{\partial\left[R\rho_{\mathrm{d},i}(\overline{v_R v_z})_i\right]}{\partial R} + \frac{\partial\left(\rho_{\mathrm{d},i}\sigma^2_{z,i}\right)}{\partial z} = \rho_{\mathrm{d},i}\frac{\partial\Phi}{\partial z}, \tag{2.8}$$

where $\Phi(R, z)$ is the total potential of the Galaxy. Again for the sake of simplicity, we assume a velocity ellipsoid aligned with the $R$ and $z$ axes, i.e., $(\overline{v_R v_z})_i = 0$, the first term in the left-hand side of Eq. (2.8) vanishes, and

$$\sigma_{z,i}(R, z) = \frac{1}{\rho_{\mathrm{d},i}(R, z)} \int_z^\infty \mathrm{d}z' \rho_{\mathrm{d},i}(R, z') \frac{\partial\Phi}{\partial z'}. \tag{2.9}$$

In practice, we compute Eq. (2.9) on a discrete grid of equispaced points on the meridional plane and, to obtain $\sigma_{z,i}(R, z)$ in a generic $(R, z)$ point, we linearly interpolate between the nearest grid points.

Each velocity component of a particle is assigned by drawing a random number from a Gaussian distribution with the respective dispersion. The tangential component of the velocity, $v_{\phi,i}$, is corrected for the asymmetric drift $v_{\mathrm{a},i}$,

$$v_{\mathrm{a},i}(R) = \frac{\sigma_{R,i}^2}{2v_\mathrm{c}} \left[ \frac{\sigma_{\phi,i}^2}{\sigma_{R,i}^2} - 1 - \left. \frac{\partial \ln(\rho_{\mathrm{d},i}\sigma_{R,i}^2)}{\partial \ln R} \right|_{z=0} \right], \tag{2.10}$$

(Binney & Tremaine 2008) where, again, we set $(\overline{v_R v_z})_i = 0$.

The initial conditions generated in this way are not fully consistent with the potential. In particular we have assumed the velocity distribution to be locally Gaussian. Therefore we expect these to change in time, while reaching equilibrium with the potential. These transient effects are described in Minchev et al. (2009) and produce kinematic arcs in the Solar Neighborhood. To avoid confusion between these effects and those induced by the bar we first let our initial conditions evolve in the axisymmetric potential for a time $t_\mathrm{r}$. We find that $t_\mathrm{r} \sim 8$ Gyr suffices to reach a stationary state in the inner $\sim 10$ kpc of the Galaxy. We use these evolved initial conditions as effective initial conditions for our simulations with the bar.

The evolution of the velocity dispersions for ICTHIN and ICTHICK is shown in Fig. 2.2 for the axisymmetric potential A0+B2 (the results for A0+B1 are similar). We see that the radial and tangential velocity dispersions increase in the outer parts of the Galaxy and decrease in the inner regions, both for ICTHIN and ICTHICK. In contrast, the vertical velocity dispersion does not evolve for ICTHIN and only slightly increases for ICTHICK. This is likely because the vertical velocity dispersion is obtained directly by solving the Jeans equation, while the radial dispersion and tangential profiles are only imposed later using Eq. (2.6) and related through the epicyclic approximation .

An intermediate age population in the thin disk ($\sim 5$ Gyr) has local velocity dispersions $(\sigma_R, \sigma_\phi, \sigma_z) \sim (40, 26, 17)$ km s$^{-1}$ (Robin et al. 2003; Holmberg et al. 2007). After evolution, our set of initial conditions ICTHIN has comparable characteristics with slightly larger $\sigma_\phi$ and smaller $\sigma_z$ (Fig. 2.2, top). The measured local dispersions of the stars in the thick disc are $(\sigma_R, \sigma_\phi, \sigma_z) \sim (67, 51, 42)$ km s$^{-1}$ according to Robin et al. (2003) or smaller in the $\phi$ and $z$ directions $(\sigma_R, \sigma_\phi, \sigma_z) \sim (67, 38, 35)$ km s$^{-1}$ as reported in Bensby et al. (2003). Our initial conditions ICTHICK after the evolution in the imposed potential are consistent with these measurements (Fig. 2.2, bottom).

### 2.2.4 Orbits and resonances

Let us, for a moment, consider orbits in an axisymmetric potential. The guiding center of a star with angular momentum $L_z$ is defined as that radius $R_\mathrm{g}$ where

$$R_\mathrm{g}^2 \Omega\left(R_\mathrm{g}\right) = L_z. \tag{2.11}$$

Therefore the azimuthal velocity of a star, located at $R$ in the Galaxy, is

$$v_\phi = \frac{R_\mathrm{g}^2 \Omega\left(R_\mathrm{g}\right)}{R} \tag{2.12}$$

where $R_\mathrm{g}$ is the radius of the guiding center of its orbit. Of particular interest are the orbits with $R_\mathrm{g}$ such that

$$l_2 \kappa(R_\mathrm{g}) = l_1 \left[\Omega(R_\mathrm{g}) - \Omega_\mathrm{b}\right], \tag{2.13}$$

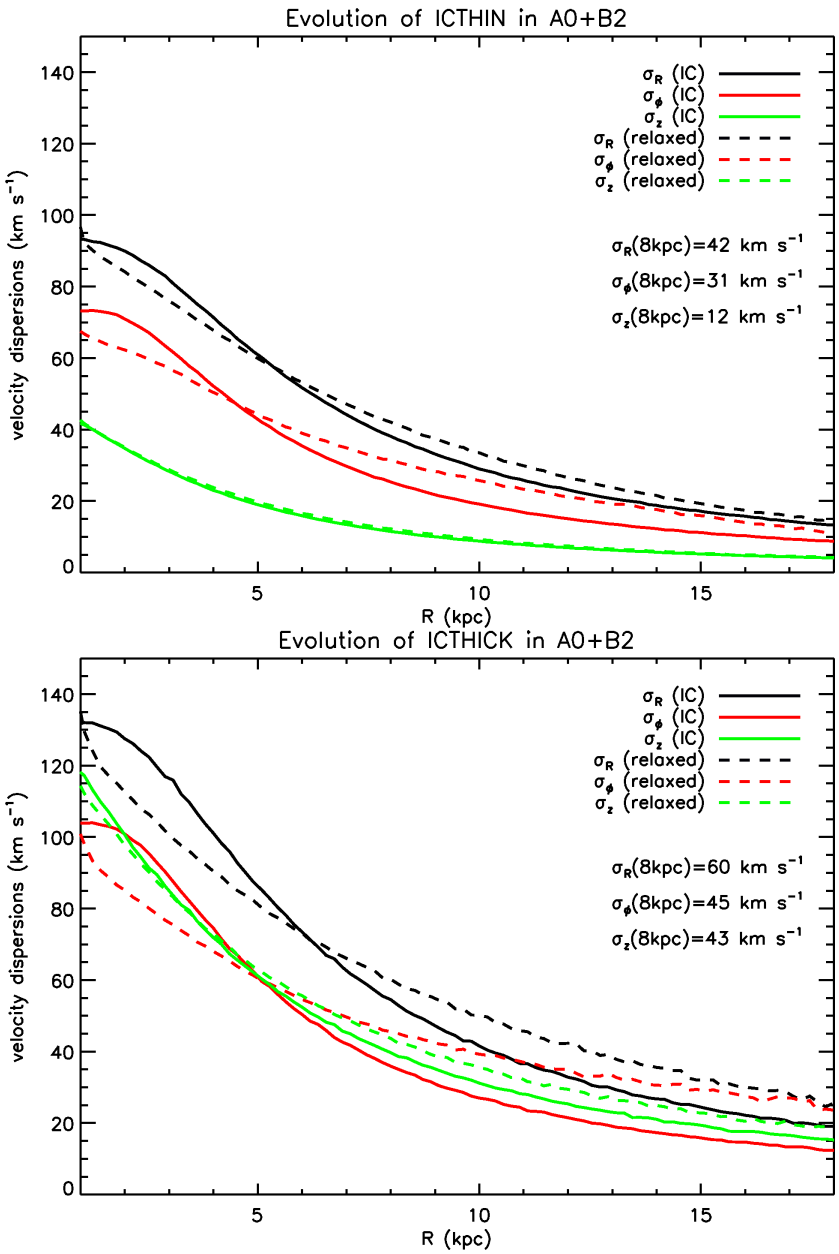


**Figure 2.2:** Velocity dispersions before and after the evolution of the initial conditions in the A0+B2 axisymmetric potential for $t_r \simeq 8.3$ Gyr and for stars with final $|z| < 0.3$ kpc. The final velocity dispersions at $R = 8$ kpc are also indicated.

where $l_1$ and $l_2$ are two integer numbers. For these orbits the epicyclic frequency resonates with the frequency of the circular orbit at $R_{\rm g}$, in the reference frame rotating with pattern speed $\Omega_{\rm b}$. In other words, orbits well described by the epicyclic approximation (i.e., not too eccentric) that satisfy this condition are closed in this reference frame[2]. Important for the rest of the paper are, especially, the Outer Lindblad Resonance (OLR, $R_{\rm g} = R_{\rm OLR}$) where $l_1 = -2$ and $l_2 = 1$, the $-1:1$ Resonance ($R_{\rm g} = R_{-1:1}$), where $l_1 = -1$ and $l_2 = 1$, and the Corotation Resonance ($R_{\rm g} = R_{\rm cor}$), where $l_2 = 0$ i.e., $\Omega(R_{\rm g}) = \Omega_{\rm b}$. In Fig. 2.3 we show the positions of the main resonances for the A0 +GB2 potential but considering only the $m = 0$ Fourier component of GB2, for $\Omega_{\rm b} = 50$ km s$^{-1}$ kpc$^{-1}$ (Table 2.2).

Now, let us assume a small non-axisymmetric perturbation (the bar) to the axisymmetric potential, rotating with pattern speed $\Omega_{\rm b}$. If the perturbation is small, the motion of most stars will still be approximately described by the epicyclic theory. However, some stars will be more strongly affected by the perturbation, namely those that satisfy Eq. (2.13) in the axisymmetric potential. As stated by Binney & Tremaine (2008), at the resonances the "perturbation is acting with one sign for a long time. If the effects of a perturbation can accumulate for long enough, they can become important, even if the perturbation is weak".

### 2.2.5 Vertical motion

The simple dynamical picture that we described in the previous section is complicated in two ways in the Milky Way: the Galactic disks are 3D structures, i.e. stars have vertical motions, and especially the thick disk population is kinematically hot.

The epicyclic approximation assumes that the orbits of the stars are not too eccentric and that the amplitudes of the vertical motions are so small that horizontal and vertical motions are nearly decoupled. In an axisymmetric potential the motion is exactly decoupled when the radial and vertical force ($f_R$ and $f_z$) are respectively functions of $R$ and $z$ only. This is only true very near to the Galactic plane. In Fig. 2.4 we have plotted the radial (top) and vertical (bottom) forces for the total potential (color) and the contribution of the bar ($m > 0$ terms of the Fourier decomposition, black solid lines) for the model A0+GB2. The bottom panel shows, as just discussed, that $f_z$ is independent of $R$ only at small $z$ (where it runs parallel to the cylindrical radius axis). However, already beyond $z \sim 0.3$ kpc, it varies significantly with $R$, over the range explored by many orbits that visit the Solar Neighborhood. On the other hand, the top panel shows that the $f_R$ isocontours are less curved and that this force decreases more slowly with $z$ (and the force decreases even more slowly if we consider the bar's radial force only as indicated by the black curves). For this reason the radial motion may be expected to be more similar with height, than the vertical motion with radius. Furthermore, it is important also to note that orbits with angular momentum $L_z$ and vertical oscillations larger than $\sim 0.3$ kpc live in a range of $R$ that is hundred of parsecs different from that of a planar orbit with the same $L_z$ angular momentum (see Binney & McMillan 2011).

We want to emphasize that for all our models the bar induces horizontal forces that, at $R \sim 8$ kpc, are almost independent on $z$ (top panel of Fig. 2.4, solid black curves). In fact, the relative importance of the perturbation due to the bar with respect to the axisymmetric potential slightly increases with $z$, as a consequence of the decreasing radial

[2] A better approximation for the azimuthal frequency than the circular frequency was given by Dehnen (1999). At a certain radius $R$ this frequency depends both on $v_\phi$ and, less significantly, on $v_R$.

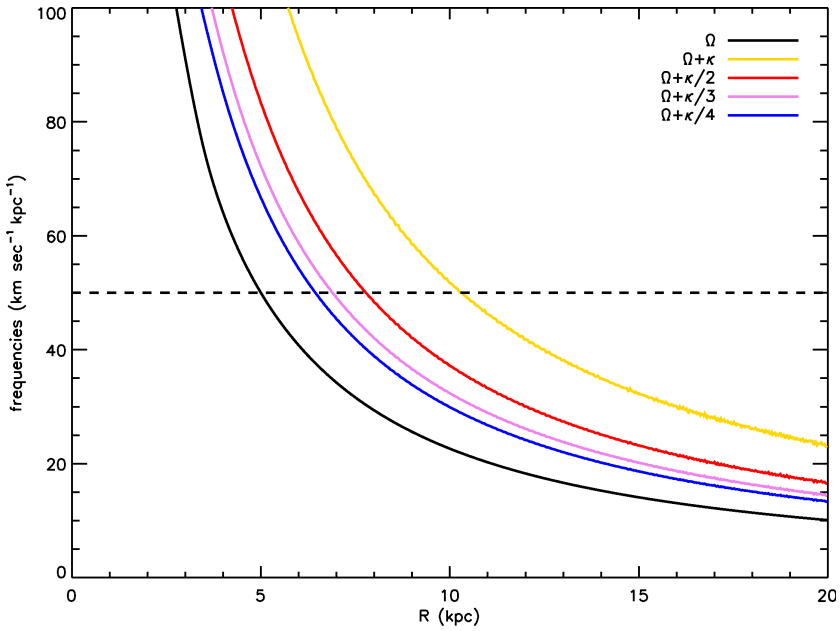


**Figure 2.3:** Positions of the main resonances for the model A0+GB2 ($m = 0$ Fourier component) with $\Omega_b = 50$ km s$^{-1}$ kpc$^{-1}$ (horizontal dashed line). The position is given by the $R$ at which the curves cross the horizontal line.

force of the axisymmetric part of the potential. Therefore, we expect stars far from the Galactic plane to experience a slightly stronger relative effect of the bar compared to those on the plane.

To study how the vertical motions affect the simple dynamical picture previously sketched, particularly for the populations with larger kinematic temperature, requires however suitable and fully 3D orbital integrations (as Fig. 2.4, bottom panel shows).

## 2.3 Results

Motivated by the above discussion, we turn to numerical simulations to study how the bar impacts the kinematics of stars near the Sun and neighboring volumes.

We conventionally place the Sun on the Galactic plane, at $(R, \phi) = (R_0, \phi_0) \equiv (8 \text{ kpc}, -20°)$ and we consider cylindrical volumes throughout the Galaxy of radius $R_{\rm vol} = 0.3$ kpc and height $h_{\rm vol} = 0.6$ kpc, centered at some $(R, \phi, z)$. For each volume we study the $v_R$ vs. $v_\phi$ velocity distribution.

### 2.3.1 General effects of the bar and time evolution

In Fig. 2.5 we show the evolution in time of the kinematics in the Solar Neighborhood volume for the model A0+GB2 and the LR thin disk initial conditions (LR ICTHIN).

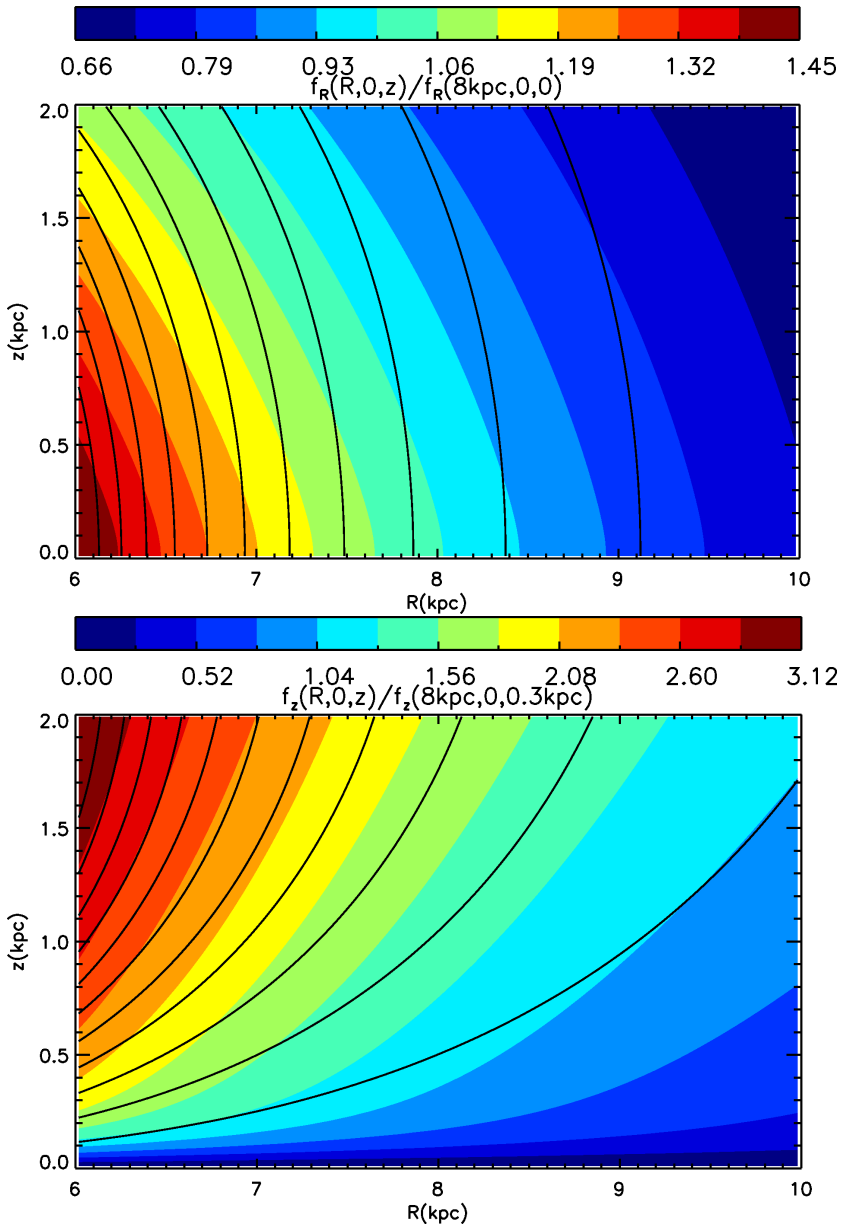


**Figure 2.4:** Isocontours of the $f_R$ (top panel) and $f_z$ (bottom panel) forces for the the potential A0+GB2 (colors) and $m > 0$ terms of the Fourier decomposition of GB2 (black solid lines). The meridional plane is shown at $\phi = 0$ (along the long axis of the bar).

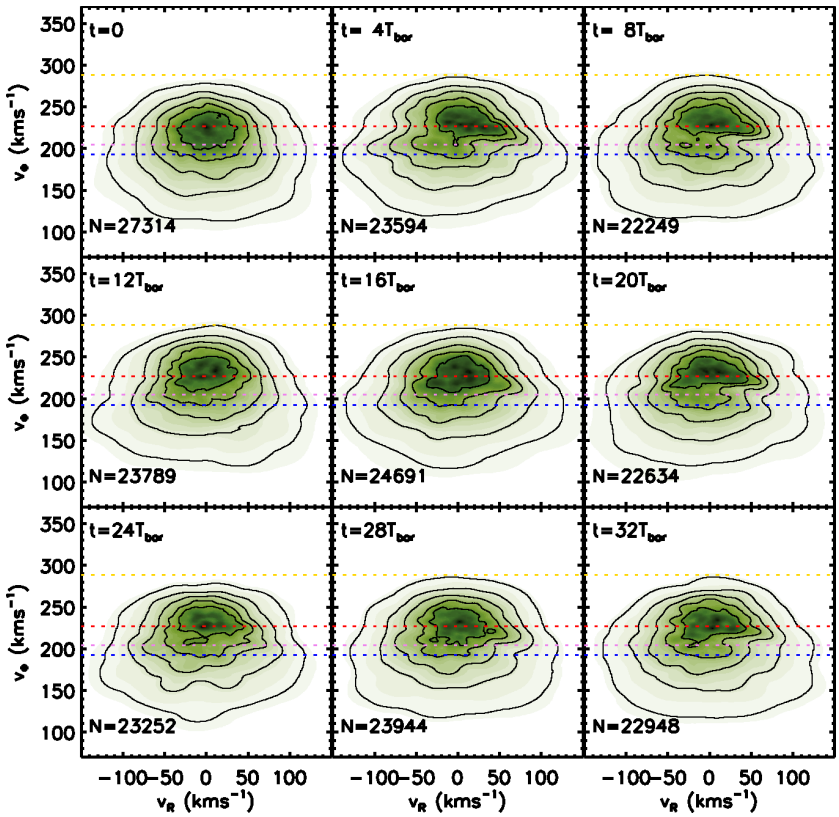


**Figure 2.5:** Evolution in time of the kinematics of the simulated LR thin disk in the Solar Neighborhood volume for the potential A0+GB2. The dashed horizontal lines correspond to $v_{\phi,-1:1}$ (yellow), $v_{\phi,\mathrm{OLR}}$ (red), $v_{\phi,-3:1}$ (purple) and $v_{\phi,-4:1}$ (blue). The density field is obtained with the modified Breiman estimator, described in Ferdosi et al. (2011), with optimal pilot window $\sigma^{\mathrm{opt}} = 9.6$ km s$^{-1}$. The contours enclose $0.25p_{1\sigma} \times i$ %, $i = 1, ..., 5$ of the probability, where $p_{1\sigma} = 68.268$. In the lower left part of the panel we indicate the number of particles in the volume.

Specifically, to describe the kinematics we use a probability density function of $(v_R, v_\phi)$, determined with the modified Breiman estimator, described in Ferdosi et al. (2011), with optimal pilot window $\sigma^{\rm opt} = 9.6$ km s$^{-1}$. We show 5 density contours that enclose (from inside to outside) $0.25 p_{1\sigma} \times i$ %, $i = 1, ..., 5$ of the probability, where $p_{1\sigma} = 68.268$. The 4-th contour from inside out corresponds, therefore, to the $1\sigma$ contour. The evolution seen in Fig. 2.5 is qualitatively similar for all the other potentials (and respective values of the parameters) explored. As we can see, the form of the distribution changes with time (see Minchev et al. 2010 for a colder disk). Initially, the distribution of stars is featureless, symmetric in $v_R$, and with a tail of stars at low $v_\phi$ due to the asymmetric drift. At $t = 4T_{\rm bar}$ the distribution has changed completely: it is split up in two regions and presents other deformations that make it asymmetric, both in $v_R$ and $v_\phi$.

Before proceeding with the analysis of the evolution in this plane, it will be useful for the rest of the paper to introduce a terminology describing the features seen in velocity space. In Fig. 2.5 we have indicated the $v_\phi$ of four important families of resonant orbits, using Eq. (2.12) for $R = 8$ kpc: $v_{\phi,-1:1}$ (yellow dashed line), $v_{\phi,\rm OLR}$ (red dashed line), $v_{\phi,-3:1}$ (purple dashed line) and $v_{\phi,-4:1}$ (blue dashed line). As we can see, the diagonal valley in the velocity distribution corresponds roughly to $v_{\phi,\rm OLR}$, confirming the large effect of the Outer Lindblad Resonance on the kinematics of the stars. Following Dehnen (2000), we call the peak in the density of stars above the valley the "LSR Mode", and the one below the "OLR Mode". Furthermore, in the right part of the LSR Mode, at $(v_R, v_\phi) \sim (75$ km s$^{-1}, 220$ km s$^{-1})$, there is an elongation in $v_R$, which we call "Horn".

Previous studies have used default integration times of $t_2 = 4T_{\rm bar}$ (Dehnen 2000). We notice here that between $t = 4T_{\rm bar}$ and $t = 16T_{\rm bar}$ there is still significant evolution of the distribution, which only reaches a stationary configuration later. For instance, the valley between the LSR Mode and the OLR is progressively filled with stars. The OLR and LSR Modes change shape in time.

In general, it is clear from Fig. 2.5 that all the features associated to the bar are most prominent for short integration times. The features that we find in the velocity distribution for these times are similar to those observed by Dehnen (2000) in 2D integrations with a quadrupole bar. This is the first time that they are seen in 3D simulations. On the other hand, the time evolution confirms, again in 3D, the results obtained by Fux (2001) in his study of the time evolution and phase-mixing of orbits in 2D and with the quadrupole bar.

As our thin disk corresponds to an intermediate-old population of stars, ($\sim 10$ Gyr; see Robin et al. 2003), it is unlikely that they experienced the effects of the bar only for $4T_{\rm bar}$ ($\approx 492$ Myr). On the other hand, Cole & Weinberg (2002), using properties of infrared carbon stars from the Two Micron All Sky survey, state that the Milky Way Bar is likely to be younger than 3 Gyr, fixing an upper limit for its formation to 6 Gyr ago (however studies of the bulge indicate that it is dominated by a stellar population older than 10 Gyr, e.g., Minniti & Zoccali 2008). Given this, we decide to choose a default integration time of $t_2 = 24T_{\rm bar} \sim 3$ Gyr, when the kinematics has roughly reached stationarity. Note that we are effectively assuming that the properties of the bar, such as its pattern speed, did not change much during this time[3].

[3] Weinberg (1994) studied the kinematic response of the Galactic disk (mean velocity and dispersion) in the presence of a bar with variable pattern speed.

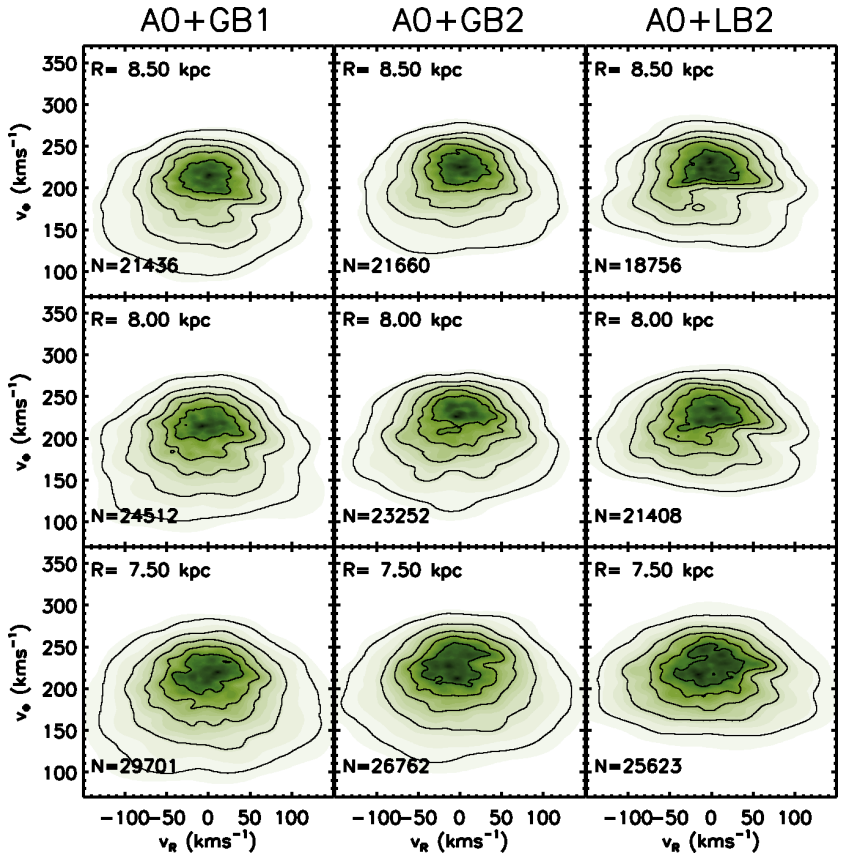


**Figure 2.6:** Effect of different bar potentials on the kinematics of the simulated thin disk in 3 volumes centered at an angle $\phi = -20°$ and $R = 8.5,\ 8,\ 7.5$ kpc for $t = 24T_{\rm bar}$.

### 2.3.2 Thin disk

Fig. 2.6 shows the kinematics of the thin disk in the Solar Neighborhood and in two nearby volumes aligned with the Solar Neighborhood ($\phi = -20°$) but at different radii ($R = 8.5$ kpc and $R = 7.5$ kpc) for various potentials and LR simulations. The first and second column show the distributions with the bar potential with $M_{\rm bar} = 10^{10} M_\odot$ and $M_{\rm bar} = 2 \times 10^{10} M_\odot$, respectively. Not surprisingly, the effect of the least massive bar is weaker compared to a bar twice as massive. The density contrast between the OLR Mode and the LSR Mode is smaller, and the Horn is slightly less prominent for the least massive bar. The overall distribution has also a more symmetric appearance (quantifiable using $\langle v_R \rangle$). These small differences are explainable by simply noting that the force of the perturbation is only slightly smaller in the case of the least massive bar. The non-axisymmetric part of the force (i.e. excluding the monopole term associated to the bar) differs only by $\sim 30\%$ at $R = 8$ kpc between the GB1 and GB2. Some of

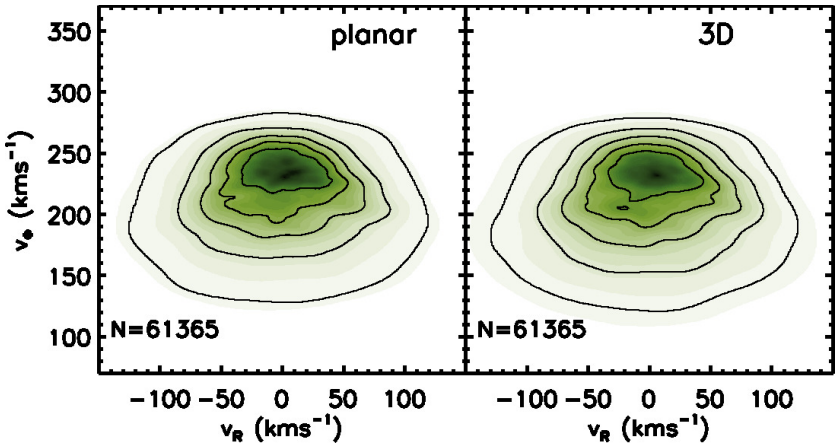


**Figure 2.7:** Kinematics in the Solar Neighborhood at $t = 24T_{\rm bar}$ for two subsets of the thin disk HR simulation with A0+GB2 potential. Left panel: the most planar particles in the simulation. Right panel: a random subsample of the simulation with the same number of stars.

the differences between the distributions may also be ascribed to the difference between the circular velocity curves of A0+B1 and A0+B2, which have the resonances at slightly different positions (see Table 2.2). Since the resonances are mostly responsible for the effects of the bar on the kinematics of the stars, we expect some differences at fixed[4] $R$.

The second and third columns of Fig. 2.6 allow us to compare more massive bar models ($M_{\rm bar} = 2 \times 10^{10} M_\odot$) with different geometrical properties (GB and LB). The Long Bar (third column) has slightly different effects on the thin disk velocity distributions than the less elongated Galactic Bar. It produces sharper features such as a Horn with a more defined lower edge, especially for $R = 8.5$ kpc and $R = 8$ kpc. This was already noticed by Gardner & Flynn (2010) when they compared the responses to these two Ferrers bar models, but we confirm here their results in our 3D simulations. Nevertheless, we stress that, for this long integration time, the differences between the effect of the different bars on the kinematics inside the various volumes explored is much less significant than for shorter integration times. Furthermore, for short integration times the structures are much more evident in all our bar models.

Given the uncertainties in having a satisfactory model for the bar (recent studies even suggest that it could be a superposition of something similar to our Galactic Bar and Long Bar, see Robin et al. 2012), we use from now on as a default model the Galactic Bar and the potential A0+GB2, confident that the effects will be similar for all the other models, especially for long integration times, as illustrated in Fig. 2.6.

Since most works so far have used 2D simulations, it is important to understand if significant differences exist for the kinematics near the plane in the 2D vs. 3D simulations.

[4] These differences may also reflect a dissimilar evolution of the distributions. As explained in Minchev et al. (2010), the typical time of libration of the stars trapped to the resonances depends on the bar strength; since the shape of the distributions is defined mostly by the resonances, we may expect, at the same snapshot, different evolutionary stages for different bar strengths.

To this end we consider a subset of the HR 3D thin disk simulation in the potential A0+GB2, constituted by those particles that, at $t = 0$, have $|z| < 0.05$ kpc and $|v_z| < 5$ km s$^{-1}$. These are the particles whose vertical oscillations have the smallest amplitude in the simulation: at $t = 24T_{\rm bar}$ their $z$ dispersion is still less than 0.04 kpc and their $v_z$ dispersion less than 4 km s$^{-1}$. It is then reasonable to expect they behave in a similar fashion to particles in a 2D simulation, distributed on the Galactic plane with similar $(R, \phi)$ density and kinematics at $t = 0$, and subject to the same potential A0+GB2.

Fig. 2.7 shows the kinematics of the subset of most "planar" particles (left panel) and the kinematics of a random subsample of the whole 3D simulation with the same number of stars (right panel), in the Solar Neighborhood volume at the default integration time. We note that there are no large differences between the velocity distributions for these two data sets. The two sets do have slightly differing velocity dispersions: the planar particles are slightly colder ($\sigma_R = 42$ km s$^{-1}$ kpc$^{-1}$, while $\sigma_R = 44$ km s$^{-1}$ kpc$^{-1}$ for the 3D subsample), but this is a reflection of the initial conditions. This agreement stems likely from the fact that the planar and vertical motions are decoupled for most thin disk particles. Since our 3D thin disk is particularly cold in $v_z$ ($\sigma_z \sim 12$ km s$^{-1}$ at $R = 8$ kpc), it is also possible that the motion is more decoupled in our simulations than in reality since the observed local dispersion is $\sigma_z \sim 17$ km s$^{-1}$ (Robin et al. 2003; Holmberg et al. 2007).

In Fig. 2.8 we show the kinematics of the thin disk in the vicinity of the Solar Neighborhood at $t = 24T_{\rm bar}$ and in HR. From left to right, the columns correspond to volumes centered at angles $\phi = -40°$, $\phi = -20°$ and $\phi = 0$ (aligned with the bar). From bottom to top, the rows correspond to different Galactocentric radii from $R = 7$ kpc to $R = 9$ kpc in steps of $\Delta R = 0.5$ kpc. The yellow, red, purple and blue dashed lines represent $v_\phi$ of the main resonances (as in Fig. 2.5), obtained using Eq. (2.12) with $R$ of the corresponding volume. This figure shows that the main kinematic features associated to the bar vary as a function of position in the Galaxy, similarly to the effects already reported in the literature for 2D simulations. First, we note that the main features shift in $v_\phi$ as $R$ varies. At $R = 9$ kpc (first row), $v_{\phi,\rm OLR}$ is in the low $v_\phi$ tail of the distribution ($v_\phi \sim 180$ km s$^{-1}$), the OLR Mode has a small extension, and the Horn is placed at the lower right edge of the $1\sigma$ contour (4-th contour). For $R \sim 7.5$ and 8 kpc $v_{\phi,\rm OLR}$, and in consequence the separation between LSR Mode and OLR Mode, lies at the center of the $v_\phi$ distribution ($v_\phi \sim 220$ km s$^{-1}$), and the LSR Mode and OLR Mode become clearly separated. For $R = 7$ kpc (bottom row), superposed, the LSR mode can hardly be seen the Horn is now at the upper right edge of the distribution. Since these features are mostly associated with the resonant orbits, their shift can be explained in light of Eq. (2.12), for each of the resonant families ($R_{\rm g}$ constant).

We can also observe a change in the mean $v_R$ of the OLR Mode as the orientation of the volume with respect to the bar ($\phi$) is varied. While the OLR Mode is almost completely symmetric with respect to the $v_R$ axis for $\phi = 0$, it moves towards $v_R < 0$ for more negative $\phi$. At $\phi = -40°$ the OLR Mode is completely in the $v_R < 0$ half plane at almost all radii. We quantify this change in Fig. 2.9. The red solid line shows the mean $v_R$ for particles with $v_\phi < v_{\phi,\rm OLR}$, in volumes at $R = 8$ kpc as a function of $\phi$ (plotted in steps $\Delta\phi = 2.5°$). The black solid line represents the same quantity, but for the axisymmetric initial conditions and averaged between all the angles. The dashed lines represents twice the standard deviation of the set of means obtained for all the angles. This figure shows that the OLR Mode varies periodically in $v_R$ as a function of $\phi$, and that the amplitude of

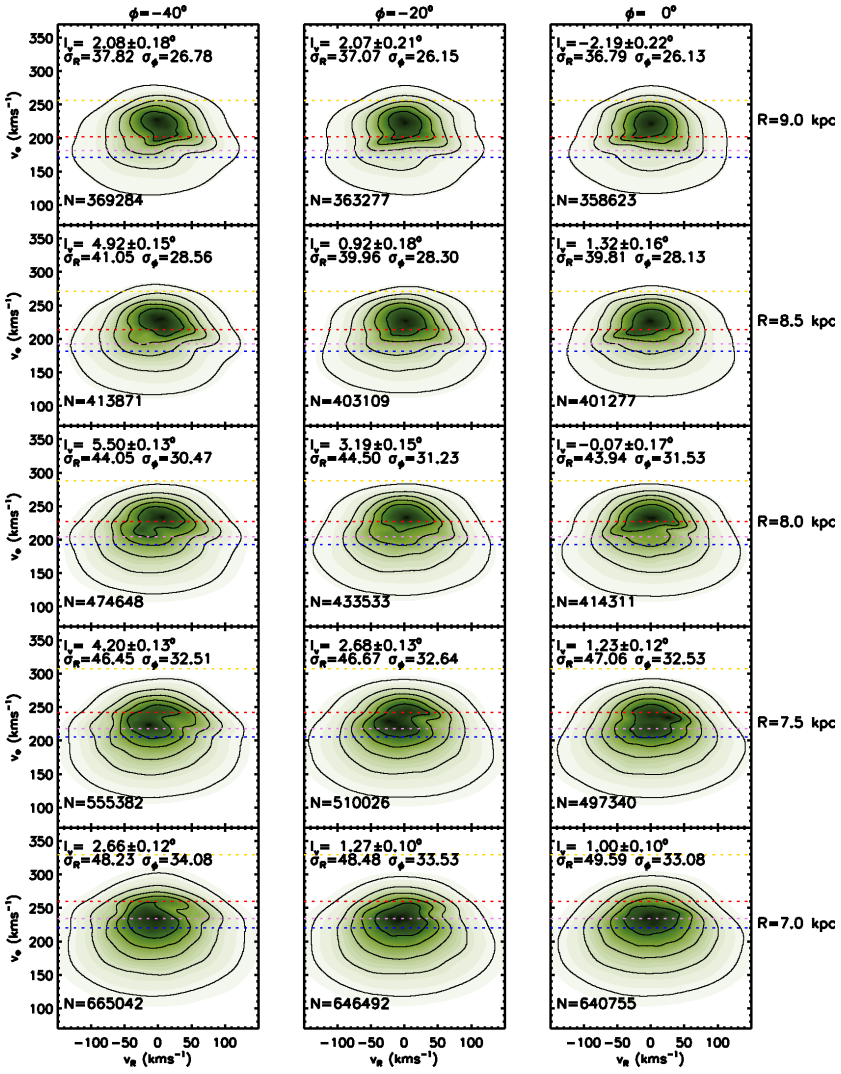


**Figure 2.8:** Kinematics of the simulated HR thin disk in the potential A0+GB2 in different volumes at $t = 24T_{\rm bar}$. Different columns correspond to volumes centered at different angles from the bar in the direction of antirotation, from $\phi = -40°$ (leftmost column) and with step $\Delta\phi = 20°$. Different rows correspond to volumes centered at different Galactocentric radii, from $R = 9$ kpc (topmost row) and with step $\Delta R = 0.5$ kpc. The dashed lines correspond to $v_{\phi,-1:1}$ (yellow), $v_{\phi,\rm OLR}$ (red), $v_{\phi,-3:1}$ (purple) and $v_{\phi,-4:1}$ (blue). Notice how for the volumes in the bottom row $v_{\phi,\rm OLR}$ and $v_{\phi,-1:1}$ are superposed.

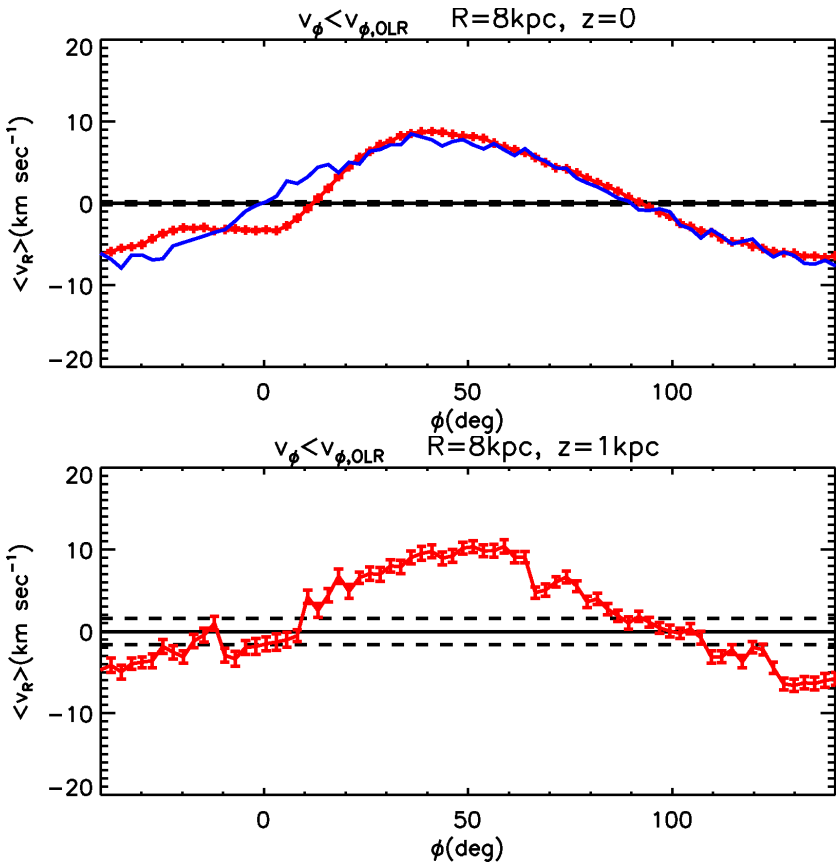


**Figure 2.9:** Average $v_R$ of thin disk particles $v_\phi < v_{\phi,\mathrm{OLR}}$ in volumes centered at $R = 8$ kpc as a function of $\phi$ for the HR simulation A0+GB2 , at $t = 24T_{\mathrm{bar}}$ (solid red). For comparison we show with the solid black line the average $v_R$ over all angles $\phi$ for the axisymmetric initial conditions ICTHIN, and with dashed lines corresponding to twice the standard deviation around this average. The top and bottom panels are for $z = 0$ kpc and $z = 1$ kpc respectively. The blue line in the top panel represents the average $v_R$ of thin disk particles $v_\phi < v_{\phi,\mathrm{OLR}}$ in volumes centered at $R = 8$ kpc as a function of $\phi$ for the LR simulation A0+GB2, at $t = 120T_{\mathrm{bar}}$ (solid blue).

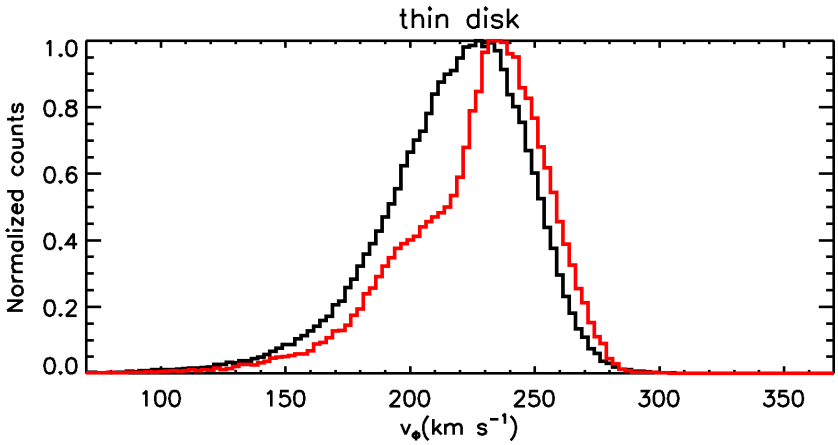


**Figure 2.10:** Distribution of thin disk stars in $v_\phi$ for the volume centered at $(R, \phi, z) = (8 \text{ kpc}, 0, 0)$ and for stars with $|v_R| < 30$ km s$^{-1}$. The red line represents the simulation A0+GB2, at $t = 24T_{\rm bar}$. The solid black line represents the axisymmetric initial conditions.

this oscillation is significantly above the noise level. Notice however how the curve is not perfectly symmetric: there is a wiggle for $-40° < \phi < 0$, and the amplitude is different between positive and negative $\langle v_R \rangle$. Because of the symmetry of the potential, we would expect instead $\langle v_R(\phi) \rangle = -\langle v_R(-\phi) \rangle$ and $\langle v_R(\phi) \rangle = \langle v_R(\pi + \phi) \rangle$, for each $\phi$. This happens because the disk has not reached a fully stationary equilibrium configuration at $R = 8$ kpc at this time (Fux 2001; Mühlbauer & Dehnen 2003). A much longer (and unrealistic) integration time of $120T_{\rm bar}$ ($\sim 15$ Gyr) is required to reach complete symmetry (Fig. 2.9, blue line). For volumes approximately aligned or perpendicular to the bar the OLR Mode has a null mean, that is the OLR Mode is centered. For these cases, however, the behavior is still significantly different from the axisymmetric case, as one can see directly in the right column of Fig. 2.8, at $R = 8$ kpc, where the bimodality, despite being centered with respect to $v_R$, is still present, and as shown in Fig. 2.10. In this figure we restrict the attention to those stars with $|v_R| < 30$ km s$^{-1}$, where the differences from the axisymmetric initial conditions are enhanced.

The vertex deviation $l_v$ quantifies the orientation of the velocity ellipsoid on the $z = 0$ plane. Following Binney & Merrifield (1998) this is:

$$l_{\rm v} \equiv \frac{1}{2} \arctan \left[ \frac{2\langle v_R \, (v_\phi - \langle v_\phi \rangle) \rangle}{\sigma_R^2 - \sigma_\phi^2} \right]. \tag{2.14}$$

The corresponding values are quoted in all panels of Fig. 2.8. In the Solar Neighborhood vicinity $l_{\rm v}$ is generally small. This means that the velocity ellipsoid is only slightly misaligned with the respect to the $v_R$ and $v_\phi$ axis. The vertex deviation behavior is fully quantified in Fig. 2.11. For $R = 8$ kpc, we see that $l_{\rm v}$ is positive for $\phi < 0$, null for $\phi = 0$ (volumes aligned with the bar), and negative for $\phi > 0$, until it changes again sign at $\phi = 90°$. This is consistent with the results of Mühlbauer & Dehnen (2003), who

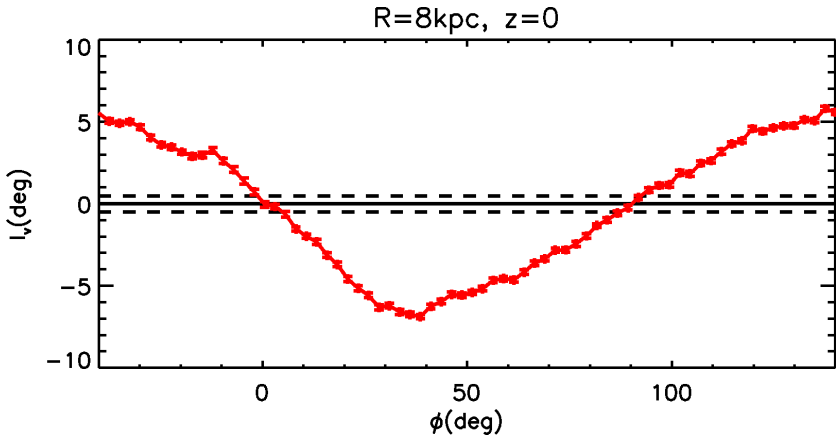


**Figure 2.11:** Vertex deviation in volumes centered at $R = 8$ kpc as a function of $\phi$. The description of the lines is the same of Fig. 2.9.

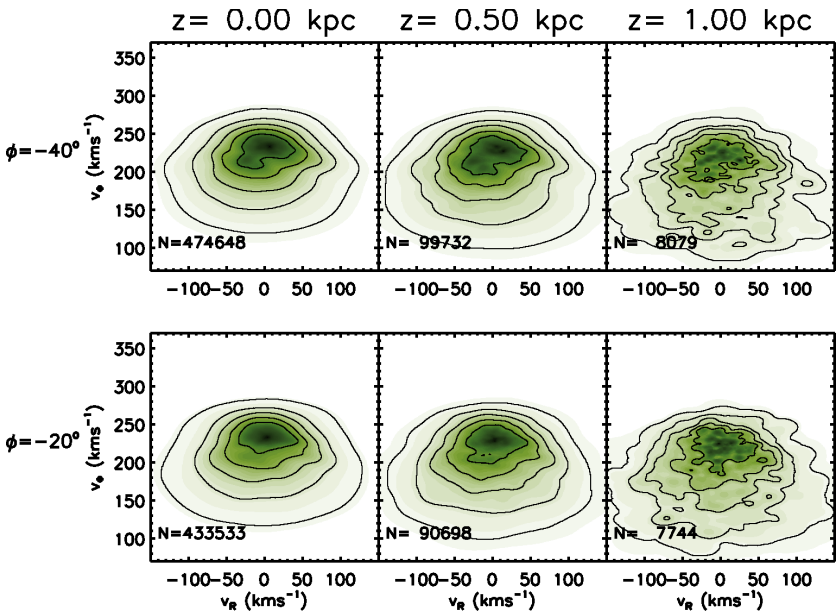


**Figure 2.12:** Kinematics of the thin disk HR simulation in the potential A0+GB2 in volumes centered at $R = 8$ kpc and $\phi = -20°$ and $\phi = -40°$ and $z = 0, 0.5, 1$ kpc (first, second and third column respectively).

showed that the bar can cause significant periodic perturbations in the velocity moments throughout the Galaxy for the 2D case.

Our 3D simulations offer us the unique opportunity to trace the disk kinematics far from the Galactic plane. In Fig. 2.12 we show the velocity distribution of the thin disk for the default bar model, for volumes at $R = 8$ kpc, at angles $\phi = -20^\circ$ (bottom row) and $\phi = -40^\circ$ (top row), but centered at different $z$. For both angles it is possible to trace the characteristic features (LSR and OLR Mode, Horn) present at $z = 0$, at least up to $z = 0.5$ kpc. the periodic oscillation of the average $v_R$ of the OLR Mode which is significant, even at this height. Periodicity is present also at $z = 1$ kpc (see lower panel of Fig. 2.9).

We mentioned in earlier sections how the relative strength of the bar slightly increases with $z$. It might be then not surprising to see effects of the bar at these heights. However the volumes at these heights are populated very differently than the ones located on the plane: the orbits are more eccentric, they have larger vertical amplitudes and they rotate more slowly in average ($\langle v_\phi(8 \text{ kpc}, 20^\circ, 0)\rangle - \langle v_\phi(8 \text{ kpc}, 20^\circ, 1 \text{ kpc})\rangle \sim 20$ km s$^{-1}$). It seems, however, that the differences in the velocity distributions at various heights are not much driven by the different types of orbits but mostly by the much smaller numbers of stars (and related Poisson noise) far from the plane.

### 2.3.3 Thick disk

Even in a hot and vertically extended population like the thick disk, it is still possible to recognize the dynamical imprints of the bar on its kinematics. Fig. 2.13 (equivalent for the thick disk to Fig. 2.8) shows that, for $\phi \leq 20^\circ$, we can find the Horn in all volumes (see the $1\sigma$ contour) at larger $v_\phi$ for decreasing $R$. At the same time, we can recognize the OLR Mode as a distinct feature with respect to the LSR mode in several volumes. Specifically, for $R = 8$ kpc and $R = 8.5$ kpc the 4th contour from inside shows a lack of stars at positive $v_R$ in the range 150 km s$^{-1} < v_\phi < 220$ km s$^{-1}$.

Fig. 2.13 also confirms that the bar effects are systematic and vary with the location of the volumes in the Galaxy, and that the main structures associated with the OLR Resonance (Horn, separation between LSR and OLR Mode), are still present as deformations in the 3rd, 4th and 5th contours from inside of the distributions. Fig. 2.14 (equivalent to Fig. 2.9 for the thin disk) indicates that, also in this case, the $v_R$ of the OLR Mode varies significantly, as a function of $\phi$. However, in the cases of volumes aligned with the bar ($\phi = 0$ and $\phi = 90^\circ$), where $\langle v_R\rangle \sim 0$ as in the axisymmetric case, the imprints of the bar on the $v_\phi$ distribution are not so clear as in the thin disk case, as Fig. 2.15 shows.

The vertical coherence of the kinematic structures in the thick disk is depicted in Fig. 2.16. The vertical extent of the thick disk allows us to have enough stars for this analysis, even at $z = 1$ kpc. The distributions are similar on the plane and for $z = 0.5$ kpc and $z = 1$ kpc. The Horn and the OLR Mode are present at the two angles, visible especially in the 2nd, 3rd and 4th contours. This is confirmed by the analysis of the mean $v_R$ of the OLR Mode (shown in the lower panels of Fig. 2.14). Even for $z = 2$ kpc, the periodicity of the mean $v_R$ of the OLR Mode is still noticeable.

We have repeated these analyses on the OLR Mode, both for the bar models GB1 and LB2, and found that the same periodicity can be observed, with a larger amplitude of the oscillations in the LB2 case.

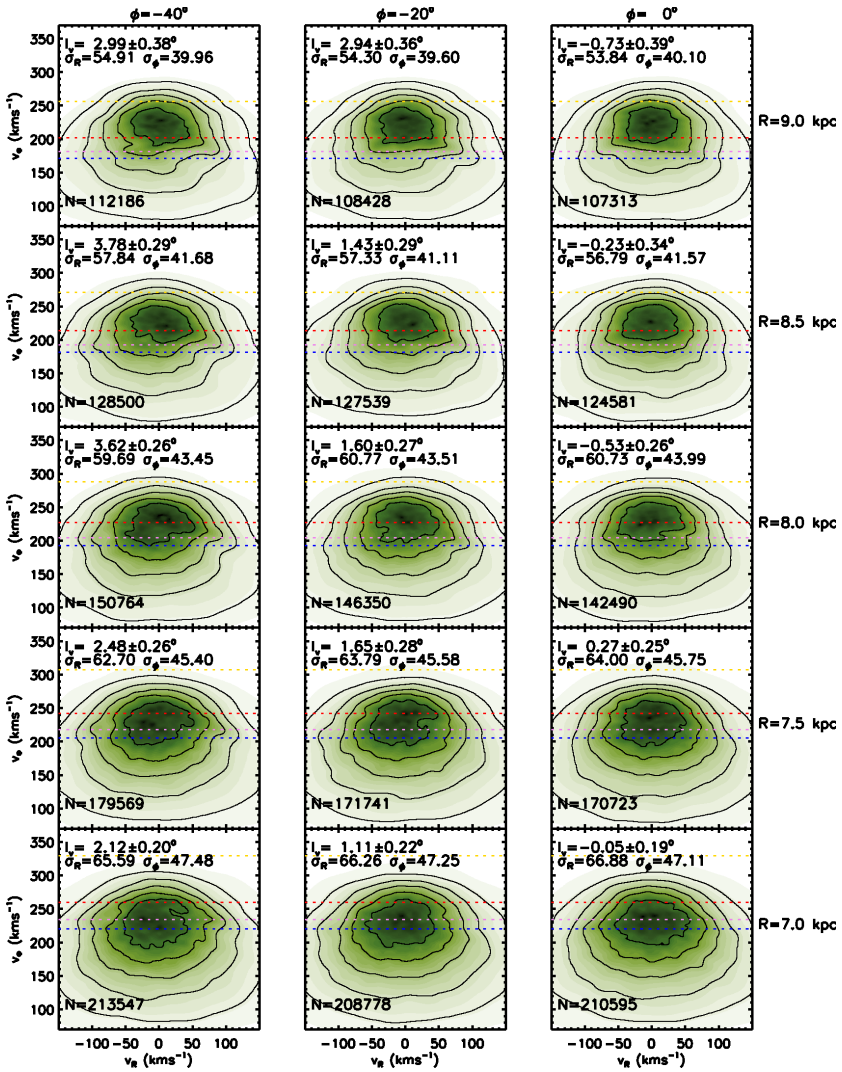


**Figure 2.13:** Kinematics of the simulated thick disk in the potential A0+GB2 in different volumes at $t = 24T_{\rm bar}$. As in Fig. 2.8 the columns correspond to volumes centered at different angles, and the rows to volumes centered at different Galactocentric radii. The dashed lines indicate to $v_{\phi,-1:1}$ (yellow), $v_{\phi,\rm OLR}$ (red), $v_{\phi,-3:1}$ (purple) and $v_{\phi,-4:1}$ (blue).

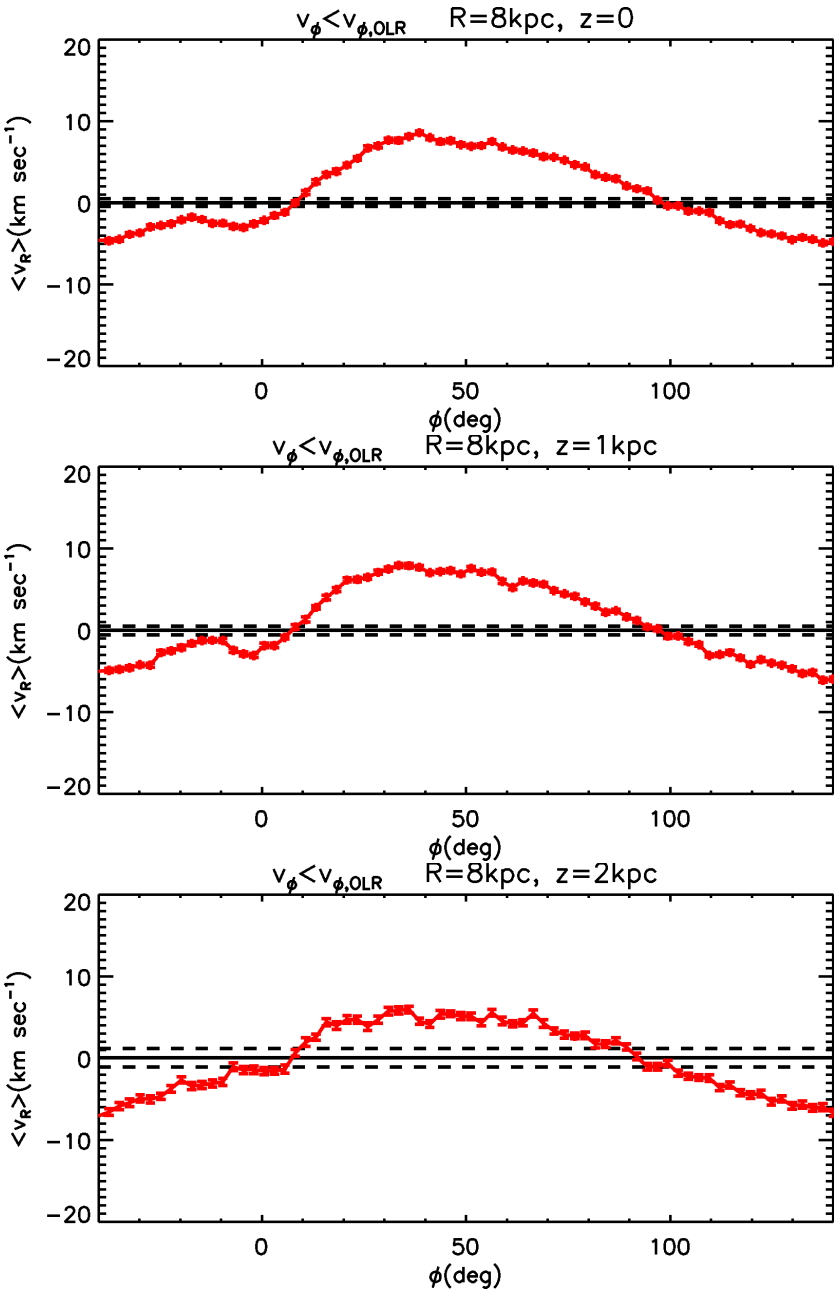


**Figure 2.14:** Average $v_R$ of thick disk particles $v_\phi < v_{\phi,\mathrm{OLR}}$ in volumes centered at $R = 8$ kpc as a function of $\phi$, for simulation A0+GB2, at $t = 24T_{\mathrm{bar}}$ (solid red). As in Fig. 2.9 we show for comparison the average (solid black) and twice the standard deviation (dashed black) $v_R$ for the axisymmetric initial conditions ICTHICK. The top, middle and bottom panels correspond to $z = 0$ kpc, $z = 1$ kpc and $z = 2$ kpc respectively.

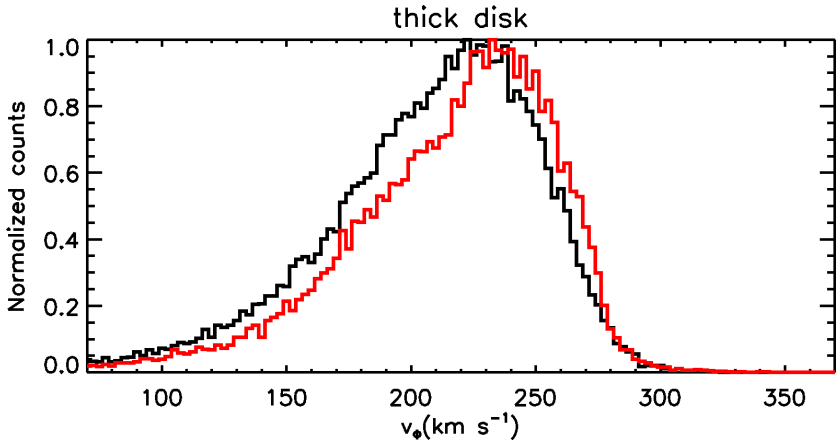


**Figure 2.15:** $v_\phi$-distribution of thick disk stars for the volume centered at $(R, \phi, z) = (8 \text{ kpc}, 0, 0)$ and for stars with $|v_R| < 30$ km s$^{-1}$. The red line represents the simulation A0+GB2, at $t = 24T_{\text{bar}}$. The solid black line represents the axisymmetric initial conditions.

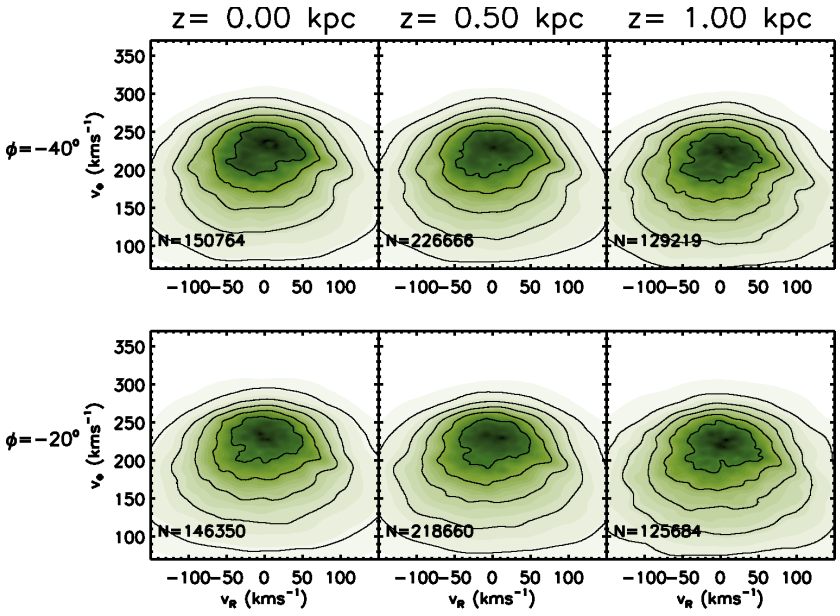


**Figure 2.16:** Kinematics of the thick disk simulation in the potential A0+GB2 in volumes centered at $R = 8$ kpc and $\phi = -20°$ and $\phi = -40°$ and $z = 0, 0.5, 1$ kpc (first, second and third column respectively). Notice that for $z > 0$, we can double the resolution using the volumes centered at $-|z|$.

### 2.3.4 Combination of thin and thick disk

In practice, surveys generally have a mix of both the thin and thick disk populations. This is why in Fig. 2.17 we show the velocity distribution of the thin and the thick disk together. Since the thick disk has 20% of the mass of the thin disk (Sect. 2.2.1), we combine the $5 \times 10^7$ particles of the thin disk for the A0+GB2 potential, with a random subsample of $10^7$ thick disk particles run in the same potential. As a result, in the volumes on the Galactic plane the number of stars of the thick disk is $\sim 10\%$ that of the thin disk. Fig. 2.17 shows how, in a sample of stars selected independently of the parent disk population, the imprints of the dynamics of the bar are easily detectable. In particular, we see how for $z = 0$ the distribution completely resembles that of the thin disk, while the thick disk, dominates the distribution at $z \geq 1$ kpc. All the main features, described in the previous figures (Horn, OLR Mode, LSR Mode) are easily detectable at every height.

## 2.4 Summary and discussion

In this work we have studied the 3D response of test particles, representing the thin and thick disk component of the Milky Way, to the Galactic gravitational field including a rotating central bar. Our goal was to understand if this non-axisymmetric component could induce moving groups, especially in the case when the vertical thickness of the Galaxy is taken into account.

We have found that the imprints of the bar are apparent both in a population resembling the intermediate/old population of the thin disk of the Milky Way and in a hot and vertically extended population resembling the thick disk. Thanks to our 3D simulations, this is the first time that such imprints have been traced far from the Galactic plane, up to $z \sim 1$ kpc in the thin disk and up to $z \sim 2$ kpc in the thick disk. These results are not strongly dependent on the bar models used, as all the simulations explored with different structural parameters (semi-major axes, vertical thickness and masses) yield similar results.

The effects of the bar that are seen in our simulations are clearly related to the resonant interaction between the rotation of the bar and the orbits of the stars in the disk. Many of the stellar particles in the vicinity of the Sun have orbits strongly affected by the bar's OLR of the bar. The OLR is apparent in a splitting of the simulated velocity distributions in two main groups. Our simulations also show that the impact of the OLR varies with position in the Galaxy, depending on Galactocentric radius and angle from the major axis of the bar. On a larger scale, the characteristics of the velocity distributions are periodic with respect to the orientation angle of the bar, tracing the symmetries of the bar's potential. This is manifested, for instance, on the vertex deviation around the Solar radius and in the mean radial velocity of the OLR groups.

In this sense our work agrees with previous results on the effects of the OLR of the bar on the kinematics of stars in the Solar Neighborhood (Dehnen 2000; Fux 2001; Mühlbauer & Dehnen 2003; Gardner & Flynn 2010). The main difference is that our simulations are more realistic as they are 3D and incorporate both a thin and a thick disk. For the analyses we have considered volumes of finite spatial extent (as in the observations) in contrast to the previous studies, which studied velocity distributions in a single point in the configuration space. Due to this difference as well as our longer integration times,

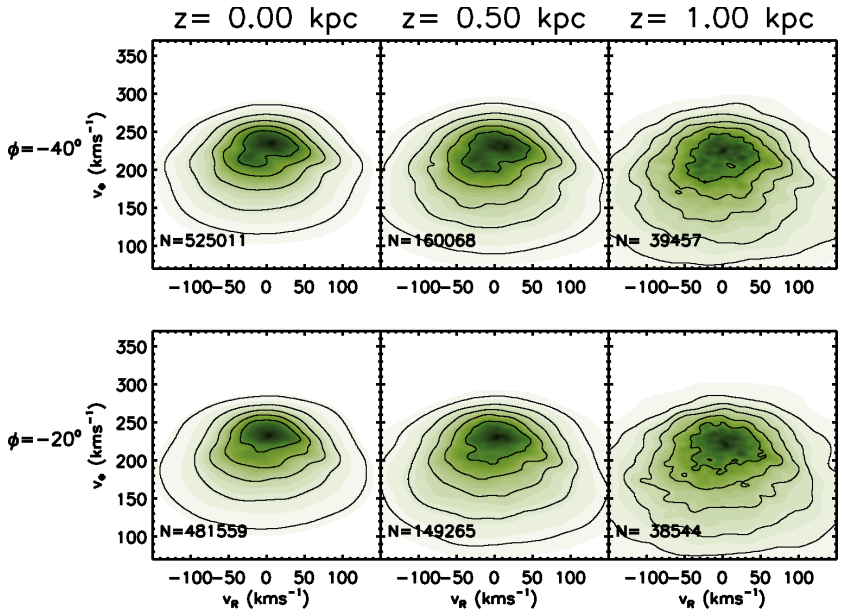


**Figure 2.17:** Kinematics of the thin and thick disk simulations together in the potential A0+GB2, in volumes centered at $R = 8$ kpc and $\phi = -20°$ and $\phi = -40°$ and $z = 0, 0.5, 1$ kpc (first, second and third column respectively). This is obtained combining $5 \times 10^7$ thin disk particles with a a random subsample of $10^7$ thick disk particles, so that the thick-to-thin density normalization at $z = 0$ is $\sim 10\%$.

we find in our volumes more diffuse kinematic structures, less sharp than if the velocity distributions were evaluated at points in space.

The presence of structures at large heights above the plane may also be understood from the fact that near the Sun the forces along the polar radius direction do not vary strongly with height, and certainly much less than the vertical forces. This implies that resonant features in the $v_R - v_\phi$ velocity plane, even at large heights from the plane, are expected. Our 3D simulations have shown that even in these regions of the Galaxy where a large fraction of stars have horizontal and vertical motions that are not decoupled, and the orbital eccentricity is large (especially for the thick disk), the bar significantly transforms the velocity distribution, in a similar way as on the plane.

We detect strong transient effects for approximately 10 bar rotation periods after the bar is introduced. Short integration times, like in e.g., Dehnen (2000), produce much clearer bar signatures. However, we believe that it is unlikely that an old population would have experienced the bar for such a short time scale.

Our simulations offer an explanation for the discovery that several of the observed kinematic groups in the Solar Neighborhood are also present far below the plane of Galaxy ($z \sim -0.7$ kpc, Antoja et al. 2012). If some of these kinematic groups are a direct consequence of the bar gravitational force (like, e.g., the Hercules group seems to be), our results show that it is not surprising to be able to recognize them far from the

Galactic plane. Moreover, our simulations predict that, depending on the location of the Sun in the Galaxy and with the respect to the bar, some imprints of the bar should be recognizable even beyond these heights.

Although we find kinematic structures in the thick disk, the Arcturus stream does not appear in our simulations for our default (long) integration times. This moving group is expected at $v_\phi \sim 134$ km s$^{-1}$ in the Solar Neighborhood of our simulations ($V \sim 100$ km s$^{-1}$ in Williams et al. 2009). However, for short integration times and the long bar model, we can identify the same structures and distortions in the low $v_\phi$ tail of the kinematic distribution in our thin disk, already associated to Arcturus by Gardner & Flynn (2010). Our simulations seem to suggest that, if the Arcturus stream is an imprint of the bar, the bar should be very young. However, the lack of overdensity in the Arcturus region for longer times could also be a reflection of the choice of the initial conditions of our simulations if we are to associate it to a non-axisymmetry of the potential rather than an accreted origin.

One important assumption of this work is that the the pattern speed (and other properties) of the bar has not changed in the last $\sim 3$ Gyr. A change in the pattern speed should result in a change in the resonances, and in which stars are affected. But whether this evolution would produce more or less bar signatures on the disk phase-space remains to be seen.

Finally, as shown in Solway et al. (2012), the spiral arms induce angular momentum changes that affect not only the thin but also the thick disk. This suggests that spiral arms may also produce kinematic signatures on the thick disk like those induced by the bar and studied here. It would be interesting to quantify the relative importance of the effects of spiral arm resonances with respect to the bar's.

In our upcoming paper we will present a more exhaustive quantification of the substructures and the bar effects and a dynamical interpretation of the results based on the orbital frequency analysis.

The results obtained in this study unveil a more complex and structure-rich thick disk, which has been likely affected not only by accretion events but also by secular evolution induced by the disk's non-axisymmetries such as the bar and spiral arms.

## Acknowledgments

The authors gratefully acknowledge support from the European Research Council under ERC Starting Grant GALACTICA-240271. We also thank H. Buddelmeijer for the density estimator code.

Chapter 3

# 3D test particle simulations of the Galactic disks II. The effects of the bar in frequency space.

Based on Monari, Helmi & Antoja (2014).
In preparation.


## Abstract

The Galactic bar can be described as a small perturbation onto the axisymmetric potential that represents most of the mass in the Milky Way. With the help of Perturbation Theory we define resonant trapping and study the regions of velocity space occupied by trapped orbits for a simple 2D model of the Milky Way. Then we extend our analysis to the 3D simulations presented in Chapter 2, using Fourier frequency analysis to classify orbits trapped to resonances and to identify irregular orbits. For our default bar model, we find that roughly 16% of orbits are trapped to resonances in our simulations and that they create features in the velocity distribution. The fraction of orbits trapped to horizontal ($\Omega_R : \Omega_\phi = n : m$) resonances and their characteristics do not depend on height from the Galactic plane but rather on the angle from the bar and distance from the Galactic center. The fraction of orbits trapped to the vertical resonances ($\Omega_R : \Omega_z = n : m$, $\Omega_\phi : \Omega_z = n' : m'$) instead grows as the height increases. We explore two additional bar models and find that the main difference resides in the number of trapped and irregular orbits, and this is directly related to the strength of the perturbation.

## 3.1 Introduction

The problem of understanding the effects of non-axisymmetric perturbations like the Galactic bar or spiral arms on the dynamics of stars in the Milky Way (or in other galaxies) has been studied on numerous occasions. Through resonant effects the bar and spiral arms can modify significantly the phase-space distribution of the stars in galaxies. This leads to the expectation that there is a one-to-one relationship between these effects and the characteristics of the perturbation, as if phase-space would have a characteristic signature of the bar or the spiral arms near the resonances. Therefore, by studying the phase-space distribution of stars even far from the perturbation, we can know its parameters (e.g., pattern speed, mass, geometry), as well as obtain information about the characteristic parameters of the Galaxy as a whole (e.g., its circular speed curve).

The first works on this subject were mostly analytical. In a series of papers from the '70s - '80s (Contopoulos 1975; Contopoulos & Mertzanides 1977; Contopoulos 1979; Contopoulos & Papayannopoulos 1980; Contopoulos 1981; Contopoulos & Grosbol 1986) 2D perturbation theory models were used. These authors studied the orbits induced by some simple bar or spiral arm potentials rotating with a constant pattern speed, and introduced a terminology to classify the periodic orbits ($x_i$ orbits) that is still widely used. Contopoulos (1979) also studied the *density* response of the stars in a galaxy near the Inner Lindblad Resonance associated to a spiral pattern. Along similar lines, using also 2D perturbation theory, Weinberg (1994) studied the *kinematic* response (mean velocity and dispersion) of the Galactic disk, near Corotation, Inner and Outer Lindblad resonances to a bar perturbation with variable pattern speed. Kuijken & Tremaine (1991) studied the kinematic response of a disk to a more general class of perturbations, as function of the angle from the perturbation. Finally, Kalnajs (1991) proposed that the different orbital families induced by the bar could create distinctive signatures in the kinematics of the stars in the Solar Neighborhood.

A big impulse to the topic came from the systematic exploration of the kinematics of stars in the Solar Neighborhood, after the launch of the *Hipparcos* mission. The Solar Neighborhood was found to be rich in substructures (Dehnen 1998), composed by stars that not always had the same age and chemical composition (Famaey et al. 2005). Therefore it was believed that many of them could have their origin in the resonant effects of the bar or the spiral arms, as in Kalnajs (1991) hypothesis.

Since *Hipparcos*, and with the advances in computational power, different authors tried to fit the observed kinematics with numerical simulations of the Milky Way using models including the bar (Dehnen 2000; Fux 2001), the spiral arms (De Simone et al. 2004; Antoja et al. 2011), or both (Antoja et al. 2009; Quillen et al. 2011). Further insights from analytic models were obtained by, e.g., Quillen (2003) who studied the chaos in the Solar Neighborhood due to overlap between the bar and the spiral arms resonances. Sellwood (2010) studied the distribution of stars of the *Geneva-Copenhagen* survey in the angle coordinates of a spherical 2D model and McMillan (2011, 2013) tried to fit an analytical distribution function composed by an axisymmetric phase-mixed part and a non-mixed resonant term due to a spiral perturbation to the *RAVE* observations, in order to explain the Hyades moving group.

This Chapter complements the study presented in Chapter 2 on the effects of the bar on the Galactic disk. We focus here on the resonant trapping induced by the bar, and the relation to the local kinematic structures present in the velocity distribution. We

first approach this problem with the help of perturbation theory for a simple 2D model of the Galaxy, in order to define the resonant trapping and get insight into the dynamics. Then we turn to our 3D test particle simulations. We perform a Fourier analysis of the orbits of stars across the whole disk. This allows to quantify the presence of resonances also far from the Galactic plane as well as to test the validity of the 2D analytic model.

In Sect. 3.2 we describe the dynamics of the problem using the Perturbation Theory in 2D and we predict the location of the orbits trapped to the resonances at different positions in the Galactic disk. In Sect. 3.3 we explain the Fourier transform method used to obtain the orbits' frequencies in our numerical experiments. In Sect. 3.4 we present the results obtained with the frequency analysis and in Sect. 3.5 we conclude.

## 3.2 Dynamics near the resonances

### 3.2.1 Generalities

The Milky Way contains a bar and spiral arms. Their gravitational potential can be described as a small perturbation onto an axisymmetric background, i.e, $\Phi(R,z) = \Phi_0(R,z) + \Phi_\mathrm{b}(R,\phi,z)$, where $(R,\phi,z)$ are the usual cylindrical coordinates and $\Phi_\mathrm{b}$ is the perturbation. We can write the Hamiltonian of the problem as

$$H\left(\boldsymbol{J}\right) = H_0\left(\boldsymbol{J}\right) + \delta H(\boldsymbol{J},\boldsymbol{\theta}), \tag{3.1}$$

where $H_0$ is the term governing the dynamics in the unperturbed background potential (that we assume to be integrable), $\delta H = \Phi_\mathrm{b}$ the perturbation, and $(\boldsymbol{J},\boldsymbol{\theta})$ a set of actions and angles for $H_0$. The angles $\boldsymbol{\theta}$ evolve in $H_0$ with frequencies $\boldsymbol{\Omega} = \partial H_0/\partial \boldsymbol{J}$. The resonances are defined using the frequencies as

$$\mathbf{l}\cdot\boldsymbol{\Omega} = 0, \tag{3.2}$$

where $\mathbf{l}$ is a vector of integers.

Near a resonance, like that described by Eq. (3.2), we can define a new set of angle-action coordinates more appropriate for the study of the perturbed problem. This, in $N$ dimensions, is done via the canonical transformation $(\boldsymbol{J},\boldsymbol{\theta}) = (\{J_1,...,J_N\},\{\theta_1,...,\theta_N\}) \rightarrow (\boldsymbol{I},\boldsymbol{\phi}) = (\{I_\mathrm{s},I_\mathrm{f1},...,I_{\mathrm{f},N-1}\},\{\phi_\mathrm{s},\phi_\mathrm{f1},...,\phi_{\mathrm{f},N-1}\})$,

$$\begin{array}{ll}
\phi_\mathrm{s} = \mathbf{l}\cdot\boldsymbol{\theta}, & J_1 = l_1 I_\mathrm{s} + I_\mathrm{f1} \\
\phi_\mathrm{f1} = \theta_1, & J_2 = l_2 I_\mathrm{s} + I_\mathrm{f2} \\
... & \\
\phi_{\mathrm{f},N-2} = \theta_{N-2}, & J_{N-1} = l_{N-1} I_\mathrm{s} + I_{\mathrm{f},N-1} \\
\phi_{\mathrm{f},N-1} = \theta_{N-1}, & J_N = l_N I_\mathrm{s}.
\end{array} \tag{3.3}$$

The angle $\phi_\mathrm{s}$ is called "slow angle", because near the resonance it evolves at a frequency $\Omega_\mathrm{s} = \mathbf{l}\cdot\boldsymbol{\Omega} \approx 0$.

It can be shown (Kaasalainen 1994; Binney & Tremaine 2008, see also Eq. (3.24b) below) that near to the resonance the equation of motion of $\phi_\mathrm{s}$ is approximately that of a pendulum. The energy of the pendulum is

$$E_\mathrm{p} = \frac{1}{2}\dot{\phi_\mathrm{s}}^2 + V_\mathbf{l}(\phi_\mathrm{s}), \tag{3.4}$$

where the potential $V_{\rm l}(\phi_{\rm s})$ is different for each resonance. If $E_{\rm p} \geq \max(V_{\rm l})$ then $\phi_{\rm s}$ circulates (i.e., it always increases with time), else $\phi_{\rm s}$ librates (i.e., it oscillates between two values). In this latter case the orbit is said to be "trapped to the resonance".

### 3.2.2 Perturbation theory: a simple case

In this Section we apply the formalism just introduced to a very simple case, to get insight into the dynamics induced by the bar as it perturbs the motions of stars in the Galactic disk.

Following Weinberg (1994), we study the problem in two dimensions, assuming that the background potential corresponds to that of a galaxy with a flat rotation curve with circular speed $v_0$,

$$\Phi_0(R) = v_0^2 \ln\left(\frac{R}{R_0}\right). \tag{3.5}$$

We assume that the bar perturbation rotates with constant pattern speed $\Omega_{\rm b}$ and to be a pure quadrupole, i.e.,

$$\Phi_{\rm b}(R,\phi) = {\rm Re}\left\{U_2(R){\rm e}^{i2(\phi-\Omega_{\rm b}t)}\right\}, \tag{3.6}$$

where

$$U_2(R) = -\epsilon v_0^2 \begin{cases} (R/r_{\rm b})^2 & \text{if } R < r_{\rm b} \\ (R/r_{\rm b})^{-3} & \text{if } R \geq r_{\rm b}. \end{cases} \tag{3.7}$$

Here $(R,\phi)$ are polar coordinates, with $\phi$ measured from the long axis of the bar, $r_{\rm b}$ is the dimension of the bar and $\epsilon$ denotes the amplitude of the perturbation compared to the background potential, which itself is proportional to $v_0^2$ (see Eq. 3.5).

We study the problem in the epicyclic approximation (Binney & Tremaine 2008) i.e., we assume that the orbits of stars in the disk are not too eccentric. In this case Eq. (3.1) reads

$$H = H_0\left(J_R, J_\phi\right) - \Omega_{\rm b} J_\phi + \delta H\left(J_R, J_\phi, \theta_R, \theta_\phi\right). \tag{3.8}$$

$H$ is often referred to as "Jacobi Integral" and $H_0$ is the Hamiltonian of the potential responsible for the flat rotation curve. The coordinates $(J_R, J_\phi, \theta_R, \theta_\phi)$ are action angle coordinates in the unperturbed Hamiltonian. In particular $J_\phi$ is the angular momentum. The angular frequencies are

$$\dot{\theta}_R = \kappa, \quad \dot{\theta}_\phi = \Omega, \tag{3.9}$$

where $\kappa(R)$ and $\Omega(R)$ are the epicyclic and circular frequency respectively[1]. The effective background Hamiltonian is in this case $H_0^{\rm eff}\left(J_R, J_\phi\right) \equiv H_0\left(J_R, J_\phi\right) - \Omega_{\rm b} J_\phi$, and Eq. (3.2) can be expressed as

$$l_R \kappa + l_\phi\left(\Omega - \Omega_{\rm b}\right) = 0, \tag{3.10}$$

where $l_R$ and $l_\phi$ are integers. The canonical transformation given by Eq. (3.3), becomes

$$\begin{array}{ll} \phi_{\rm s} = l_R\theta_R + l_\phi\left(\theta_\phi - \Omega_{\rm b}t\right), & J_R = l_R I_{\rm s} + I_{\rm f}, \\ \phi_{\rm f} = \theta_R, & J_\phi = l_\phi I_{\rm s}. \end{array} \tag{3.11}$$

[1] We consider here Lindblad's version of the epicyclic theory, used also in Lynden-Bell & Kalnajs (1972) and Weinberg (1994). In this version the $(J_R, J_\phi, \theta_R, \theta_\phi)$ coordinates are not canonical. To make them canonical (and obtain a more accurate representation of the orbits) one should use $\dot{\theta}_\phi = \Omega + \frac{{\rm d}\kappa}{{\rm d}J_\phi}$ and add a (small) term $\propto \sin 2\theta_R$ to $f(\theta_R)$ in Eq. (3.15) (Dehnen 1999).

The perturbation $\delta H$ is cyclic in the $(\phi_\mathrm{s}, \phi_\mathrm{f})$ angles (as these are combinations of the $(\theta_\phi, \theta_R)$ angles) so $\delta H$ can be expanded in a Fourier series as

$$\delta H = \Phi_\mathrm{b} = \mathrm{Re}\left\{\sum_{j=-\infty}^{\infty}\sum_{k=-\infty}^{\infty} h_{jk}(I_\mathrm{s}, I_\mathrm{f}) \exp\left[i(j\phi_\mathrm{f} + k\phi_\mathrm{s})\right]\right\}. \tag{3.12}$$

At this point we argue that any term in the sum that contains $\phi_\mathrm{f}$ has a negligible effect on the dynamics: these terms give rise to forces that rapidly average to zero (Binney & Tremaine 2008). We therefore drop all the terms in the $j$-sum in Eq. (3.12), except $j = 0$. Therefore,

$$\delta H = \mathrm{Re}\left\{U_2(R)\mathrm{e}^{i2(\phi-\Omega_\mathrm{b}t)}\right\} \approx \mathrm{Re}\left\{\sum_{k=-\infty}^{\infty} h_k(I_\mathrm{s}, I_\mathrm{f})\mathrm{e}^{ik\phi_\mathrm{s}}\right\}, \tag{3.13}$$

where

$$h_k \equiv h_{0k} = \frac{1}{(2\pi)^2}\int_0^{2\pi}\int_0^{2\pi} \mathrm{d}\phi_\mathrm{f}\mathrm{d}\phi_\mathrm{s} U_2(R)\mathrm{e}^{i2(\phi-\Omega_\mathrm{b}t)}\mathrm{e}^{-ik\phi_\mathrm{s}}. \tag{3.14}$$

To estimate $h_k$ we write the deviation of the azimuthal position of the star $\phi$ from its guiding center $\theta_\phi$, as

$$f(\theta_R) \equiv \theta_\phi - \phi. \tag{3.15}$$

In the epicyclic approximation

$$f(\theta_R) = -\frac{\Omega(R_\mathrm{g})}{\kappa(R_\mathrm{g})}\frac{2a}{R_\mathrm{g}}\sin\theta_R, \tag{3.16}$$

where $R_\mathrm{g} = J_\phi/v_0$ is the guiding center radius and $a$ is the amplitude of the epicyclic motion. From Eq. (3.11), $\theta_\phi = \phi_\mathrm{s}/l_\phi - l_R\theta_R/l_\phi + \Omega_\mathrm{b}t$, $\phi_\mathrm{f} = \theta_R$, and therefore

$$\begin{aligned} h_k &= \frac{1}{(2\pi)^2}\int_0^{2\pi}\int_0^{2\pi} \mathrm{d}\theta_R\mathrm{d}\phi_\mathrm{s} U_2(R)\mathrm{e}^{i2\left[\frac{\phi_\mathrm{s}}{l_\phi} - \frac{l_R}{l_\phi}\theta_R - f(\theta_R)\right]}\mathrm{e}^{-ik\phi_\mathrm{s}} = \\ &= \frac{c_2(l_\phi, k)}{(2\pi)^2}\int_0^{2\pi}\mathrm{d}\theta_R U_2(R)\mathrm{e}^{-i2\left[\frac{l_R}{l_\phi}\theta_R + f(\theta_R)\right]}, \end{aligned} \tag{3.17}$$

where

$$c_2(l_\phi, k) = \begin{cases} \frac{\mathrm{e}^{i\left(\frac{2}{l_\phi}-k\right)2\pi}-1}{i\left(\frac{2}{l_\phi}-k\right)} & \text{if } kl_\phi \neq 2 \\ 2\pi & \text{if } kl_\phi = 2. \end{cases} \tag{3.18}$$

If $l_\phi \leq 2$, $c_2(l_\phi, k) = \delta_{2,l_\phi k}$. The integrand in Eq. (3.17) is an even function of $\theta_R$, therefore

$$h_k = \frac{c_2(l_\phi, k)}{2\pi^2}\int_0^{\pi}\mathrm{d}\theta_R U_2(R)\cos\left\{2\left[\frac{l_R}{l_\phi}\theta_R + f(\theta_R)\right]\right\}. \tag{3.19}$$

Using the perturbed slow and fast actions we can re-write Eq. (3.8) as

$$H = H_0(I_\mathrm{s}, I_\mathrm{f}) - l_\phi\Omega_\mathrm{b}I_\mathrm{s} + \mathrm{Re}\left\{\sum_{k=-\infty}^{\infty} h_k\mathrm{e}^{ik\phi_\mathrm{s}}\right\}. \tag{3.20}$$

If we expand the effective background Hamiltonian $H_0^{\rm eff} = H_0 - l_\phi \Omega_{\rm b} I_{\rm s}$ around the value of $I_{\rm s}$ at the resonance we obtain

$$H_0^{\rm eff} \approx H_0^{\rm eff}(I_{\rm f}, I_{\rm s,res}) + \frac{\partial H_0^{\rm eff}}{\partial I_{\rm s}}\Big|_{\rm res}(I_{\rm s} - I_{\rm s,res}) + \frac{1}{2}\frac{\partial^2 H_0^{\rm eff}}{\partial I_{\rm s}^2}\Big|_{\rm res}(I_{\rm s} - I_{\rm s,res})^2 . \tag{3.21}$$

The second term in this expansion is null because $\partial H_0^{\rm eff}/\partial I_{\rm s} = \Omega_{\rm s}$, which is exactly zero at the resonance. At this point we assume $I_{\rm f}$ constant, as its evolution is adiabatic. The effective one-dimensional Hamiltonian that governs the motion in the $(I_{\rm s}, \phi_{\rm s})$ plane then becomes

$$\hat{H} = \frac{1}{2}\frac{\partial \Omega_{\rm s}}{\partial I_{\rm s}}\Big|_{\rm res}(I_{\rm s} - I_{\rm s,res})^2 + {\rm Re}\left\{\sum_{k=-\infty}^{\infty} h_k {\rm e}^{ik\phi_{\rm s}}\right\}. \tag{3.22}$$

Hamilton's equations in this case read

$$\dot{I}_{\rm s} = {\rm Re}\left\{ i \sum_{k=-\infty}^{\infty} k h_k(I_{\rm s}) {\rm e}^{ik\phi_{\rm s}}\right\}, \tag{3.23a}$$

$$\dot{\phi}_{\rm s} = \frac{\partial \Omega_{\rm s}}{\partial I_{\rm s}}\Big|_{\rm res}(I_{\rm s} - I_{\rm s,res}) + {\rm Re}\left\{\frac{\partial h_k}{\partial I_{\rm s}} {\rm e}^{ik\phi_{\rm s}}\right\}, \tag{3.23b}$$

and

$$\ddot{\phi}_{\rm s} \approx \frac{\partial \Omega_{\rm s}}{\partial I_{\rm s}}\Big|_{\rm res}\dot{I}_{\rm s}, \tag{3.24a}$$

$$\ddot{\phi}_{\rm s} \approx \frac{\partial \Omega_{\rm s}}{\partial I_{\rm s}}\Big|_{\rm res}{\rm Re}\left\{ i \sum_{k=-\infty}^{\infty} k h_k(I_{\rm s}) {\rm e}^{ik\phi_{\rm s}}\right\}, \tag{3.24b}$$

where in the last equation we have neglected the terms proportional to powers of $\epsilon$ larger or equal than 2 (recall that $h_k \propto \epsilon$). Eq. (3.24b) is the pendulum equation that governs the motion of the slow angle $\phi_{\rm s}$. In this case

$$V(\phi_{\rm s}) = {\rm Re}\left\{\sum_{k=-\infty}^{\infty} \frac{\partial \Omega_{\rm s}}{\partial I_{\rm s}} h_k {\rm e}^{ik\phi_{\rm s}}\right\}. \tag{3.25}$$

The angle $\phi_{\rm s}$ represents the precession of the orbit i.e., it describes the angle from the long axis of the bar recorded at the apocenters (relative maxima in $R$). A trapped orbit precesses back and forward between two values of $\phi_{\rm s}$. Integrating Eq. (3.24a) with respect to the time variable $t$, we find

$$I_{\rm s}(t) = I_{\rm s}(0) + \left(\frac{\partial \Omega_{\rm s}}{\partial I_{\rm s}}\Big|_{\rm res}\right)^{-1}\left[\dot{\phi}_{\rm s}(t) - \dot{\phi}_{\rm s}(0)\right], \tag{3.26}$$

and, since $I_{\rm s} = R^2\dot{\phi}/l_\phi$, then

$$R^2(t) = \frac{1}{\dot{\phi}(t)}\left\{ J_\phi(0) + l_\phi\left(\frac{\partial \Omega_{\rm s}}{\partial I_{\rm s}}\Big|_{\rm res}\right)^{-1}\left[\dot{\phi}_{\rm s}(t) - \dot{\phi}_{\rm s}(0)\right]\right\}. \tag{3.27}$$

From Eq. (3.11) and Eq. (3.15) we see that

$$\dot{\phi} = \dot{\phi}_{\rm ep}(\theta_R) + \Delta\dot{\phi}(\phi_{\rm s}), \tag{3.28}$$

**Table 3.1:** Color coding of orbits trapped to the resonances in the plots of this work, defined by the indices $l_R$, $l_\phi$ and $l_z$.

| $(l_R, l_\phi, l_z)$ | Color |
|---|---|
| $(1, 1, 0)$ | Yellow |
| $(1, 2, 0)$ | Red |
| $(1, 3, 0)$ | Purple |
| $(1, 4, 0)$ | Blue |
| $(3, 0, 2)$ | Light green |
| $(1, 0, 1)$ | Orange |
| $(1, 0, 2)$ | Dark green |
| $(0, 1, 1)$ | Gray |
| All | Black |
| Irregular | Light blue |

where we have defined $\dot{\phi}_{\rm ep} \equiv \Omega - f'(\theta_R)\kappa$ (the value of $\dot{\phi}$ without the bar perturbation in the epicyclic approximation) and $\Delta\dot{\phi} \equiv \dot{\phi}_{\rm s}/l_\phi - l_R\kappa/l_\phi + \Omega_{\rm b} - \Omega$. Since $\dot{\phi}_{\rm ep} \gg \Delta\dot{\phi}$

$$\begin{aligned} R^2 &\approx \frac{J_\phi(0)}{\dot{\phi}_{\rm ep}(\theta_R)} - l_\phi \left( \frac{\partial \Omega_{\rm s}}{\partial I_{\rm s}}\Big|_{\rm res} \right)^{-1} \frac{\dot{\phi}_{\rm s}(t) - \dot{\phi}_{\rm s}(0)}{\dot{\phi}_{\rm ep}(\theta_R)} = \\ &= \frac{J_\phi(0)}{\dot{\phi}_{\rm ep}(\theta_R)} - l_\phi \left( \frac{\partial \Omega_{\rm s}}{\partial I_{\rm s}}\Big|_{\rm res} \right)^{-1} \frac{\sqrt{E_{\rm p} - V(\phi_{\rm s})} - \dot{\phi}_{\rm s}(0)}{\dot{\phi}_{\rm ep}(\theta_R)}. \end{aligned} \tag{3.29}$$

From Eq. (3.29) we see that the motion in $R$ is composed by an "epicyclic" unperturbed part, dependent only on $\theta_R$ and a part depending also on the $\phi_{\rm s}$ angle. Hence, $R$ is the combination of two periodic motions. Depending on the value of $\phi_{\rm s}$, the orbit will be more or less elongated in the $R$ direction. In particular, for orbits with guiding center radius $R_{\rm g}$ inside the Outer Lindblad Resonance (OLR, $l_R = 1$, $l_\phi = 2$), the orbits are most elongated in $R$ when $\phi_{\rm s} = \pm\pi/2$ and for orbits outside the OLR at $\phi_{\rm s} = 0$ (see Fig. 3.1 and Weinberg 1994).

### 3.2.3 Resonances and velocity space

In Fig. 3.2 we assume $v_0 = 220$ km s$^{-1}$, $\Omega_{\rm b} = 50$ km s$^{-1}$ kpc$^{-1}$, $r_{\rm b} = 3.5$ kpc and $\epsilon = 0.05,\ 0.1$, and we compute $E_{\rm p} - \max(V)$ for orbits passing through the given $(R, \phi)$ locations with velocities $(v_R, v_\phi) = (-\dot{R}, R\dot{\phi})$. The contours represent $E_{\rm p} - \max(V) = 0$ for different combinations of $(l_R, l_\phi)$ (see Table 3.1 for the color coding). Orbits inside these contours are, according to the perturbation theory, trapped to the corresponding resonance. We see how these contours enclose regions that look like islands in the $(v_R, v_\phi)$ space.

In the top left panel of Fig. 3.2 we have assumed $(R, \phi) = (8\ {\rm kpc}, -20^\circ)$ while in the top right plot we assume $(R, \phi) = (8\ {\rm kpc}, 0)$ for $\epsilon = 0.05$. From the comparison of these two plots we see how the angle from the bar $\phi$ affects the location of the islands. In particular, at $\phi = 0$ the islands are completely symmetric with the respect to the $v_R = 0$ axis, while at $(R, \phi) = (8\ {\rm kpc}, -20^\circ)$ they are asymmetric. Let us for example consider

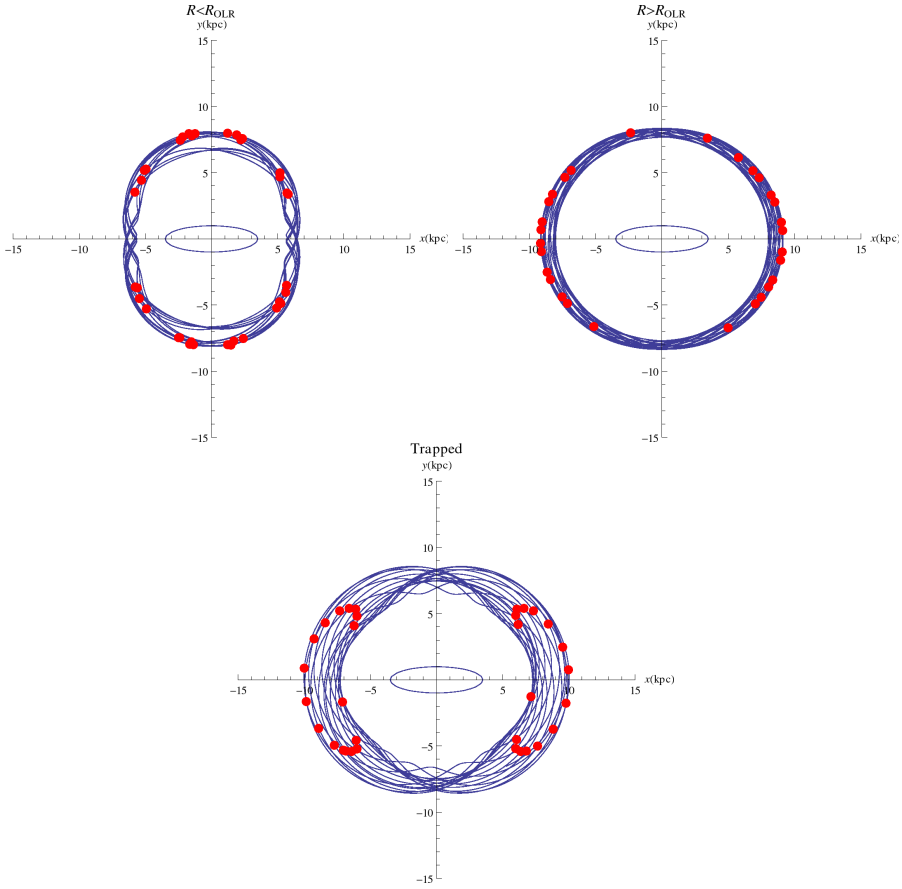


**Figure 3.1:** Orbits integrated in the potential $\Phi_0 + \Phi_b$ given by Eqs. (3.5)-(3.7) for $t \approx 1$ Gyr and in the frame of reference corotating with the bar. The red dots correspond to the position of the apocenters, the local maxima of $R(t)$. The ellipse in the center of the plot represents the bar. Top: examples of orbits not trapped to a resonance for $R_g < R_{OLR}$ (left) and $R_g > R_{OLR}$ (right). Bottom: an orbit trapped to the $(l_R, l_\phi) = (1, 2)$ (OLR) resonance. The azimuth $\phi$ of the apocenters is equivalent to the slow angle $\phi_s$. In the non-trapped cases the apocenter circulates around the center, while in the trapped case it oscillates between two angles. Moreover, in the non-trapped cases $R$ at the apocenters is maximum at $\phi_s = 0$ ($\phi_s = \pm 90°$) for $R_g > R_{OLR}$ ($R_g < R_{OLR}$). For the trapped orbits $R$ at the apocenters is maximum and minimum at $\phi_s = 0$.

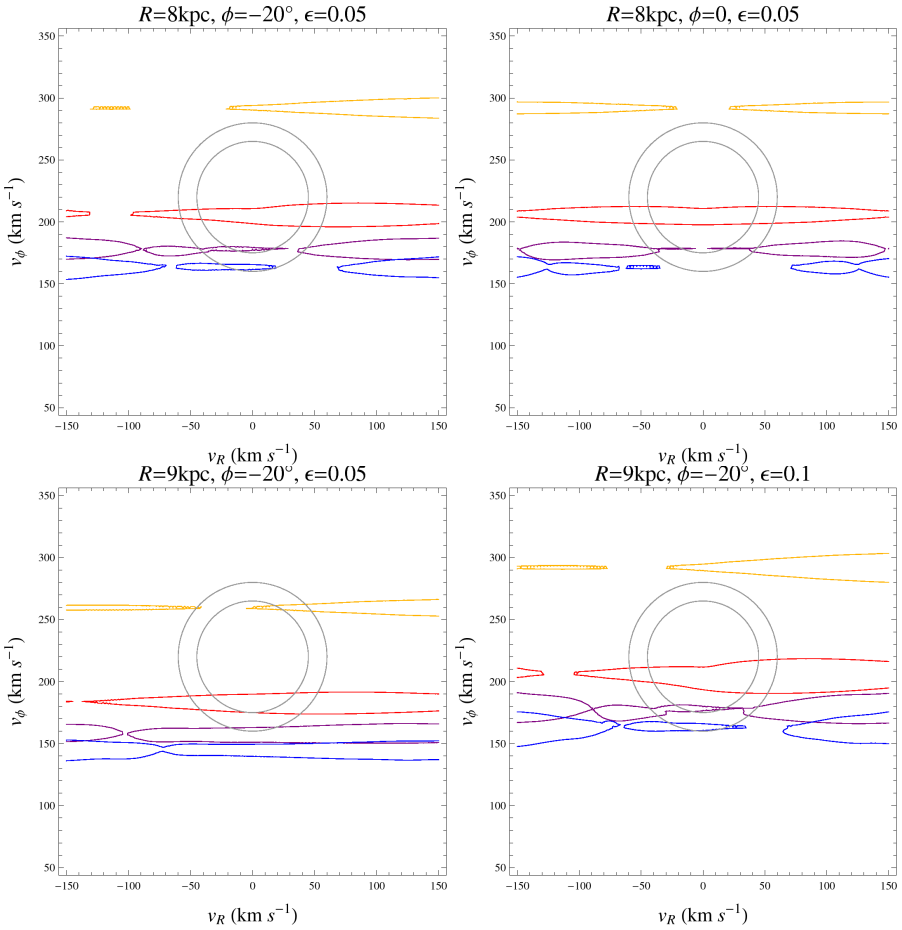


**Figure 3.2:** Predictions of the perturbation theory presented in Sect. 3.2.2 for different $(R, \phi)$ and $\epsilon$ on $v_R$ vs. $v_\phi$, for a simple Galaxy model, with $\Omega_b = 50$ km s$^{-1}$ kpc$^{-1}$. The contours enclose the regions of resonant trapping, estimated from Eqs. (3.23b)-(3.25) neglecting the terms in the sums with $|k| > 10$. The color coding is given in Table 3.1. The gray circles are centered at $(v_R, v_\phi) = (0, 220$ km s$^{-1})$ and have radius 45 and 60 km s$^{-1}$ respectively and roughly indicate the $1\sigma$ extension in velocity space of the thin and thick disks in the Solar Neighborhood.

the contours of the $(l_R, l_\phi) = (1, 2)$ (red) resonance. For $\phi = 0$ the island represents orbits trapped to the resonance and arriving at $(R, \phi) = (8 \text{ kpc}, 0)$ moving outwards ($v_R < 0$) or inwards ($v_R > 0$). At $\phi = -20°$ the islands are asymmetric. If we consider a gaussian distribution of stars to represent the thin or the thick disk (the gray circles in figure are meant to represent the $1\sigma$ contours of these disks), we see that the majority of stars crosses this point moving inwards in the Galaxy.

If instead we change $R$, and we focus on e.g., $(R, \phi) = (9 \text{ kpc}, -20°)$ (Fig. 3.2, bottom right), the regions where the orbits are trapped shift to lower $v_\phi$. Vice versa, moving inwards in $R$ would shift the contours to higher $v_\phi$. The symmetry of some resonant families with respect to $v_R$ is also changed (see especially the $(1, 3)$ and $(1, 4)$ resonances in the figure).

Finally, increasing the bar strength to $\epsilon = 0.1$ (Fig. 3.2, bottom left) we see that the contours become wider in $v_\phi$, at a fixed $v_R$. This is due to the fact that a stronger bar increases the volume of the phase-space where resonant trapping is possible.

Fig 3.2 shows that in some cases the contours overlap. In the regions where the contours overlap, the perturbation analysis performed fails to predict to which resonance the orbits are trapped. This happens because this approximation treats each resonance separately. In other words, it can happen that according to the perturbation analysis an orbit can be trapped to more than one resonance. We remind the reader that the phase-space regions of transition between different kinds of resonant trapping correspond usually with regions of chaotic orbits (a phenomenon also known as *resonance overlap*, see Binney & Tremaine 2008).

## 3.3 Fourier analysis

The perturbation theory described in Sect. 3.2, has the disadvantage that it cannot be easily extended to more complicated systems. In particular, the greatest problem is to find a general method in three dimensions, that is able to obtain for any unperturbed Hamiltonian $H_0$ action-angle coordinates $(\boldsymbol{J}, \boldsymbol{\theta})$ (see Eq. 3.1) and a scheme for perturbative calculations in the vicinity of the different types of resonances. Despite encouraging results (Kaasalainen 1994), we are still far from having an efficient and simple method.

Nonetheless, insights can be obtained from numerical experiments. In particular, Fourier analysis can provide a fast classification of orbits in a potential, to determine if they are trapped or not to resonances.

### 3.3.1 Fourier spectra

Several works in the literature treat the subject of orbital spectral analysis in great detail (e.g., Binney & Spergel 1982; Laskar 1993; Carpintero & Aguilar 1998). All methods have in common a procedure that consists in numerical integrating orbits in a potential and obtaining numerically the Fourier transform of the time series of the coordinates $\mathbf{x}_i(t_i)$. If the orbit is regular in a $N_\mathrm{d}$-dimensional space, the motion is quasi-periodic i.e.,

$$\mathbf{x}(t) = \sum_{k=1}^{\infty} \mathbf{a}_k e^{i\chi_k t}, \tag{3.30}$$

where $\mathbf{a}_k$ are the complex amplitudes and $\chi_k$ are linear combinations of the $N_\mathrm{f} \leq N_\mathrm{d}$ fundamental frequencies $\boldsymbol{\chi}$, i.e., $\chi_k = \mathbf{n}_k \cdot \boldsymbol{\chi}$. The Fourier transform of a quasi-periodic

signal like Eq. (3.30) is a sum of delta functions with amplitudes given by the coefficients $\mathbf{a}_k$. The delta functions become spikes of a certain width in the computation of the Fourier transform, as the resolution of the orbital integration $\Delta t = t_{i+1} - t_i$ is finite.

In the rest of this Chapter we consider orbits in configuration space (i.e., in 3D), described by the cylindrical coordinates $(R, \phi, z)$. First we integrate the orbits in a potential that resembles that of the Milky Way, for a time $t_\mathrm{f}$ and with resolution $\Delta t$ (see details below), to obtain the time series $\mathbf{x}_i = (R_i, \phi_i, z_i)$. Then we derive the power spectrum $P_\xi(\omega_j)$ as

$$P_\xi(\chi_j) = \sqrt{\frac{1}{N}\left[\left(\sum_{i=1}^{N} \xi_i \cos \chi_j t_i\right)^2 + \left(\sum_{i=1}^{N} \xi_i \sin \chi_j t_i\right)^2\right]}, \tag{3.31}$$

where $\xi$ is $R$ or $z$ and $N$ is the number of time intervals. From this spectrum we select the frequency $\omega_\xi$, where $P_\xi(\omega_\xi) = \max_j [P_\xi(\chi_j)]$, which is the frequency of the component of the motion with the highest amplitude. The frequency $\omega_\phi$ is instead obtained as the slope of the straight line that gives the best fit to the points $(t_i, \phi_i + 2\pi N_\phi)$, where $N_\phi$ is the number of revolutions of the particle around the center of the potential (Athanassoula 2002; Ceverino & Klypin 2007).

### 3.3.2 Frequency maps

For each orbit the Fourier analysis gives a triad of frequencies $(\omega_R, \omega_\phi, \omega_z)$. In Fig. 3.3 we show a "frequency map". Here each point corresponds to an orbit characterized by $(\omega_R/\omega_z, \omega_\phi/\omega_z)$ (Binney & Tremaine 2008). This map was obtained for thin disk particles taken from the simulations described in Chapter 2, for the GB2 potential, in a cylindrical volume centered at $(R, \phi, z) = (8\ \mathrm{kpc}, -20°, 0)$ of width 300 pc and height 600 pc, in the final output of the simulation. To compute the frequencies we used $t_\mathrm{f} = 100T$, where $T = 2\pi \times (220/8\ \mathrm{km\ s^{-1}\ kpc^{-1}})^{-1}$ (approximately one dynamical time at the Sun's position in the Galaxy).

As we see, the dots are not uniformly distributed in the map, but they often group along straight lines. The orbits on lines in a frequency map are trapped to the same resonance. The colors correspond to the different resonances as given in Table 3.1.

To explain why orbits trapped to a resonances occupy lines in the frequency map, we use as an example a horizontal resonance $\Omega_R : \Omega_\phi = n : m$ ignoring the vertical motion, and therefore restricting the problem to 2D (similar considerations can be applied to the 3D case, and to the vertical resonances). When we apply the frequency analysis to the azimuth $\phi$ of the orbit, we fit a straight line to the curve (see Sect. 3.3.1)

$$\phi'(t) \equiv \phi(t) - \Omega_\mathrm{b} t = \theta_\phi(t) - \Omega_\mathrm{b} t - f(\theta_R(t)). \tag{3.32}$$

In an axisymmetric potential the $\theta_\phi(t) - \Omega_\mathrm{b} t$ part of the curve would correspond to a straight line, with periodic wiggles superposed to it, due to the $f(\theta_R(t))$ term (this is because $\phi$ is not a canonical angle, unlike $\theta_\phi$, and so does not vary as $\Omega_\phi t$). Therefore the frequency analysis would return the slope of $\theta_\phi(t) - \Omega_\mathrm{b} t$, i.e. $\Omega_\phi - \Omega_\mathrm{b}$. However, in the non-axisymmetric case the curve $\theta_\phi(t) - \Omega_\mathrm{b} t$ in general is not a straight line. In fact, we can rewrite it as

$$\theta_\phi(t) - \Omega_\mathrm{b} t = \frac{\phi_\mathrm{s}(t)}{l_\phi} - \frac{l_R}{l_\phi}\theta_R(t). \tag{3.33}$$

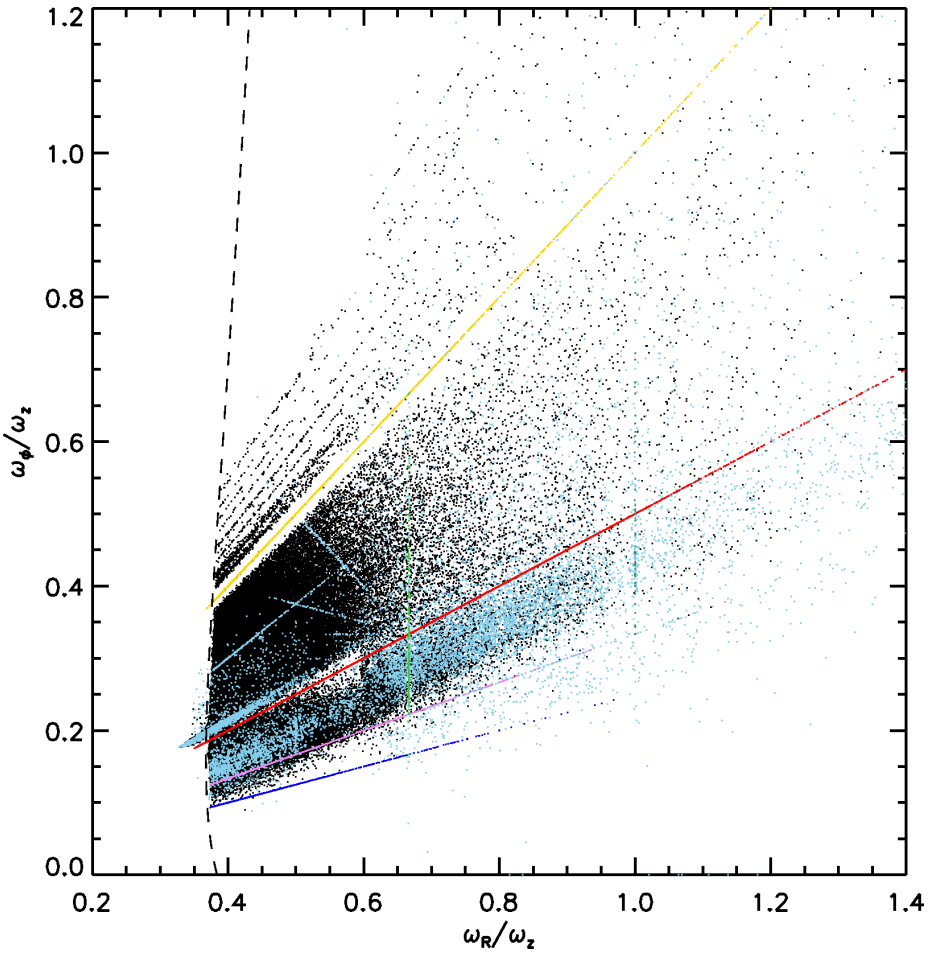


**Figure 3.3:** Frequency map for the particles inside a small cylinder of width 300 pc and height 600 pc, centered at $(R, \phi, z) = (8 \text{ kpc}, -20°, 0)$, for particles in the thin disk of the GB2 simulation presented in Chapter 2.

For an orbit trapped to a resonance $\Omega_\mathrm{s} \ll \Omega_R$, and so $\theta_\phi(t) - \Omega_\mathrm{b} t$ will also be a straight line perturbed by wiggles due to the precession of the orbit, where $\phi_\mathrm{s}(t)/l_\phi$, will librate between two values. In that case, the slope of the fitted straight line (i.e., the result of the frequency analysis) is due only to the second term in Eq. (3.33):

$$\omega_\phi = -\frac{l_R}{l_\phi}\Omega_R. \tag{3.34}$$

The $R(t)$ variable is a composition of a dominant component of the motion at a constant frequency $\Omega_R$ plus the periodic elongations due to the bar and dependent on $\phi_\mathrm{s}(t)$ (which follows from the lines of reasoning that led to Eq. (3.29)). The Fourier analysis will return the frequency of the motion with largest amplitude, i.e.,

$$\omega_R = \Omega_R. \tag{3.35}$$

Therefore the ratio

$$\frac{\omega_R}{\omega_\phi} = -\frac{l_\phi}{l_R}, \tag{3.36}$$

is a line in the frequency map. Conversely, an orbit not trapped to a resonance $\phi_\mathrm{s}$ is circulating and contributes to the fit of the curve Eq. (3.33), so that the orbits do not line up in the frequency map anymore.

For orbits with low eccentricity and vertical amplitude $(\Omega_R, \Omega_\phi, \Omega_z) \approx (\kappa, \Omega - \Omega_\mathrm{b}, \nu)$. The parametric curve $(\kappa/\nu, [\Omega - \Omega_\mathrm{b}]/\nu)\,(R_\mathrm{g})$ is shown by the dashed line in Fig. 3.3, and represents the locus of orbits that would follow exactly the epicyclic approximation (here obtained using the $m = 0$ component of the Fourier decomposition of the potential in $\phi$).

The lines in Fig. 3.3 suggest the way to identify the orbits trapped to the resonances. In what follows, we call orbits trapped to a resonance $(l_R, l_\phi, l_z)$ *regular* orbits with $|l_R\omega_R + l_\phi\omega_\phi + l_z\omega_z| < 0.001$. Notice that often the resonant orbits are defined as the ratio of frequencies, e.g., for $(l_R, l_\phi, l_z) = (1, 2, 0)$, $\omega_\phi/\omega_R = -l_R/l_\phi$.

### 3.3.3 Diffusion coefficients

Not all orbits in the potential considered will be regular (i.e., have sufficient integrals of motion to be restricted to a 3D torus in the phase-space). To characterize the regularity of an orbit (i.e., if an orbit can be written as Eq. (3.30), see also Binney & Tremaine 2008; Fux 2001) we define the diffusion coefficients. These are estimated as $d = |(\omega_1 - \omega_2)/\omega_1|$, where $\omega_1$ and $\omega_2$ are the frequency estimates derived in two intervals: for $t \in [0, 100T]$ and for $t \in [100T, 200T]$ respectively. The larger $d$, the more irregular is the orbit. We fix the threshold between regular and irregular orbits at $d_\mathrm{max} = 10^{-3}$ (Vasiliev & Athanassoula 2012). The fraction and distribution of irregular orbits is not very dependent on the exact value of this threshold: for $d_\mathrm{max} = 10^{-2}$ the fraction of irregular orbits decreases by less than $\sim 2\%$, while for $d_\mathrm{max} = 10^{-4}$ this fraction increases by $\sim 6\%$. In what follows, except for the computation of $d$, we use the frequencies obtained in the interval $t \in [0, 100T]$.

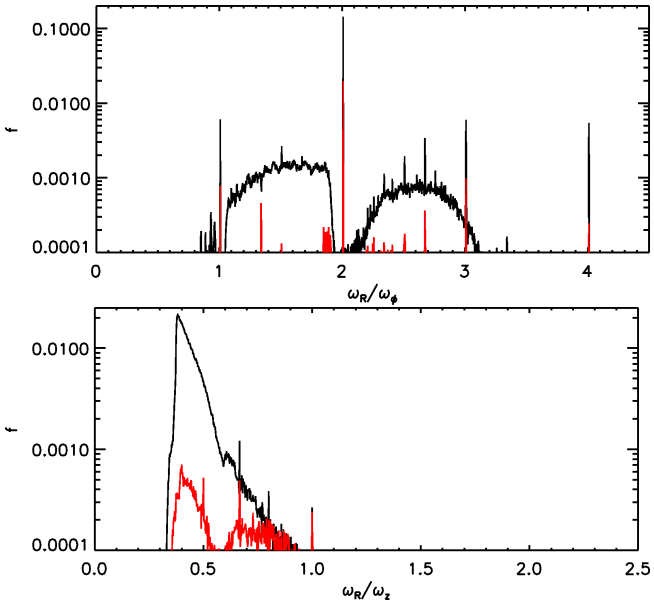


**Figure 3.4:** Distributions in the frequency ratios $\omega_R/\omega_\phi$ (top) and $\omega_R/\omega_z$ (bottom) for the same volume of Fig. 3.3 for thin disk particles in our default bar simulation. In black we plot the regular orbits, in red those that are irregular.

## 3.4 Results

### 3.4.1 Distribution of frequencies

In Fig. 3.4 we show the fraction of particles (relative to the total number of particles in the volume) from the thin disk of the GB2 simulation (corresponding to our default bar model) of Chapter 2, as a function of $\omega_R/\omega_\phi$ (top) and $\omega_R/\omega_z$ (bottom). The volume is a cylinder of width 300 pc and 600 pc height centered at $(R, \phi, z) = (8 \text{ kpc}, -20°, 0)$. This figure helps us to quantify the amount of resonant trapping in this potential and for this distribution of particles. We see that there are thin spikes present in the distributions, which correspond to the lines in Fig. 3.3. The most populated resonance is by far $(1, 2, 0)$, for almost $\sim 15\%$ of orbits are trapped to this resonance, followed by some much smaller spikes, e.g., $(1, 1, 0)$, $(1, 3, 0)$, $(1, 4, 0)$. The $R - z$ vertical resonances are very weakly populated, with only the $(3, 0, 2)$ resonance trapping $\sim 0.1\%$ of the orbits. The red curves in Fig. 3.4 represent the distribution of irregular orbits in the same volume. There is a peak of irregular orbits in the vicinity of $(1, 0, 2)$, $(1, 0, 1)$ and all the other resonances are populated by regular orbits. We can relate this to the fact that irregular orbits live in the surroundings of resonances.

In Fig. 3.5 we plot the distribution of frequencies but now for the thick disk. In this case the fraction of trapped orbits associated to horizontal resonances is slightly larger (especially for the $(1, 1, 0)$ resonance), and much larger in the vertical resonances

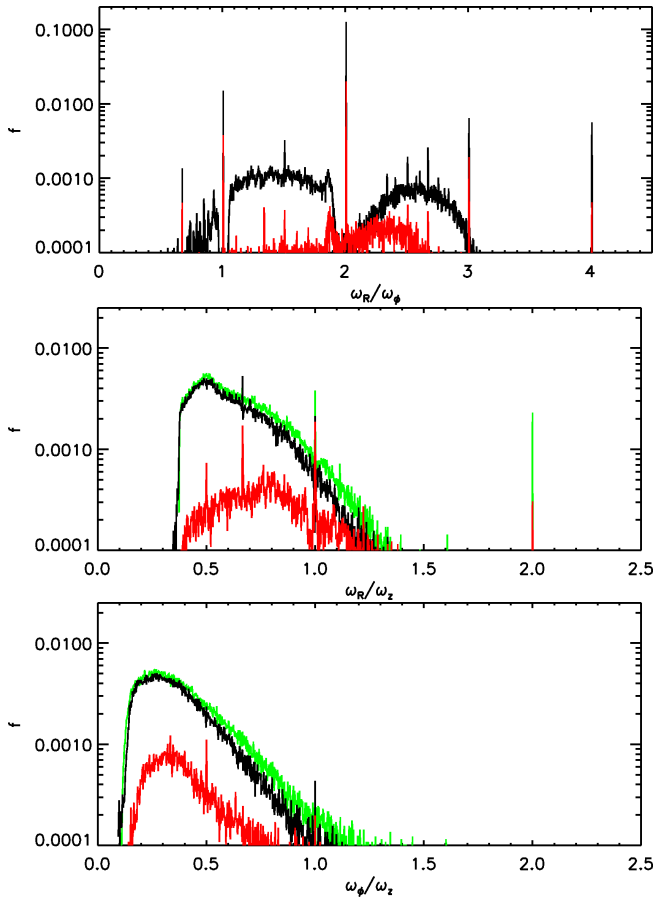


**Figure 3.5:** As in Fig. 3.4, but for the thick disk. We also include the distribution of the frequency ratios $\omega_\phi/\omega_z$ (bottom plot). The green line represents the frequencies for orbits computed in the axisymmetric potential A0+B2 (see Chapter 2).

**Table 3.2:** Fraction of orbits trapped to the main resonances inside a cylinder of width 300 pc and height 600 pc, centered at $(R, \phi, z) = (8 \text{ kpc}, -20°, 0)$, for thin and thick disk in the GB2 simulations from Chapter 2.

| $(l_R, l_\phi, l_z)$ | Thin disk | Thick disk |
|---|---|---|
| $(1, 1, 0)$ | 0.6% | 1.5% |
| $(1, 2, 0)$ | 14.2% | 12.5% |
| $(1, 3, 0)$ | 0.6% | 0.6% |
| $(1, 4, 0)$ | 0.5% | 0.6% |
| $(3, 0, 2)$ | 0.1% | 0.5% |
| $(1, 0, 1)$ | 0 | 0.2% |
| $(1, 0, 2)$ | 0 | 0.1% |
| Trapped | 16% | 16% |
| Irregular | 6.4% | 16.4% |

($(3, 0, 2)$, $(1, 0, 1)$, $(1, 0, 2)$). Also the fraction of irregular orbits is larger. For comparison we have also computed the fraction of orbits trapped to vertical resonances, for the axisymmetric potential used in the simulations of Chapter 2 before the growth of the bar using as initial conditions the positions and velocities of the particles in the thick disk of the GB2 simulations at the final time[2]. Interestingly, the green curve shows how trapping to the $R - z$ vertical resonances is already present in the axisymmetric part of potential[3] and is therefore not induced by the bar. Therefore, the only vertical frequencies genuinely related to the bar are those between the $\phi - z$ coordinates (or between $R - \phi - z$), that are represented in the bottom plot of Fig. 3.5. Some of the $\phi - z$ are present (e.g., $(0, 1, 1)$), however the fraction of orbits trapped to these resonances is negligible ($< 0.1\%$). Table 3.2 summarizes the fraction of trapped and irregular orbits in this volume both for the thin and the thick disks.

### 3.4.2 Frequencies and velocity distributions

In Fig. 3.6 we show the $(v_R, v_\phi)$ velocity distribution of the particles in the same volume considered in the previous Section (left panel: thin disk, right panel: thick disk). The color coding corresponds to the trapping to the main resonances as given in Table 3.1.

The left panel of Fig. 3.6 shows that the orbits trapped to $(1, 2, 0)$ are localized in $v_R$ vs. $v_\phi$, and that they define a horn-like feature. This horn-like feature of the $v_R$ vs. $v_\phi$ distributions was already described in Chapter 2 and is present also in the simulations of e.g., Dehnen (2000) and Fux (2001). The location of this feature corresponds well to the $(1, 2)$ resonance computed using the perturbation analysis of Sect. 3.2.2, as shown in top left panel of Fig. 3.2. It seems, therefore, that the expectations of the perturbation theory are also valid for these 3D simulations, although of course the details are different.

[2] We obtain similar results performing the analysis for particles in the axisymmetric initial conditions for the same volumes.

[3] In fact, resonant trapping and irregular orbits can exist also in realistic galactic axisymmetric potentials, even though such orbits occupy a small region of the phase-space (Henon & Heiles 1964).

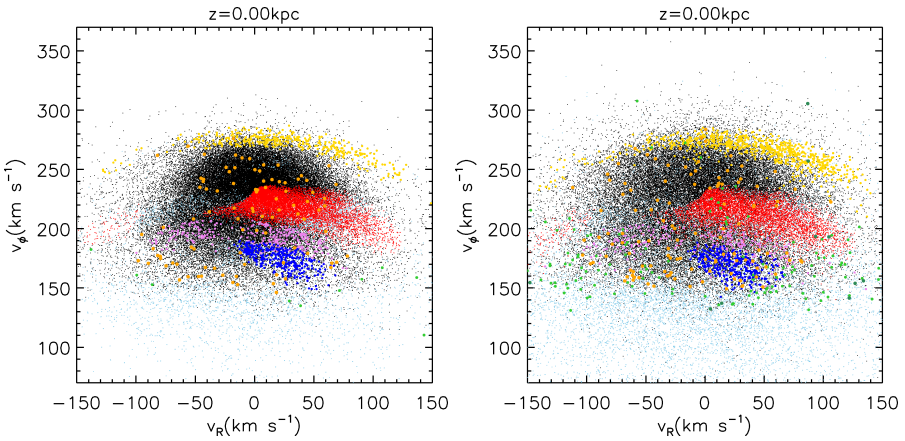


**Figure 3.6:** $v_R$ vs. $v_\phi$ distributions of a random subsample of 50000 particles from the same volume as in Fig. 3.3, color coded with the orbits trapped to the resonances, for thin (left) and thick disk (right) particles.

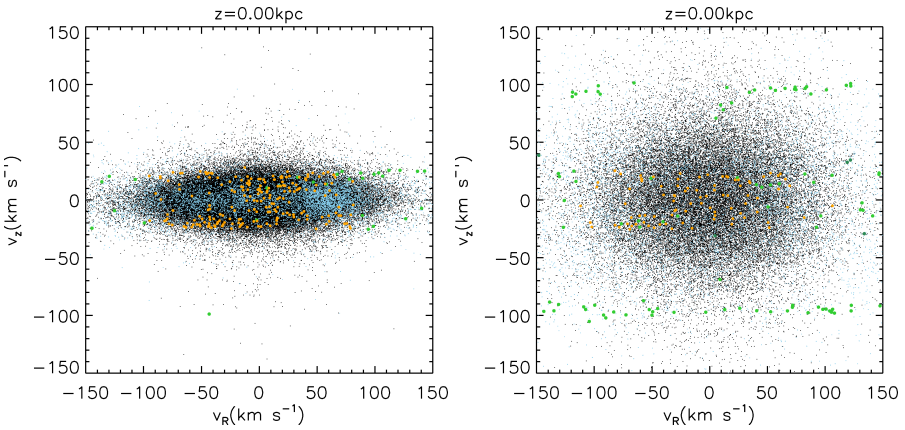


**Figure 3.7:** $v_R$ vs. $v_z$ distributions of a random subsample of 50000 particles from the same volume as in Fig. 3.3, color coded with the orbits trapped to the resonances, for thin (left) and thick disk (right) particles. In this case we only show the two most populated vertical resonances: the dark green points correspond to $(1, 0, 1)$ and the orange points to $(1, 0, 2)$.

As in Fig. 3.2, we notice that for $v_R < 0$ there is almost complete depletion of $(1, 2, 0)$ orbits. The orbits trapped to $(1, 1, 0)$ and $(1, 3, 0)$ are localized both at positive and negative $v_R$ as also seen in Fig. 3.2. Only $(1, 4, 0)$ seems to be distributed differently in our simulations as it is only found for $v_R > 0$ while in Fig. 3.2 it can be seen both in $v_R > 0$ and $v_R < 0$.

The right panel of Fig. 3.6 shows that the distribution in the $v_R$ vs. $v_\phi$ space for particles in the thick disk associated to trapped orbits is similar. The only difference is that all the resonances are more populated, especially those in the tails of the velocity distribution, such as $(1, 1, 0)$.

Both for the thin and thick disks the irregular orbits are distributed in wide regions, but they are mostly concentrated near to trapped orbits. This is especially clear in the valley formed by the $(1, 2, 0)$ resonance at $v_\phi \sim 200$ km s$^{-1}$ (see Chapter 2). This is expected, as irregular orbits occupy in phase-space the gaps between regions of resonant trapping, as commonly observed using Surfaces of Section methods (Binney & Tremaine 2008).

Finally, in Fig. 3.7 we plot the $v_R$ vs. $v_z$ distribution. This time, however, we highlight only the orbits trapped to the vertical resonances, as the horizontal resonances are evenly distributed in $v_z$. We see how the stars on orbits trapped to $(1, 0, 1)$ (green dots) tend to be distributed at high $|v_z|$, both for the thin and the thick disk. The density of this kind of orbits is in fact larger farther away from the disk plane (see below), and so only orbits with large $v_z$ reach these heights. However, in small volumes centered at $z = 0$, the fraction of orbits trapped to the vertical resonances is almost negligible. Also apparent from Fig. 3.7 is that the $v_z$ distribution is smooth and so the resonant orbits do not lead to the appearance of features in the vertical velocity distribution.

### 3.4.3 Distribution of guiding centers

In Fig. 3.8 we have plotted the $v_R$ vs. $v_\phi$ velocity distribution for thin disk particles in a volume centered at $(R, \phi, z) = (8 \text{ kpc}, -20°, 0)$ from the GB2 simulation of Chapter 2, color coded by the location of their guiding center radius. The red points have $R_\text{g} < R_\text{OLR}$, the blue points have $R_\text{g} > R_\text{OLR}$. Our proxy for $R_\text{g}$ is the average $R$ of the orbits computed over the same time interval used to derive the frequencies.

This plot shows that the guiding centers of the orbits almost perfectly trace the bimodality in the velocity distribution induced by the bar. The OLR Mode (see Chapter 2) is composed by particles with $R_\text{g} < R_\text{OLR}$, i.e., stretched perpendicular to the bar and the LSR Mode by orbits with $R_\text{g} > R_\text{OLR}$, stretched parallel to the bar, as shown in the top panels of Fig. 3.1.

The orbits with $R_\text{g} < R_\text{OLR}$ have a net outward motion and those with $R_\text{g} > R_\text{OLR}$ an inward motion, from which the bimodality in the velocity distribution results, as in Kalnajs (1991) hypothesis. The analysis of the thick disk particles in the same volume leads to similar conclusions.

### 3.4.4 Trends as a function of $z$

In Fig. 3.9 we show the fraction of orbits trapped to the different resonances as a function of $z$, inside a cylinder of width 300 pc and height 4 kpc, centered at $(R, \phi, z) = (8 \text{ kpc}, -20°, 0)$, for the thin (top panel) and thick disk (bottom panel). From these

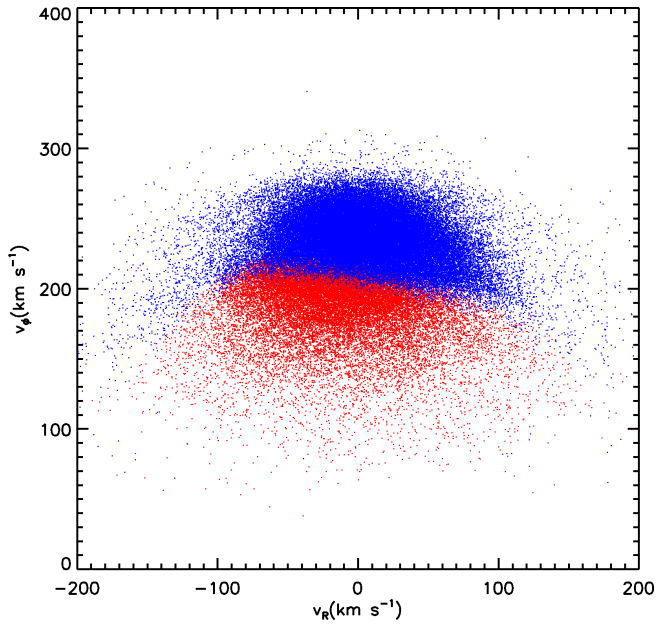


**Figure 3.8:** Velocity distribution of the particles inside a cylinder of width 300 pc and height 600 pc, centered at $(R, \phi, z) = (8 \text{ kpc}, -20°, 0)$, for the thin disk simulation GB2, from Chapter 2. Here the red dots have guiding center radii $R_g < R_{OLR}$, while the blue dots have $R_g > R_{OLR}$.

figures we see that the fraction of orbits trapped to horizontal $R-\phi$ resonances is almost constant with distance from the disk plane in the wide range of $z$ considered ($|z| < 2$ kpc), both for the thin and thick disk. Therefore the *amount* of horizontal trapping seems to be independent on $z$. This is in agreement with the results of Chapter 2, where we noticed that the total effect of the bar on the horizontal velocity distribution induced by the bar to be nearly independent of $z$. The fraction of orbits trapped to vertical resonances instead increases with $z$ (orange, green and gray line) for all the vertical resonances that we considered. However, the fraction of particles trapped to those resonances genuinely induced by the bar (e.g., $(0, 1, 1)$, gray line) always remains very moderate in magnitude. The resonance that seems to be most populated is $(1, 0, 1)$ (green line) for the thick disk. In particular at $\sim 2.5$ kpc (outside of the axes range of the plot) the amount of particles trapped to this resonance is non-negligible ($\sim 8\%$). However there is no clear sign of a kinematical effect of this resonance on the velocity distribution for thick disk particles at these heights. The fraction of irregular orbits also slightly increases with $z$, as the vertical resonances become more populated.

In Figs. 3.10 and 3.11 we study how the characteristic parameters of the velocity distribution of the particles associated to the various resonant families changes with height from the Galactic plane. These figures plot the average of each of the three velocity components for particles inside the same bins as in Fig. 3.9. We see how the

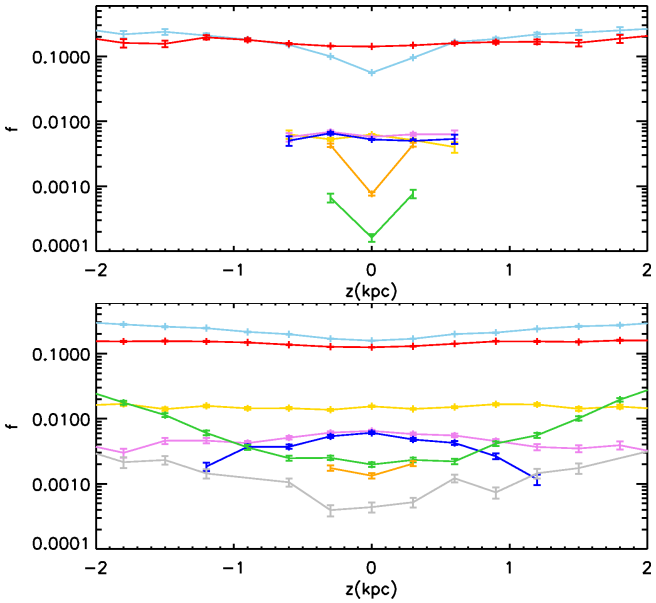


**Figure 3.9:** Fraction of trapped orbits as a function of the distance from the disk plane $z$, for particles in the GB2 simulation, inside a cylinder of width 300 pc centered at $(R, \phi, z) = (8 \text{ kpc}, -20°, 0)$ and height 4 kpc. These curves are made using independent vertical bins of size 300 pc. The error bars on the averages are due to the Poisson noise associated to the finite number of particles. Top: thin disk. Bottom: thick disk.

average $v_R$ and $v_z$ reflects what we saw in Sect. 3.4.2, namely that $\langle v_z \rangle = 0$ and $\langle v_R \rangle \neq 0$ for the different horizontal resonant families for $z = 0$, and how this behavior remains almost unchanged with $z$. The only exception seems to be a tendency for the orbits trapped to the $(1, 2, 0)$ and especially $(1, 1, 0)$ to have positive $v_z$ for $z < 0$ and negative $v_z$ for $z > 0$. The rotational velocity $v_\phi$ of the trapped orbits is instead clearly decreasing as $|z|$ increases. In fact, the $v_\phi$ position of the resonances varies following the change with $z$ of the axisymmetric part of the potential $\Phi_0(R, z)$, while the potential of the bar is almost constant with $z$. Notice that a related manifestation is that $\langle v_\phi \rangle$ of the whole distribution (black lines) decreases with $|z|$ as expected from the asymmetric drift relation (Binney & Tremaine 2008).

### 3.4.5 Trends as a function of $\phi$

In Fig. 3.12 we show the trend in the fraction of trapped orbits and in their average velocity as a function of the angle from the long axis of the bar $\phi$, for orbits in the thin disk of the GB2 simulation, in an annulus of 600 pc width and 600 pc height, centered at $R = 8$ kpc and $z = 0$. From this figure we see that the fraction of orbits trapped to the resonances is a periodic function $\phi$, and the same is true for the average horizontal velocity $v_R$ and $v_\phi$ components. Notice how the periodicity depends on the geometry of

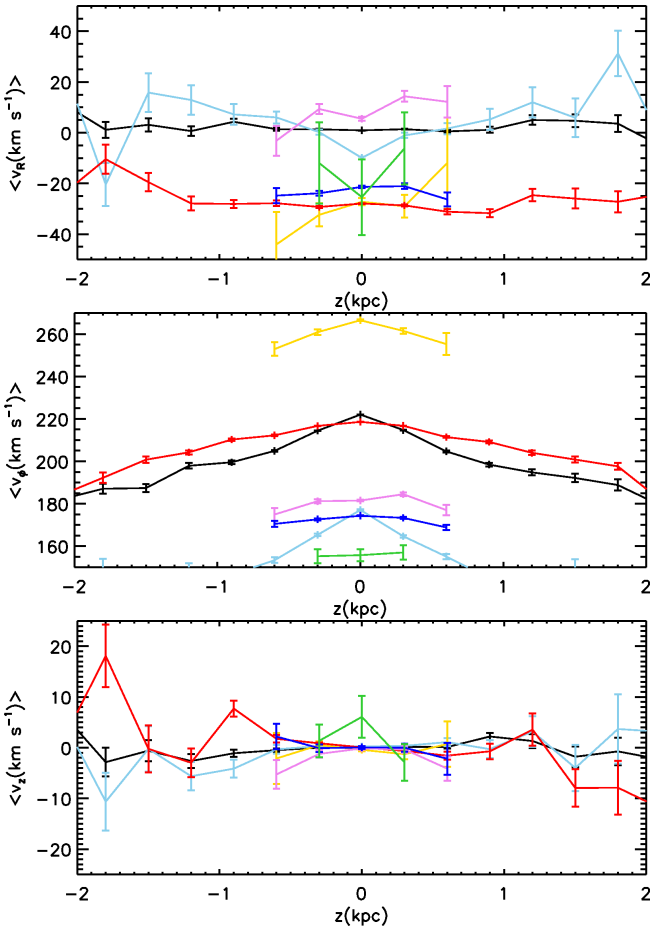


**Figure 3.10:** Average velocities inside independent vertical bins of size 300 pc for the thin disk in GB2. The different colors correspond to orbits trapped to different resonances (e.g., $(1, 2, 0)$, red line), the irregular orbits (light blue line) and all the particles (black line). The detailed color scheme is given in Table 3.1.

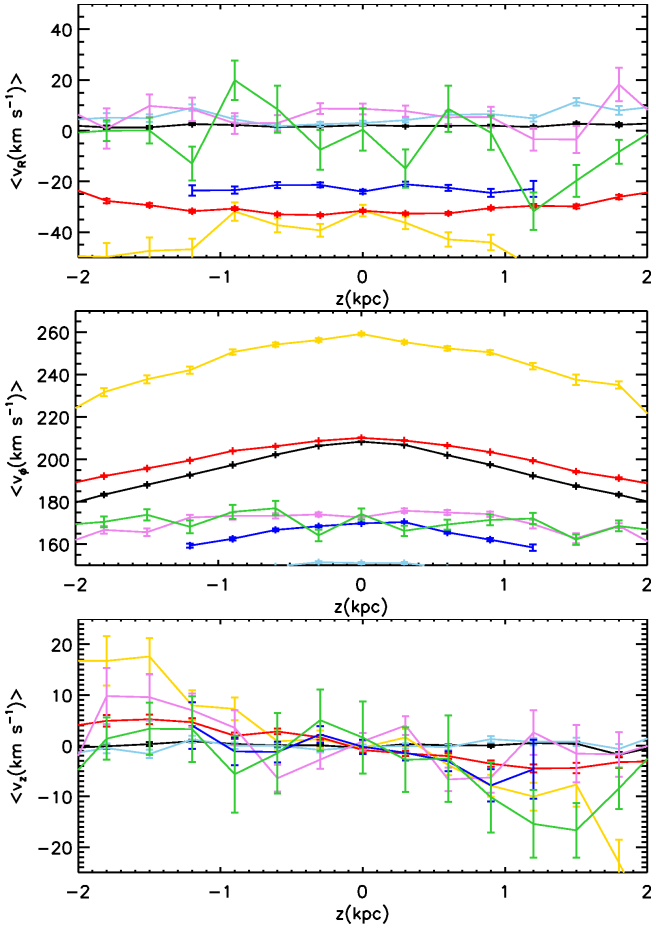


**Figure 3.11:** As in Fig. 3.10, but for the thick disk.

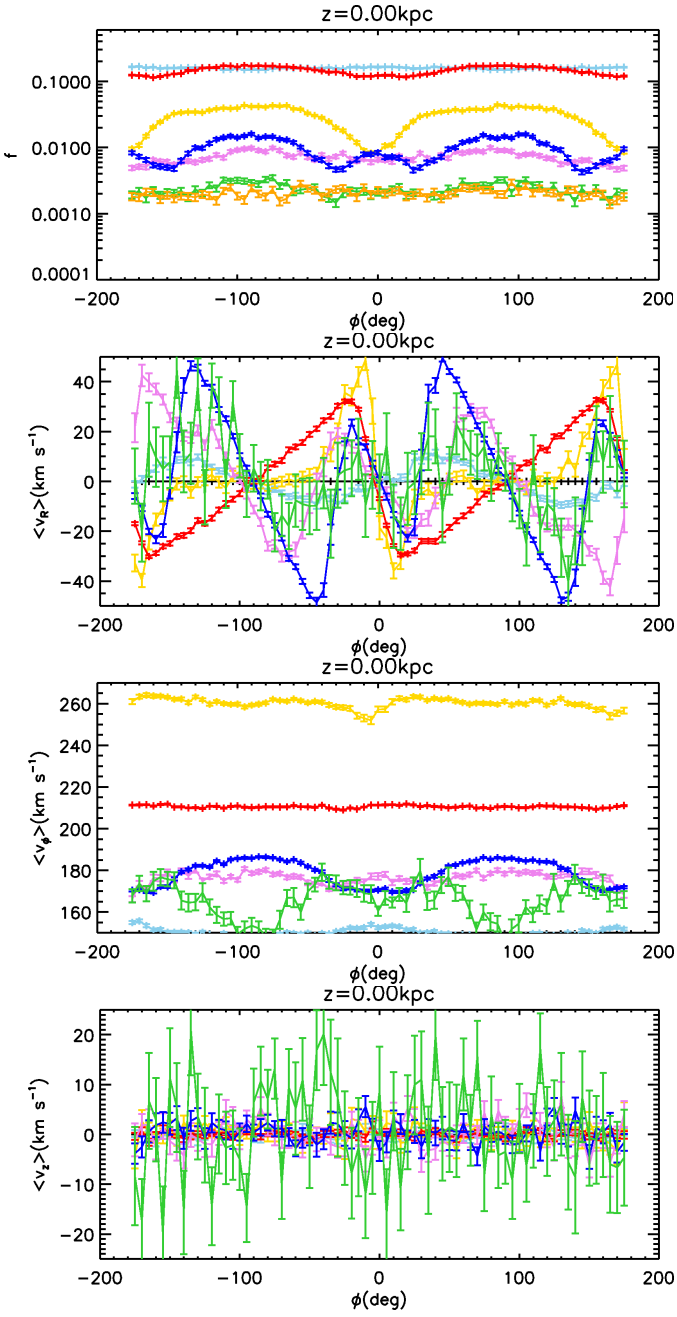


**Figure 3.12:** Fraction of trapped orbits and average velocities as a function of $\phi$, for thin disk particles in the GB2 simulation, inside a ring of 600 pc radial extent and height 600 pc, centered at $R = 8$ kpc and $z = 0$. The error bars represent the Poisson noise. Only those bins with more than 25 particles are shown.

the type of orbits considered. For example, it is very clear that the $\langle v_R \rangle$ of the $(1,2,0)$ orbits oscillates twice in the $\phi$ range $[-180°, 180,°]$, while the $\langle v_R \rangle$ of $(1,4,0)$ oscillates four times. Moreover, the amplitude of the oscillation changes with $\phi$ because the bar stretches the same orbits parallel and perpendicular to its long axis[4]. These results seem to agree with the predictions from the perturbation theory in 2D, that show that the angle $\phi$ mostly influences the $v_R$ position of the orbits trapped to the resonances, with different periodicity depending on the different resonances. It is also interesting to notice how the orbits trapped to the vertical resonance $(1,0,1)$ have oscillations in the horizontal velocities, and that $\langle v_z \rangle$ does not depend at all on $\phi$.

The behavior with $\phi$ of the trapped orbits of the thick disk, both on and far from the plane, is qualitatively similar to what was just discussed for the thin disk.

### 3.4.6 Trends as a function of $R$

In Fig. 3.13 we plot the average velocity of the various resonant families as well as their fraction as function of distance $R$ from the Galactic center for $R \in [6.5, 9.5]$ kpc. Here we consider the GB2 simulation for volumes centered at $\phi = -20°$, $z = 0$. The trends in the thick disk are very similar. The velocity trends that we find are consistent with the expectations from the perturbation analysis. In particular the $\langle v_\phi \rangle$ of the horizontal resonances always decreases going outwards in the Galaxy. Inside (outside) the Outer Lindblad Resonance, at $R = 7.69$ kpc, $\langle v_R \rangle$ of the $(1,2,0)$ orbits is decreasing (increasing). At the same time $\langle v_z \rangle \sim 0$ for all the cases we consider. The fraction of trapped orbits increases or decreases with $R$ as we are approaching (e.g., for $(1,1,0)$, $(1,2,0)$) or leaving the position of a resonance in the Galaxy (as in the case of $(1,3,0)$, $(1,4,0)$). Interestingly, the peak of orbits trapped to $(1,2,0)$ does not occur precisely at the Outer Lindblad Resonance, but rather at $R \sim 8.5$ kpc.

### 3.4.7 Other bar models

In this section we present the results of the frequency analysis for two other bar models. We select the GB1 and LB2 bar models from Chapter 2. The GB1 model corresponds to the less massive bar and has the same geometry of the GB2 model discussed so far. The LB2 has the same mass but a different geometry from GB2 (see Chapter 2 for more details).

We focus here on the fraction of orbits trapped to the resonances for these models, as we expect to see the most interesting differences or similarities for this quantity.

In Fig. 3.14 (top) we show the fraction of orbits trapped to the resonances for the GB1 model, for a cylindrical volume of width 300 pc centered at $(R, \phi) = (8 \text{ kpc}, -20°, 0)$, in the thick disk case. In this case we plot all bins containing at least 4 particles. This plot should be compared to the bottom panel of Fig. 3.9 for GB2.

The main difference is that the fraction of orbits trapped to the resonances or irregular orbits is lower in GB1 than in GB2. For example, the fraction of orbits trapped to $(1,2,0)$ is 9% and the fraction of irregular orbits is 12% in the bin centered at $z = 0$, compared to 12% and 16% for GB2. This is a consequence of the fact that the bar mass in GB1 is smaller (by a factor of 2) and therefore the perturbation on the axisymmetric part of the

[4] A second reason for some of the variation with $\phi$ is that the simulation is not completely phase-mixed (see Sect. 2.3.2 of Chapter 2).

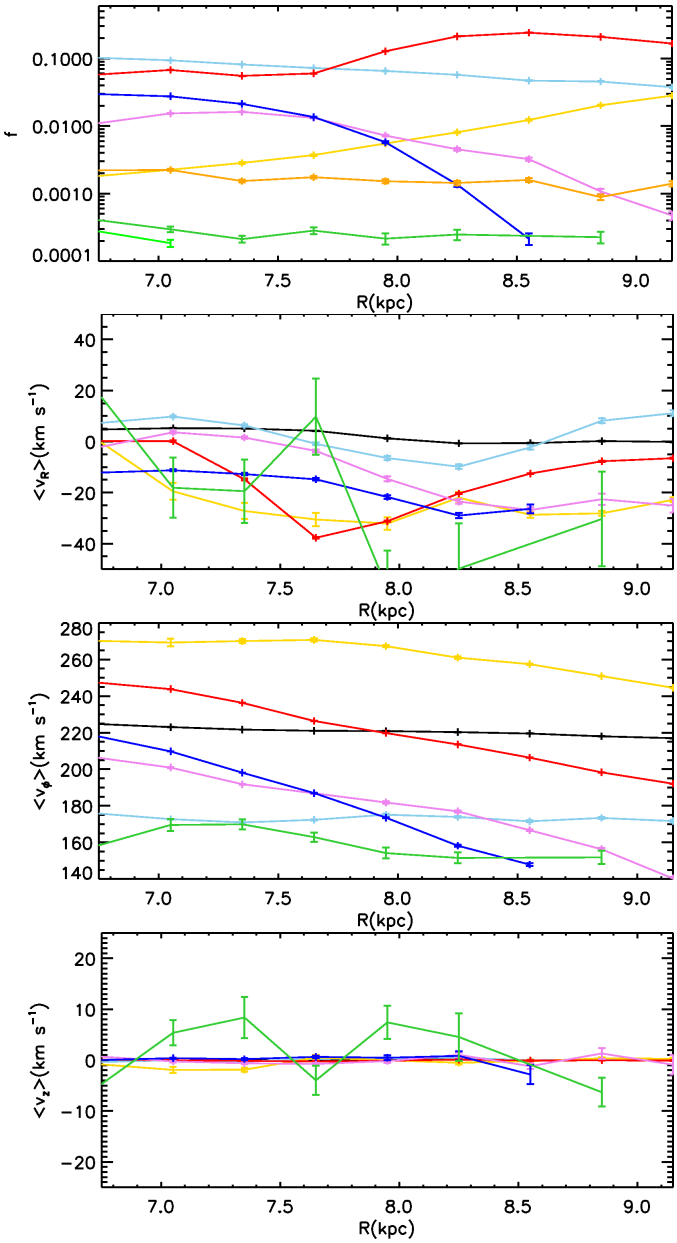


**Figure 3.13:** Fraction of trapped orbits and average velocities as a function of $R$, for particles of the thin disk in the GB2 simulation, inside volumes aligned at $\phi = -20°$ and $z = 0$. The errors bars represent the Poisson noise. Only those bins with more than 25 particles are shown.

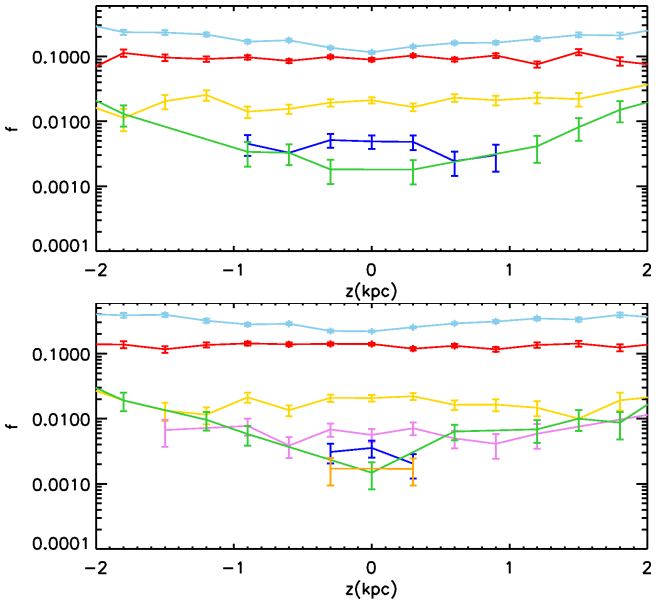


**Figure 3.14:** As in Fig. 3.9, for the GB1 model (top) and LB2 (bottom), for the thick disk. The error bars represent the Poisson noise of the fraction. In this case only those bins where the fraction is twice as big as the error are shown.

potential is also lower, which results in a smaller fraction of the phase-space occupied by resonant trapping or irregular orbits, as we saw also in the perturbation analysis of Sect. 3.2, and specifically in Fig. 3.2.

Note that as in the GB2 case, the fraction of trapped orbits remain constant with $z$ for the horizontal resonances and increases with $z$ for the vertical resonances (in green and orange).

The LB2 case is shown in the bottom panel of Fig. 3.14. Even if in this case the only difference from GB2 is the geometry of the bar, as we have explained in Chapter 2 the net effect in the Solar Neighborhood is a larger perturbation to the axisymmetric part of the potential.

As a consequence, the fraction of orbits trapped to the resonances is larger in LB2, with 14% of orbits trapped to $(1, 2, 0)$ and 22% of irregular orbits. As before the fraction of orbits trapped to horizontal resonances, stays constant with $z$, like all the other bar models that we explored here, despite the fact that the LB2 bar is flatter that in GB2.

## 3.5 Summary and conclusions

We have studied the dynamical characteristics of disk stars in a galactic potential resembling that of the Milky Way, and which includes a bar, halo and thin and thick disks. Our interest is in the effects of the bar on the kinematics of stars, in particular

close to the Sun, but also as function of location across the disk (i.e., distance from the Galactic center and angle from the major axis of the bar). To this end, we have used the simulations presented in Chapter 2, and shifted our focus to the characterization of the resonances induced by the bar and their relation to the kinematical features found earlier in this Thesis.

In the case of the Milky Way, as well as in our simulations, the bar can be seen as a perturbation on a background axisymmetric potential. This has allowed us to model the dynamics of stars using a perturbation analysis in 2D along the lines of Weinberg (1994). In this way we have identified orbital families that are trapped to resonances. We have then established how these trapped orbits map onto velocity space, especially for stars in the vicinity of the Sun, and found that they define "islands" in $(v_R, v_\phi)$ velocity space. Furthermore, we have shown that the $\langle v_R \rangle$ velocity of the trapped orbits depends on the angle from the bar and the $\langle v_\phi \rangle$ velocity depends on the distance from the center of the Galaxy and the type of resonance. Moreover, the stronger the bar force, the larger the regions of resonant trapping in the velocity space.

Since the simulations presented in Chapter 2 are 3D, the gravitational potential is somewhat more complex, and the stars follow specific distributions (both spatially and kinematically), we have performed a Fourier frequency analysis to study the resonant trapping present in those simulations. This analysis shows that an important fraction of the orbits ($\sim 16\%$) is trapped to the resonances in a solar neighborhood volume. The most populated resonance is the $(1, 2, 0)$ ($\Omega_R : \Omega_\phi = 2 : 1$), with $\sim 14\%$ trapped and defining a distinct feature in the velocity distribution. The remaining resonances are less populated, and $\sim 6\%$ of the stars in this volume are on irregular orbits.

Interestingly, we have found that the fraction of orbits trapped to horizontal resonances ($\Omega_R : \Omega_\phi$) does not depend on distance from the disk plane $z$. This is consistent with the analysis of the $(v_R, v_\phi)$ velocity distribution as function of height $z$, where characteristic features, which we can now directly associate to orbital trapping, are present at all heights explored.

On the other hand, the fraction of orbits trapped to the vertical resonances does increase with $z$. However, the vertical resonances do not influence significantly the velocity distribution, as they do not define specific features in velocity space.

More generally, we have also found that the fraction of trapped orbits and their location in velocity space varies mostly with $R$ and $\phi$ position in the Galaxy, while the effect of $z$ is mostly to shift $\langle v_\phi \rangle$ of the trapped orbits.

Finally we have also explored two other bar models (a bar with half of the mass than the default bar discussed in the rest of the Chapter but with the same geometry, and a bar with different geometry but the same mass). The main difference between the models lies in the number of trapped and irregular orbits, that depends on the strength of the perturbation. In particular, for our less massive bar model these fractions are smaller and for our long bar model are larger than in our default model.

## Acknowledgements

We would like to thank E. Vasiliev for useful discussions. The authors gratefully acknowledge support from the European Research Council under ERC Starting Grant GALACTICA-240271.

Chapter 4

# The bar and the large scale velocity gradients in the Galactic disk

Based on Monari, Helmi, Antoja & Steinmetz (2014).
Accepted for publication in A&A, arXiv:1402.4479.

## Abstract

We investigate whether the cylindrical (galactocentric) radial velocity gradient of $\sim -3$ km s$^{-1}$ kpc$^{-1}$, directed radially from the Galactic center and recently observed in the stars of the Solar Neighborhood with the *RAVE* survey, can be explained by the resonant effects of the bar near the Solar Neighborhood.

We compared the results of test particle simulations of the Milky Way with a potential that includes a rotating bar with observations from the *RAVE* survey. To this end we applied the *RAVE* selection function to the simulations and convolved these with the characteristic *RAVE* errors. We explored different "solar neighborhoods" in the simulations, as well as different bar models.

We find that the bar induces a negative radial velocity gradient at every height from the Galactic plane, outside the Outer Lindblad Resonance and for angles from the long axis of the bar compatible with the current estimates. The selection function and errors do not wash away the gradient, but often make it steeper, especially near the Galactic plane, because this is where the *RAVE* survey is less radially extended. No gradient in the vertical velocity is present in our simulations, from which we may conclude that this cannot be induced by the bar.

## 4.1 Introduction

Many of the past efforts in modeling the mass distribution of the Milky Way have assumed that the Galaxy is axisymmetric and in a steady state. However, there is a wealth of evidence that these assumptions are not really valid. The two most important deviations from axisymmetry are the spiral arms and the bar. These features are not only apparent as non-axisymmetric density enhancements, but they also have long-range gravitational effects. In particular, the bar modifies the kinematics of the outer parts of the Galactic disks, far beyond its extension, through resonant interactions.

That the velocity distribution of stars very near to the Sun is not smooth (as one would expect in a steady state axisymmetric system), but instead rich in substructures, has been established observationally thanks to data from the *Hipparcos* satellite and other surveys (Dehnen 1998; Famaey et al. 2005; Antoja et al. 2008). Several authors have explained these substructures as being due to orbital resonant effects of the bar (Dehnen 2000; Fux 2001), of the spiral arms (Mayor 1970; De Simone et al. 2004; Antoja et al. 2011), or both (Antoja et al. 2009; Quillen et al. 2011).

Using data from the *RAVE* survey (Steinmetz et al. 2006), Antoja et al. (2012) discovered that some of the kinematic substructures detected in the vicinity of the Sun can be traced further, both on and above the plane of the Galaxy, up to $\sim 0.7$ kpc.

But *RAVE* also made it possible to discover large scale stellar streaming motions. Siebert et al. (2011a) (in the rest of the Chapter S11) used a sample of $213,713$ stars to discover a gradient in the mean galactocentric radial velocity that decreases outward with Galactic radius. S11 show that this gradient was also present when using only the $29,623$ Red Clump stars in their sample, whose distances are more accurate. Siebert et al. (2012) modeled the gradient as caused by a long-lived spiral pattern[1]. Williams et al. (2013) (hereafter W13) studied the 3D velocity distribution of Red Clump stars in *RAVE* in detail, confirmed the existence of the radial velocity gradient and also discovered a more complicated vertical velocity distribution than expected, attributing it to secular phenomena in the Galaxy. Faure et al. (2014) generalized to 3D the model for the spiral arms presented in Siebert et al. (2012), which now also depends on the distance from the Galactic plane. This model nicely predicts a behavior for the mean vertical velocity that is similar to what is observed in W13 (i.e., resembling "rarefaction-compression" waves), together with the radial velocity gradient.

On the other hand, Monari et al. (2013) (hereafter M13), used 3D test particle simulations to show that the gravitational effects of the bar can significantly affect the kinematics of stars near the Sun, even at distances from the Galactic plane up to at least $z \sim 1$ kpc for the thin disk and $z \sim 2$ kpc for the thick disk. These results imply that some of the substructures found in Antoja et al. (2012) could also be caused by the bar.

In this Chapter we investigate an alternative explanation for the observed radial velocity gradient, beyond that caused by the spiral arms, by suggesting that it can be created by the bar. To do so, we compare the results of the test particle simulations in M13 with the *RAVE* data.

The Chapter is organized as follows. In Sect. 4.2 we summarize the salient characteristics of the simulations from M13, and in Sect. 4.3 we describe how we apply the *RAVE* selection function and error convolution to them, to mimic a *RAVE* catalog. In Sect. 4.4

[1] Considering the effect on the Solar Neighborhood of a slowly rotating bar, triaxial spheroid or dark matter halo, Blitz & Spergel (1991) also predicted radial motions in the gas kinematics.

**Table 4.1:** Parameters of the bar and location of the main resonances.

| Parameter | Default Bar | Long Bar | Less Massive Bar |
|---|---|---|---|
| $M_{\rm bar}(M_\odot)$ | $2\times10^{10}$ | $2\times10^{10}$ | $10^{10}$ |
| $a$(kpc) | 3.5 | 3.9 | 3.5 |
| $b$(kpc) | 1.4 | 0.6 | 1.4 |
| $c$(kpc) | 1.0 | 0.1 | 1.0 |
| $R_{\rm CR}$(kpc) | 4.91 | 4.94 | 4.54 |
| $R_{\rm OLR}$(kpc) | 7.69 | 7.69 | 7.40 |

we present the results. In Sect. 4.5 we explain how the bar can create a radial velocity gradient as observed. In Sect. 4.6 we discuss the similarities between our results and the ones in W13 and in Sect. 4.7 we conclude.

## 4.2 Simulations

We use the 3D test particle simulations of the thin and thick disk of the Milky Way described in M13. The rigid background gravitational potential in these simulations includes an axisymmetric part (composed of a dark halo, and a thin and a thick disk) and a non-axisymmetric perturbation to represent the Galactic bar. The bar potential follows a Ferrers (1870) model and we varied its structural parameters (with values taken from the literature) but with a constant pattern speed $\Omega_{\rm b} = 50$ km s$^{-1}$ kpc$^{-1}$. For the comparison with the *RAVE* data we focus on simulations with three bar potentials: the Default Bar, the Long Bar, and the Less Massive Bar (corresponding to GB2, LB2, and GB1 in M13). We choose the snapshot of the simulations at $t = 24T_{\rm bar}$, which corresponds to $\sim 3$ Gyr after the introduction of the bar in the simulations (see M13). In the Default Bar case, there are $N_{\rm thin} = 10^9$ particles in the thin disk population and $N_{\rm thick} = 2\times10^8$ particles in the thick disk (to have a thick-to-thin density of particles normalization of $\sim 10\%$ at the Sun). For the remaining cases we only have low resolution simulations with $N_{\rm thin} = 5\times10^7$ and $N_{\rm thick} = 10^7$ particles for the thin and the thick disk, respectively. The parameters of the simulations are summarized in Table 4.1.

In this Chapter $(R, \phi, z)$ are the Galactocentric cylindrical coordinates, where $\phi$ is the angle from the long axis of the bar in the direction of rotation of the Galaxy. The cylindrical velocities are $(v_R, v_\phi, v_z) = \left(\dot{R}, R\dot{\phi}, \dot{z}\right)$. Right ascension, declination, and heliocentric distance are denoted as $(\alpha, \delta, d)$, and the proper motions and line of sight velocity as $(\mu_\alpha, \mu_\delta, v_{\rm los})$.

## 4.3 Selection function and errors

### 4.3.1 Red Clump stars

Both S11 and W13 use Red Clump stars because they are promising standard candles, since they are easy to identify in the HR diagram, and while being relatively unaffected by extinction their $K$-band magnitude depends only weakly on metallicity and age. In

W13 the red clump is selected from the internal *RAVE* release from October 2011[2] (see the DR3 paper, Siebert et al. 2011b, for stellar parameter determination), as those stars with

$$0.55 \leq J_{\rm BB} - K_{\rm BB} \leq 0.8 \quad \text{and} \quad 1.8 \leq \log g \leq 3.0. \tag{4.1}$$

The absolute magnitude associated with the Red Clump stars is taken to be $M_K = -1.65$, following Alves (2000).

### 4.3.2 *RAVE* selection function

We applied the *RAVE* selection function in the space of observables $(\alpha, \delta, K)$ to the simulations. We did this as follows:

- we chose the position of the Sun in the simulated Galaxy; the default position is $(R, \phi, z) = (8\ \text{kpc}, -20^\circ, 0)$, in the range of current determinations (Bissantz & Gerhard 2002);
- we transformed the spatial coordinates of the simulation into the observables $(\alpha, \delta)$ and heliocentric distance $d$;
- we assigned $K$ magnitudes to the particles in the simulation, assuming they are Red Clump stars with $M_K = -1.65$. Then the apparent magnitude is given by $K = M_K + 5\,(\log_{10} d - 1)$;
- we binned the Red Clump stars used in W13 in the $(\alpha, \delta, K)$ space, with $N_{\rm b}$ bins of size $10^\circ \times 10^\circ \times 0.2$ mag and $\alpha \in [0, 360^\circ]$, $\delta \in [-90^\circ, 0]$, $K \in [2, 12]$;
- we binned in the same space and in the same way the particles from the simulation that are inside a sphere of radius 3 kpc from the Sun;
- for $i = 1, ..., N_{\rm b}$, if the $i$-th bin in the simulation contains $N_i \geq N_i^R$ particles (where $N_i^R$ is the number of stars in the same bin in *RAVE* ) we randomly downsampled it to $N_i^R$ particles; if $N_i^R > N_i \geq N_i^R - \sqrt{N_i^R}$ we kept the $N_i$ particles (because $N_i^R$ and $N_i$ differ less than the corresponding Poisson noise error); however, not all the bins of the simulations are populated enough: we excluded from the comparison those bins with $N_i < N_i^R - \sqrt{N_i^R}$ (this only happened for less than $\sim 0.05\%$ of the bins for the high resolution simulations, and also in the low resolution case after the treatment explained in Sect. 4.4.3).

We repeated this procedure obtaining 100 different random samples of each simulation, where the $\alpha$, $\delta$ and $K$ distribution are almost perfectly matched and the total number of star particles differs from the *RAVE* Red Clump sample in W13 by less than 0.5% for the high resolution simulations, leaving 72,064 particles in the Default Bar case. The top panel of Fig. 4.1 shows the $(R, z)$ distribution of Red Clump stars in W13, while in the bottom we have plotted the result of the procedure described above for our standard simulation and Sun's position. We see that we are successful in reproducing how the different *RAVE* fields are populated. The differences in $(R, z)$ (e.g., inside the contour enclosing 21% of the stars) are due to the small differences described above in the bins in the $(\alpha, \delta, K)$ space.

[2] Here $K$ is used to denote $K$-band magnitudes in the $2MASS$ system, while $J_{\rm BB}$ and $K_{\rm BB}$ denote the $J$ and $K$-band magnitudes in the Bessell & Brett (1989) system.

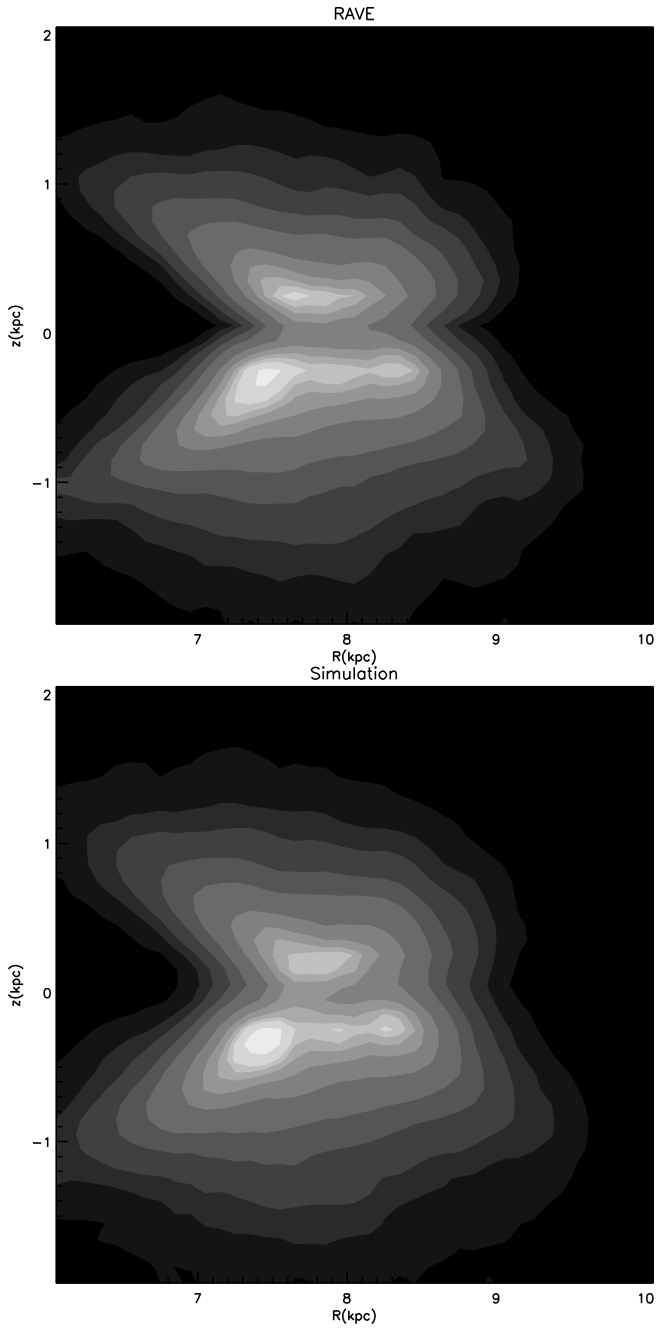


**Figure 4.1:** $(R, z)$ distribution of stars in the *RAVE* sample used in W13 (top) and in the simulation with default Sun's position after the application of the *RAVE* selection function (bottom). The contours enclose $2, 6, 12, 21, 33, 50, 68, 80, 90, 95$ and 99% of the stars.

### 4.3.3 Error convolution

For the comparison between data and simulations we proceeded to convolve the latter with the errors estimated for the *RAVE* survey.

We produced a simple error model, where the errors in proper motion and line of sight velocity are function of the $K$ magnitude only. This was done by fitting second order polynomials to $K$ vs. $e_{\rm p.m.}$ and $K$ vs. $e_{\rm los}$ for the Red Clump stars in DR3. We also derived an error in distance $e_d$ propagating the error in $K$ ($e_K \sim 0.04$ mag) and the spread in absolute magnitudes of the red clump ($e_{M_K} = 0.22$ mag, Alves 2000). The resulting relative error in distance is $e_d/d \sim 0.1$, that we assumed to be the same for all particles in our simulations.

The error convolution was done in the observable space $(\alpha, \delta, d, \mu_\alpha, \mu_\delta, v_{\rm los})$, assuming Gaussian errors in each quantity.

## 4.4 Results

### 4.4.1 Default case

As a default case we place the Sun at $(R, \phi, z) = (8\ {\rm kpc}, -20^\circ, 0)$ and we choose the Default Bar model. In this case $R_0/R_{\rm OLR} = 1.04$, where $R_0$ is $R$ of the Sun and $R_{\rm OLR}$ is the Galactocentric distance of the Outer Lindblad Resonance.

The top row of Fig. 4.2 shows the average velocities as a function of $R$ and $z$, for all the particles inside a sphere of radius 3 kpc from the Sun, with no error convolution yet applied. From left to right we show contour plots of $\overline{v}_R$, $\overline{v}_\phi$, and $\overline{v}_z$. As in W13, the data are averaged inside bins of 100 pc size in $(X', Y')$, box smoothed on a scale of 200 pc. As it is apparent from these plots, $\overline{v}_R$ decreases increasing the $R$ distance in the simulated Galaxy. Moreover, $\overline{v}_R$ is rather symmetric with $z$. The central panel shows that the rotational velocity of the stars in the Galactic disk(s) $\overline{v}_\phi$ decreases with distance from the plane. This is because the velocity dispersion increases with $z$ and because the asymmetric drift increases with the velocity dispersion (Binney & Tremaine 2008). The rightmost panel shows instead how $\overline{v}_z \sim 0$ everywhere in the simulated sample, i.e., the distribution function of our simulations is an even function of $v_z$.

The bottom row of Fig. 4.2 shows the same quantities as in the top panels, after the application of the *RAVE* selection function. The plotted values were obtained averaging over the 100 random samples of the simulation, distributed in $(\alpha, \delta, K)$ as in *RAVE*. We only consider the bins including more than 50 particles. These contour plots show that the decreasing $\overline{v}_R$ gradient is preserved after the selection function has been applied to the simulation. In fact the gradient is even enhanced: the yellow regions at $R \sim 7$ kpc are formed by particles with $\overline{v}_R > 5$ km s$^{-1}$, and the blue/green regions at $R \sim 8.5$ kpc by particles with slightly negative $\overline{v}_R$. From the second and third panel we also see that the selection function does not induce any significant difference in $\overline{v}_\phi$ and $\overline{v}_z$: unlike W13, in the samples presented in this work we do not detect any significant $\overline{v}_z$ gradient with respect to $z$ or $R$.

The reason why the selection function enhances the $v_R$ gradient is readily understood from Fig. 4.3. Here $X'$ and $Y'$ are the cartesian coordinates centered at the Sun, the Galactic Center is placed at $(X', Y') = (-8\ {\rm kpc}, 0)$, and the colors represent $\overline{v}_R$ for particles inside a sphere of radius 3 kpc from the Sun in bins of 100 pc size. The

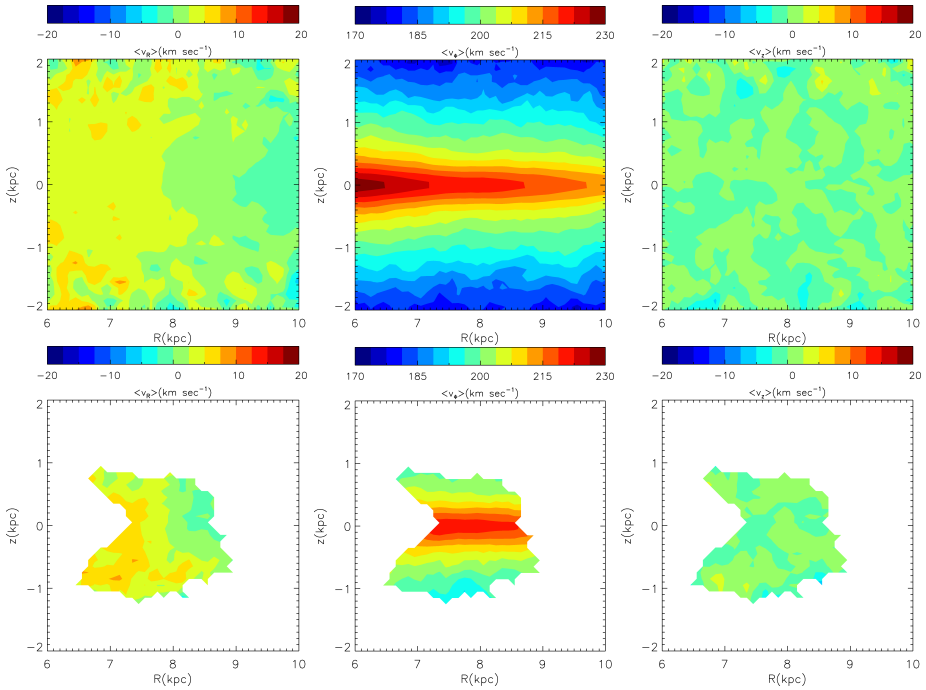


**Figure 4.2:** Average velocities for particles inside a sphere of radius 3 kpc, when the Sun is placed at $(R, \phi, z) = (8 \text{ kpc}, -20°, 0)$ and for the Default Bar model. Top row: contour plots in the $(R, z)$ plane, with binsize 100 pc and box smoothing on a scale of 200 pc. Bottom row: as in the top row, but after the application of the *RAVE* selection function. The averages in the bottom panels correspond to those obtained using 100 random samples of the simulation.

contours enclose 90% of particles with $-1.5 \text{ kpc} < z < 0$ (black) and $0 < z < 1.5$ kpc (red), when the *RAVE* selection function is applied. These contours therefore show that the selection function encloses mostly particles with negative $X'$ and positive $Y'$ (with $\phi < -20°$), where the gradient is steeper.

This analysis shows that $v_R$ is the velocity component most influenced by the bar (and that no signature is readily apparent in $v_z$) and therefore we focus in the rest of the Chapter on the $R$ gradients of $\overline{v}_R$ and on their dependence on $z$.

In Fig. 4.4 we look closer at the $\overline{v}_R$ trends with $R$, slicing the particles at different $z$. The quantity $\overline{v}_R$ is computed inside $R$ bins of size 0.5 kpc. The black line has been obtained using all the particles in the simulations inside a sphere of 3 kpc radius from the Sun, the red line those that remain after applying the *RAVE* selection function only, and the blue line the case where the error convolution is applied together with the selection function. The shaded areas represent the standard errors of the mean inside each bin. For the red and blue curves we show the maximum error amongst the 100 random samples[3].

[3] We could not use the standard deviation of these 100 random samples, as they are not completely

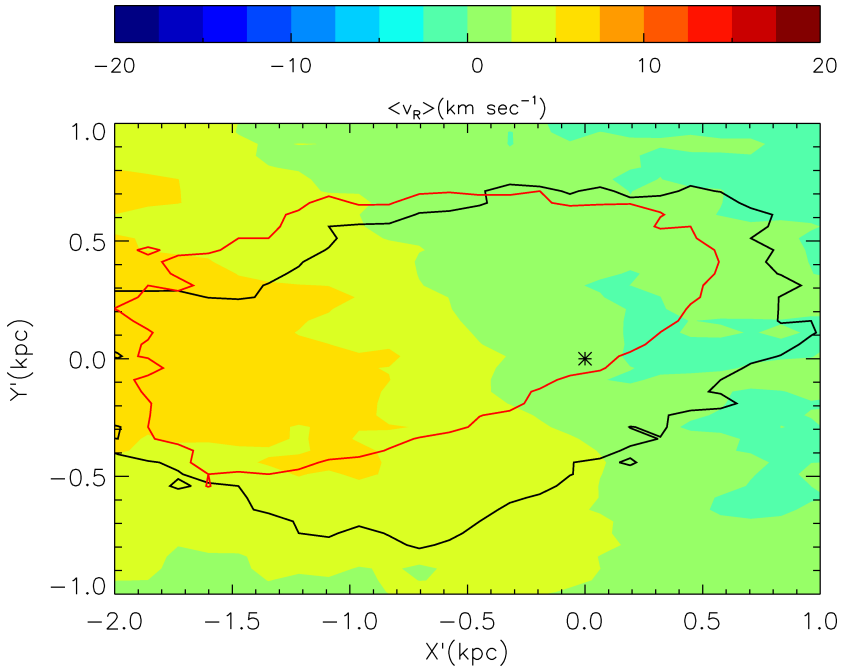


**Figure 4.3:** Trends in $\overline{v}_R$ as a function of the cartesian coordinates $(X', Y')$ centered on the Sun, with the Galactic center at $(X', Y') = (-8 \text{ kpc}, 0)$. These are computed for particles inside a sphere of radius 3 kpc, when the Sun is placed at $(R, \phi, z) = (8 \text{ kpc}, -20°, 0)$ and for the Default Bar model. The plotted data are averaged inside bins of 100 pc size in $(X', Y')$, box smoothed on a scale of 200 pc. The contours enclose 90% of particles with $-1.5 \text{ kpc} < z < 0$ (black) and $0 < z < 1.5$ kpc (red), when the *RAVE* selection function is applied.

We only show the bins with errors smaller than 5 km s$^{-1}$ and including more than 50 particles. The black line confirms what we saw in Fig. 4.2, namely that $\overline{v}_R$ decreases with $R$ in each of the 5 slices in $z$.

The numbers in the bottom right of each panel quantify the magnitude of the gradient: $m$ represents the slope of the linear regression of the $\overline{v}_R$ values inside the plotted bins, and $\sigma_m$ its uncertainty (computed from the errors represented by the shaded areas). Although $\overline{v}_R$ slowly decreases ($m \sim -1$ km s$^{-1}$ kpc$^{-1}$) with $R$ in each $z$ slice, the trend is not simple. It is the composition of a flat/increasing gradient for $R \lesssim 7.5$ kpc and a decreasing one for $R \gtrsim 7.5$ kpc. This break happens almost in correspondence with the Outer Lindblad Resonance ($R_{\rm OLR} = 7.69$ kpc). This composite behavior makes $m$ shallower than if only the data points with $R \gtrsim 7.5$ kpc were to be fitted.

The *RAVE* selection function (red line) in this Default Bar case makes the gradients

independent. This is because in some of the $(\alpha, \delta, K)$ bins there are as many particles in the simulations as stars in the *RAVE* Red Clump sample.

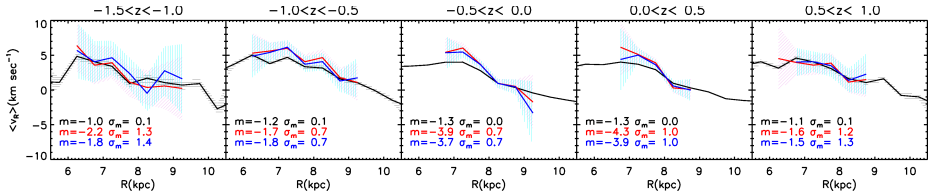


**Figure 4.4:** Average cylindrical radial velocity $\overline{v}_R$ as a function of radial distance in the plane $R$, for particles inside a sphere of radius 3 kpc, when the Sun is placed at $(R, \phi, z) = (8 \text{ kpc}, -20°, 0)$ and for the Default Bar model. The bin size is 0.5 kpc. Each panel corresponds to particles in a certain range of $z$. The black curve corresponds to the whole sample and the error bands are the statistical error on the mean. The other two curves represent the sample after the application of the *RAVE* selection function, without (red line) and with (blue line) error convolution. The quantities represented by the red and blue curves are averaged over 100 random subsamples of the simulation. The error bands correspond to the maximum error on the mean amongst the different samples. We only show the bins with errors smaller than 5 km s$^{-1}$ and more than 50 particles.

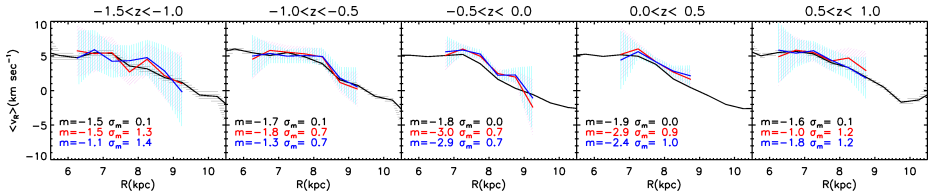


**Figure 4.5:** As in Fig. 4.4, but with the Sun placed at $(R, \phi, z) = (8 \text{ kpc}, -40°, 0)$.

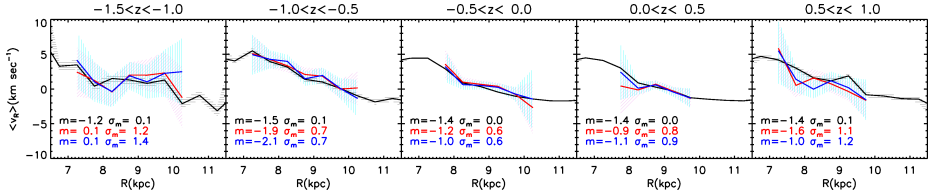


**Figure 4.6:** As in Fig. 4.4, but with the Sun placed at $(R, \phi, z) = (9 \text{ kpc}, -20°, 0)$.

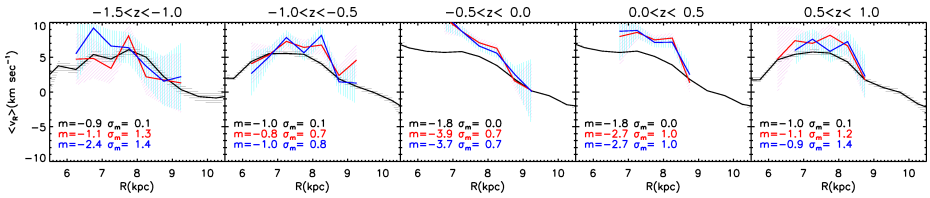


**Figure 4.7:** As in Fig. 4.4, but with the Long Bar. Note that in this case, the simulation has been mirrored with respect to the $z = 0$ plane, which implies that the black curves in the 2nd and 5th, and in the 3rd and 4th panels are identical. However, the *RAVE* selection function does depend on Galactic latitude, resulting in different blue and red curves in each panel.

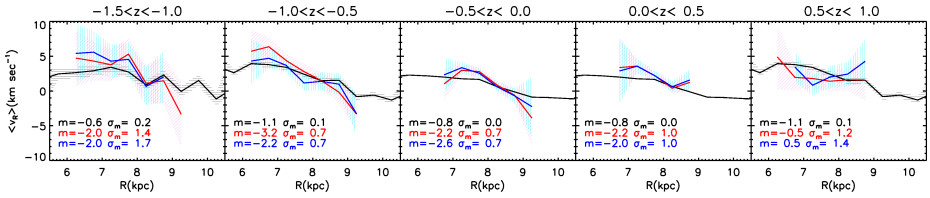


**Figure 4.8:** As in Fig. 4.4, but with less massive bar. As in the previous figure, the simulations have been mirrored with respect to the $z = 0$ plane.

steeper, because the bins with $R \lesssim 7.5$ kpc are excluded (or less populated) and for this reason they do not reduce the slope. This is especially clear for the two slices $-0.5$ kpc $< z < 0$ and $0 < z < 0.5$ kpc, where the retained bins are all very near to the Sun (because the *RAVE* fields have $|b| > 25°$, see Fig. 4.1). Since the Sun happens to be placed in the middle of the region where $\overline{v}_R$ decreases and we only have the nearest bins, the resulting gradient is very steep ($m \sim -4$ km s$^{-1}$ kpc$^{-1}$). This effect is mitigated further away from the plane, because the $R$ extent of the survey becomes larger.

Finally, we note that the effect of error convolution is very small, with the blue curves within the red (error-free) uncertainty bands.

## 4.4.2 Other locations in the Default Bar

### 4.4.2.1 $R = 8$ kpc, $\phi = -40°$

We consider now the effect of placing the Sun at a different position, namely $(R, \phi, z) = (8 \text{ kpc}, -40°, 0)$, thus at a larger angle from the long axis of the bar.

Fig. 4.5 shows that, in this case, the $v_R$ gradient in the whole sphere is steeper than in the default case. In fact, the steepest gradient in the simulation is reached at $\phi = -45°$ (the gradient is a periodic function of $\phi$, with period $\pi$; for a detailed analysis of the periodic response of a stellar disk to a bar see Mühlbauer & Dehnen 2003). We see that in the slices closest to the Galactic plane ($|z| < 0.5$ kpc) the effect of the selection function is similar to that of the default case: the Sun is placed in the region where the gradient is steepest and, since we remove the outermost bins, the mean velocity gradient

is strongly enhanced. Again, at $|z| > 0.5$ kpc the slope is smaller, because of the larger $R$ extent of the sample.

#### 4.4.2.2 $R = 9$ kpc, $\phi = -20°$

In Fig. 4.6 we present the analysis of the radial velocity gradient behavior in a volume further out in the Galaxy, namely at $(R, \phi, z) = (9 \text{ kpc}, -20°, 0)$. This case was chosen to illustrate the effect of the distance from the Outer Lindblad Resonance, here $R_0/R_{\rm OLR} = 1.17$.

In this case the slope over the whole sphere is steeper than in the default case. This happens because the volume is beyond the Outer Lindblad Resonance and is therefore less affected by the particles with $R \lesssim 7.5$ kpc (which were responsible for the positive/flat gradient). However, the local gradient at $R = 9$ kpc is shallower than the one at $R = 8$ kpc, i.e., $\left|\frac{\mathrm{d}\overline{v}_R}{\mathrm{d}R}(9 \text{ kpc})\right| < \left|\frac{\mathrm{d}\overline{v}_R}{\mathrm{d}R}(8 \text{ kpc})\right|$. For this reason, when we apply the selection function, for $|z| < 0.5$ kpc the slope $m$ becomes smaller in magnitude (than without selection function and than the default case with selection function). On the contrary, for the slice with $-1$ kpc $< z < -0.5$ kpc it becomes steeper because in this case the steepest part of the curve is included in the regression. Finally, in the outermost slice ($-1.5$ kpc $< z < -1$ kpc) the low number of particles make the $\overline{v}_R$ profile noisy and this washes out the $\overline{v}_R$ gradient.

### 4.4.3 Other bar models

The simulations in M13 include two other bar models: the Long Bar model with a different geometry but with the same mass as the default bar, and a second one with same geometry but half the mass, the low mass bar. However in these cases our simulations have lower resolution than the Default Bar case (see Sect. 4.2). In order to get the same number of objects as the *RAVE* Red Clump sample, we mirror the particles above and below the $z = 0$ plane (so that we double the resolution). However, we only do this for those $(\alpha, \delta, K)$ bins that contain fewer particles than the observed number of Red Clump stars in *RAVE*. We are allowed to do this because the potential is symmetric with the respect of the Galactic plane and the same is true for our test particle simulations (at least when they reach a steady state). After this operation, the discrepancy in total number of objects between *RAVE* and the simulation is smaller than 1.5%. The regions slightly underpopulated are those with $0 \lesssim \alpha \lesssim 80°$, $320° \lesssim \alpha \lesssim 360°$ and $\delta \lesssim -60°$. In what follows we only consider the standard Sun's location, namely the case with the Sun at $(R, \phi, z) = (8 \text{ kpc}, -20°, 0)$.

#### 4.4.3.1 $R = 8$ kpc, $\phi = -20°$, Long Bar

The Long Bar has a stronger effect than the Default Bar near the Sun, because its gravitational force is larger in the Solar Neighborhood (see M13). This is evident looking at the black line in Fig. 4.7, but also in the red and blue curves which are obtained after applying the *RAVE* selection function and error convolution. Moreover, for $|z| > 0.5$ kpc, $\overline{v}_R$ grows steeply for $R \lesssim 7.5 - 8$ kpc and decreases steeply for $R \gtrsim 7.5 - 8$ kpc. In the central slices the effect of the selection function and error enhances the gradient, for the same reasons as in the standard case. For $|z| > 0.5$ kpc the selection function together

with the errors preferentially pick out bins with smaller $R$, where $\overline{v}_R$ increases, which results in washing out the gradient.

#### 4.4.3.2 $R = 8$ kpc, $\phi = -20°$, Less Massive Bar

As shown from the black lines in Fig. 4.8 and not surprisingly, the gradient induced by the Less Massive Bar is shallower than the Default Bar because the bar is weaker. Formally the force of Less Massive Bar is half that of the Default Bar. However the non-axisymmetric part of the force (i.e., excluding the monopole term associated to the bar) only differs by $\sim 30\%$ in the solar neighborhood (see M13).

Once the selection function and the error convolution have been applied, the resulting $v_R$ gradients are significantly shallower almost everywhere.

## 4.5 Reasons for the velocity gradient

To explain the way the bar can induce a large scale radial velocity gradient in the Milky Way, as in the simulations discussed here, we show Fig. 4.9. In this figure we have plotted the velocity distribution in the $v_R$ and $v_\phi$ components of the simulation with the Default Bar at $\phi = -40°$ and different $R$, inside small cylinders of radius 300 pc and height 600 pc, centered on the Galactic plane. The density field is estimated with an adaptive kernel estimator (see details in M13).

Let us consider an axisymmetric potential similar to the one of a disk galaxy. A star with angular momentum $L_z = Rv_\phi$ is associated with a circular orbit with radius $R_\mathrm{g}$, the "guiding center", such that $L_z = R_\mathrm{g}^2 \Omega\left(R_\mathrm{g}\right)$. Therefore, when it passes from $R$, its tangential velocity is

$$v_\phi = \frac{R_\mathrm{g}^2 \Omega\left(R_\mathrm{g}\right)}{R}, \tag{4.2}$$

Near the Sun, the bar most strongly influences the stars with $R_\mathrm{g} = R_\mathrm{OLR}$. This is shown in Fig. 4.9, where the red dashed line denotes $v_\mathrm{OLR}$, which is $v_\phi$ of orbits that have $R_\mathrm{g} = R_\mathrm{OLR}$, computed using the monopole component of the Fourier decomposition of the potential in $\phi$ and where $R$ is taken at the center of the volumes. In fact, we note that around $v_\mathrm{OLR}$ the velocity distribution is split in two parts: the particles with $v_\phi > v_\mathrm{OLR}$ have $\overline{v}_R \lesssim 0$, the particles with $v_\phi < v_\mathrm{OLR}$ have $\overline{v}_R > 0$ (Kalnajs 1991 introduced the idea that the Outer Lindblad Resonance could account for bifurcation of the Solar Neighborhood velocity distribution). We dub the former group "LSR Mode" and the latter "OLR Mode", in the same fashion of Dehnen (2000), that linked the latter to the Hercules stream. The division is particularly clear for the volume centered at $R = 8$ kpc.

A first order treatment of nearly circular orbits in a weak bar potential (Binney & Tremaine 2008, Sect. 3.3.3) shows that the bar gravitational force stretches these orbits in two directions near the Outer Lindblad Resonance and in the frame of reference of the bar: the orbits with $R_\mathrm{g} < R_\mathrm{OLR}$ are stretched perpendicular to the long axis of the bar and the orbits with $R_\mathrm{g} > R_\mathrm{OLR}$ are aligned parallel to the long axis of the bar. The nearer $R_\mathrm{g}$ to $R_\mathrm{OLR}$, the stronger the effect. When they pass near the Sun, the orbits with $R_\mathrm{g} < R_\mathrm{OLR}$ ($R_\mathrm{g} > R_\mathrm{OLR}$) have positive (negative) $v_R$[4]. Orbits with $R_\mathrm{g}$ far enough

[4] This prediction of the first order treatment can be obtained from the time derivative of Eq. (3.148a) of Binney & Tremaine (2008), and is confirmed in our simulations.

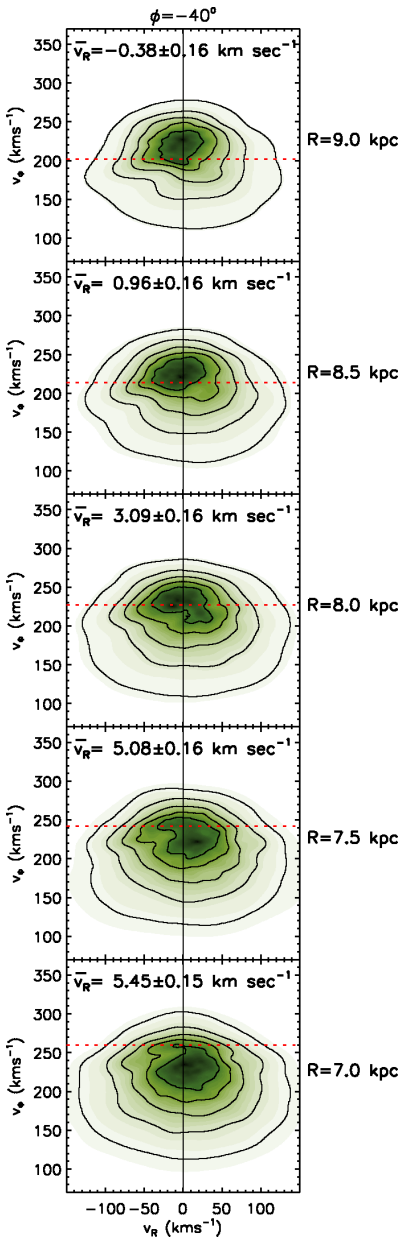


**Figure 4.9:** Velocity distribution in cylinders of radius 300 pc and height 600 pc, centered at $\phi = -40°$, $z = 0$ and different radii for the Default Bar case, inside the 3 kpc sphere centered at $(R, \phi, z) = (8 \text{ kpc}, -40°, 0)$. The density distribution is obtained with an adaptive kernel estimator (see Chapter 2).

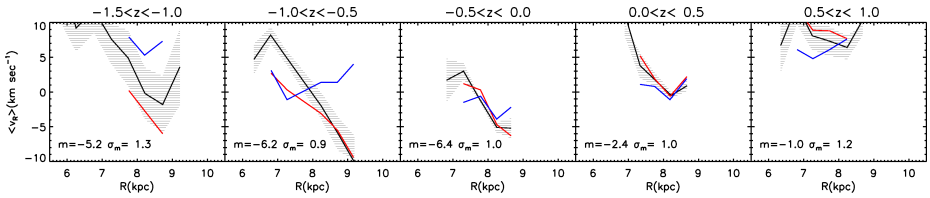


**Figure 4.10:** As in Fig. 4.4, but for the *RAVE* Red Clump stars used in W13. The shaded areas represent the measurement errors, the blue line the results obtained with the UCAC3 proper motions, the red line the results obtained with the SPM4 proper motions (see W13).

from $R_{\rm OLR}$ are not very affected by the bar, and on average have $v_R \sim 0$. We see this reflected in Fig. 4.9: the OLR Mode is formed by stars with $R_{\rm g} < R_{\rm OLR}$, and the LSR Mode by stars with $R_{\rm g} > R_{\rm OLR}$.

When the volume is centered near $R_{\rm OLR}$ (e.g., $R = 7.5 - 8$ kpc in Fig. 4.9), the orbits of the OLR Mode with $R_{\rm g} < R_{\rm OLR}$ dominate the velocity distribution of the particles, resulting in $\overline{v}_R > 0$ for the whole volume. As we go further from the Outer Lindblad Resonance less particles populate the OLR Mode. In particular, if we only consider volumes centered at $R > R_{\rm OLR}$, this results in a negative $\overline{v}_R$ gradient (positive for $R < R_{\rm OLR}$). This is why we observe $\overline{v}_R$ gradients and a double behavior inside and outside the Outer Lindblad Resonance.

Note that, because of the symmetry of the problem, for volumes centered at positive $\phi$ the situation is reversed: $\overline{v}_R$ of the OLR Mode is negative and the gradient is positive.

## 4.6 Discussion

In this Section we compare our results in the case where the selection function and the error convolution are applied (red and blue lines in Figs. 4.4 - 4.8, that are similar) with the findings of W13 and in particular with the $v_R$ trends in their Fig. 8 (here reproduced in Fig. 4.10). Depending on the assumed Sun's motion with the respect of the Local Standard of Rest, the curves may shift up or down in $v_R$, but the overall trends remain unaffected (as shown in Fig. 9 in W13). Note that we have not included a correction for the solar motion in our analysis so far. Nonetheless, the $v_R$ values are comparable to those of W13.

However, only a qualitative comparison is warranted, as our simulation does not really reproduce in detail the properties of the Milky Way (e.g, the rotation curve is falling off near the Sun, the peak velocity is larger than observed, etc). Furthermore, as we have noted, after the error convolution and *RAVE* selection function are applied, the underlying trends are sometimes modified, implying that care should be taken to avoid over interpretation of the results.

An important difference is that the radial velocity gradients found in *RAVE* (Fig. 4.10) are much steeper than in any of our models (Fig. 4.4 - 4.8), except perhaps for the slices with $z > 0$. In magnitude, the model gradients resemble more the low limit of the S11 estimate, i.e., $\frac{{\rm d}\overline{v}_R}{{\rm d}R} \gtrsim 3$ km s$^{-1}$ kpc$^{-1}$. The trends are also different in the sense that most of the cases we have explored show a flat/increasing part (e.g., at $R < 7.5$ kpc for

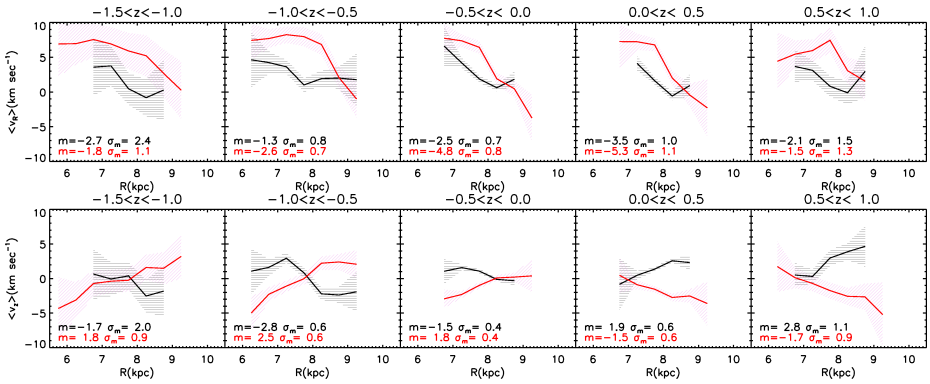


**Figure 4.11:** Effect of a systematic errors in the distance determination on the $\overline{v}_R$ (top row) and $\overline{v}_z$ (bottom row) trends in the Default Bar case. The simulation is also convolved with the random errors. Black lines: 20% systematic underestimation of the distances. Red lines: 20% systematic overestimation of the distances.

the default case) followed by a steeper decline at larger radii, a behavior that seems to be absent (or is not as clear) in the data as shown in Fig. 4.10.

Although as stated above, in absolute terms the actual values of $v_R$ depend on the solar motion, in Fig. 10 we note that the mean value of $v_R$ changes with distance from the plane, when averaged over the whole radial distance range. This behavior is also present, and in the same sense, in our default model, where for the three $z$ slices at $z > -0.5$ kpc: in the central bins $\overline{v}_R > 0$ for $R < 8$ kpc and $v_R \gtrsim 0$ for $R > 8$ kpc, and $\overline{v}_R > 0$ everywhere for $z > 0.5$ kpc.

Systematic errors in the distances (and more specifically the assumed absolute magnitude for the Red Clump stars) could also affect our results. However, we find that when we use the other Red Clump magnitude normalizations considered in W13 ($M_K = -1.54$ and $M_K = -1.64 + 0.0625|z(\mathrm{kpc})|$) our conclusions are not affected, because these only induce small distance changes ($\sim 5\%$). On the other hand, if the distances were more significantly overestimated, by for example 20%, the $v_R$ gradients would become steeper as shown by the red curves in the top panels of Fig. 4.11, while an underestimation by the same magnitude would lead to shallower gradients as shown by the black curves in the figure. Interestingly, in the case that the distances are overestimated a gradient in $v_z$ with radius is also induced as shown in the bottom panels of Fig. 4.11, which is positive below the plane, and negative above the plane, i.e. in the same sense as found by W13. Since in the literature (Alves 2000; Grocholski & Sarajedini 2002; Salaris & Girardi 2002; Groenewegen 2008) most other estimates of the Red Clump magnitude are fainter than what we have assumed, it may seem more likely that the distances in W13 have been systematically overestimated than underestimated[5], however not as extremely as we have tested in these last examples.

It should be noted that the fact that the models explored in this work do not fit the observed data, does not necessarily imply that the Galactic bar is not the cause for the

[5] In fact, Binney et al. (2014) recently estimated the absolute magnitude of the *RAVE* Red Clump stars to be $\sim 0.1$ mag fainter than in W13.

observed gradients. With our models we only have explored a very small portion of a large parameter space and, for example, steeper gradients can be obtained by increasing the bar strength near the Sun, or even with a circular speed curve falling more slowly with $R$, at fixed bar pattern speed[6]. Since some of the kinematic substructure in the Solar Neighborhood can be explained by the bar, we expect that its dynamical effect (for the current bar parameters estimates) should at least be partly responsible for the observed negative $\overline{v}_R$ gradients.

## 4.7 Conclusions

In this work we have proposed a new explanation for the recent discovery (S11, W13) of a negative $R$ gradient of the (galactocentric) radial velocity. We found that the bar can create a negative gradient if the Sun is placed just outside the Outer Lindblad Resonance and at angles from the long axis of the bar similar to the current estimates from the literature. The velocity gradients become steeper when increasing the angle from the bar and also for the Long Bar model. On the other hand, in the Less Massive Bar case they become shallower. Moreover, such gradients do not depend strongly on the height from the Galactic plane. This happens because the bar affects the kinematics of the Galaxy almost in the same way from $z = 0$ to $z \sim 2$ kpc, as explained in M13. Because of this, the bar provides a natural mechanism for the observed gradients at different heights.

We compared the 3D test particle simulations presented in M13 with the findings of *RAVE*, after applying the *RAVE* selection function and proper error convolution. The gradients exist in our simulations for all bar parameters and positions of the Sun explored (all outside the Outer Lindblad Resonance). These gradients are never completely washed out by the selection function and the errors, but rather they are enhanced in some cases. In fact, the gradients in the Solar Neighborhood spheres considered are in general shallower than those observed in the Milky Way, but the selection function can enhance them to the level of $\sim 3-4$ km s$^{-1}$ kpc$^{-1}$ (as e.g., happens for all the studied simulation slices with $|z| < 0.5$ kpc and the Sun centered at $R = 8$ kpc).

However, none of the models that we explored in this work accurately describes the behavior in *RAVE* of $\overline{v}_R$ at every $z$: the gradients are too shallow for $z < 0$. Some models resemble *RAVE* for $z > 0$, especially our Default Bar case at $R = 8$ kpc and $\phi \leq -20°$. We conclude from this that the bar should at least contribute to the negative gradient observed, for position angles with respect to the bar $\phi < 0$ and for locations of the Sun near but outside the Outer Lindblad Resonance ($R > R_{\rm OLR}$).

Furthermore, our simulations do not show any kind of vertical velocity gradient as seen in the data for *RAVE* by W13. This result is consistent with the distribution function of the simulated disks being an even function of $v_z$. On the other hand, the recent paper by Faure et al. (2014) shows that a 3D model for spiral arms is successful in reproducing radial and vertical velocity gradients similar to those observed in W13. In reality both effects of bar and spiral arms probably coexist and shape the velocity distribution of the solar neighborhood. However, while in the case of the bar the slope of the radial velocity gradient depends significantly on the angular location of the observer in the Galaxy, in the case of tightly wound spirals the angle is much less important (Fig. 6

[6] This can be shown in 2D with a simple potential with power-law velocity curve, applying Kuijken & Tremaine (1991) theory for the behavior of the mean velocities under the influence of a non-axisymmetric perturbation of multipole order $m$ (see also Mühlbauer & Dehnen 2003).

and 7 in Faure et al. 2014). Future observations of the Galactic disk (e.g., obtained with the *Gaia* satellite) are expected to be sufficiently extended to distinguish whether the main cause of the radial velocity gradient is the bar or the spiral arms.

A natural future development of this work is to fit the kinematics of the extended Solar Neighborhood with the analytic predictions from the bar perturbation theory, in the same fashion as in Siebert et al. (2012) for the spiral arms, in order to retrieve the best fit values for the bar pattern speed, bar angle, and bar strength.

## Acknowledgments

We would like to thank T. Piffl and M. Williams for useful discussions. We also thank M. Williams for kindly providing the *RAVE* data used in Williams et al. (2013). The authors gratefully acknowledge support from the European Research Council under ERC Starting Grant GALACTICA-240271.

# Bibliography


Abadi, M. G., Navarro, J. F., Steinmetz, M., & Eke, V. R. 2003, ApJ, 591, 499

Agertz, O., Teyssier, R., & Moore, B. 2011, MNRAS, 410, 1391

Aitken, R. G. 1942, Leaflet of the Astronomical Society of the Pacific, 4, 103

Alves, D. R. 2000, ApJ, 539, 732

Antoja, T., Figueras, F., Fernández, D., & Torra, J. 2008, A&A, 490, 135

Antoja, T., Figueras, F., Romero-Gómez, M., Pichardo, B., Valenzuela, O., & Moreno, E. 2011, MNRAS, 418, 1423

Antoja, T., et al. 2012, MNRAS, 426, L1

—. 2014, A&A, 563, A60

Antoja, T., Valenzuela, O., Pichardo, B., Moreno, E., Figueras, F., & Fernández, D. 2009, ApJ, 700, L78

Aristotle. 1491, Meteorologia: With the commentary, De reactione and De intensione et remissione formarum of Gaietanus de Thienis (Ipressa cura ... Ioannis de Foriiuio [et] Gregorij fratrum)

Athanassoula, E. 2002, ApJ, 569, L83

—. 2005, MNRAS, 358, 1477

Aumer, M., & Binney, J. J. 2009, MNRAS, 397, 1286

Battaglia, G., et al. 2005, MNRAS, 364, 433

Baugh, C. M. 2006, Reports on Progress in Physics, 69, 3101

Bell, E. F., et al. 2008, ApJ, 680, 295

Belokurov, V., et al. 2006, ApJ, 642, L137

Benjamin, R. A., et al. 2005, ApJ, 630, L149

Bensby, T., Feltzing, S., & Lundström, I. 2003, A&A, 410, 527

Bensby, T., Feltzing, S., & Oey, M. S. 2014, A&A, 562, A71

Bensby, T., Oey, M. S., Feltzing, S., & Gustafsson, B. 2007, ApJ, 655, L89

Bertin, G., & Lin, C. C. 1996, Spiral structure in galaxies a density wave theory

Bessel, F. W. 1838, MNRAS, 4, 152

Bessell, M. S., & Brett, J. M. 1989, in Lecture Notes in Physics, Berlin Springer Verlag, Vol. 341, Infrared Extinction and Standardization, ed. E. F. Milone, 61

Binney, J., et al. 2014, MNRAS, 437, 351

Binney, J., Gerhard, O., & Spergel, D. 1997, MNRAS, 288, 365

Binney, J., & McMillan, P. 2011, MNRAS, 413, 1889

Binney, J., & Merrifield, M. 1998, Galactic Astronomy

Binney, J., & Spergel, D. 1982, ApJ, 252, 308

Binney, J., & Tremaine, S. 2008, Galactic Dynamics: Second Edition, ed. Binney, J. & Tremaine, S. (Princeton University Press)

Bissantz, N., & Gerhard, O. 2002, MNRAS, 330, 591

Blaauw, A. 1970, in IAU Symposium, Vol. 38, The Spiral Structure of our Galaxy, ed. W. Becker & G. I. Kontopoulos, 199

Blitz, L., & Spergel, D. N. 1991, ApJ, 370, 205

Bosma, A. 1978, PhD thesis, PhD Thesis, Groningen Univ., (1978)

Bournaud, F., Combes, F., & Semelin, B. 2005, MNRAS, 364, L18

Bournaud, F., Elmegreen, B. G., & Martig, M. 2009, ApJ, 707, L1

Bovy, J., et al. 2012a, ApJ, 759, 131

Bovy, J., & Rix, H.-W. 2013, ApJ, 779, 115

Bovy, J., Rix, H.-W., & Hogg, D. W. 2012b, ApJ, 751, 131

Bovy, J., Rix, H.-W., Hogg, D. W., Beers, T. C., Lee, Y. S., & Zhang, L. 2012c, ApJ, 755, 115

Bovy, J., Rix, H.-W., Liu, C., Hogg, D. W., Beers, T. C., & Lee, Y. S. 2012d, ApJ, 753, 148

Brook, C. B., Kawata, D., Gibson, B. K., & Freeman, K. C. 2004, ApJ, 612, 894

Byrd, G. G., Valtonen, M. J., Valtaoja, L., & Sundelius, B. 1986, A&A, 166, 75

Cabrera-Lavers, A., González-Fernández, C., Garzón, F., Hammersley, P. L., & López-Corredoira, M. 2008, A&A, 491, 781

Cabrera-Lavers, A., Hammersley, P. L., González-Fernández, C., López-Corredoira, M., Garzón, F., & Mahoney, T. J. 2007, A&A, 465, 825

Carpintero, D. D., & Aguilar, L. A. 1998, MNRAS, 298, 1

Ceverino, D., & Klypin, A. 2007, MNRAS, 379, 1155

Churchwell, E., et al. 2009, PASP, 121, 213

Cole, A. A., & Weinberg, M. D. 2002, ApJ, 574, L43

Combes, F. 2008, ArXiv e-prints

Contopoulos, G. 1975, ApJ, 201, 566

—. 1979, A&A, 71, 221

—. 1981, A&A, 104, 116

Contopoulos, G., & Grosbol, P. 1986, A&A, 155, 11

Contopoulos, G., & Mertzanides, C. 1977, A&A, 61, 477

Contopoulos, G., & Papayannopoulos, T. 1980, A&A, 92, 33

Dalton, G., et al. 2012, in Society of Photo-Optical Instrumentation Engineers (SPIE) Conference Series, Vol. 8446, Society of Photo-Optical Instrumentation Engineers (SPIE) Conference Series

de Bruijne, J. H. J. 2012, Ap&SS, 341, 31

de Jong, J. T. A., Yanny, B., Rix, H.-W., Dolphin, A. E., Martin, N. F., & Beers, T. C. 2010, ApJ, 714, 663

de Jong, R. 2011, The Messenger, 145, 14

De Simone, R., Wu, X., & Tremaine, S. 2004, MNRAS, 350, 627

Dehnen, W. 1998, AJ, 115, 2384

—. 1999, ApJ, 524, L35

—. 2000, AJ, 119, 800

Dehnen, W., & Binney, J. 1998a, MNRAS, 294, 429

Dehnen, W., & Binney, J. J. 1998b, MNRAS, 298, 387

Di Matteo, P., et al. 2014, ArXiv e-prints

Dinescu, D. I. 2002, in Astronomical Society of the Pacific Conference Series, Vol. 265, Omega Centauri, A Unique Window into Astrophysics, ed. F. van Leeuwen, J. D. Hughes, & G. Piotto, 365

D'Onghia, E., Vogelsberger, M., & Hernquist, L. 2013, ApJ, 766, 34

Drimmel, R., & Spergel, D. N. 2001, ApJ, 556, 181

Dwek, E., et al. 1995, ApJ, 445, 716

Efremov, Y. N. 2011, Astronomy Reports, 55, 108

Eggen, O. J. 1958, MNRAS, 118, 154

—. 1971, PASP, 83, 271

—. 1996, AJ, 112, 1595

Eggen, O. J., Lynden-Bell, D., & Sandage, A. R. 1962, ApJ, 136, 748

Ewen, H. I., & Purcell, E. M. 1951, Nature, 168, 356

Fall, S. M., & Efstathiou, G. 1980, MNRAS, 193, 189

Famaey, B., Jorissen, A., Luri, X., Mayor, M., Udry, S., Dejonghe, H., & Turon, C. 2005, A&A, 430, 165

Famaey, B., & McGaugh, S. S. 2012, Living Reviews in Relativity, 15, 10

Faure, C., Siebert, A., & Famaey, B. 2014, MNRAS, 440, 2564

Fehrenbach, C., Burnage, R., Duflot, M., Peton, A., Rolland, L., Genty, V., & Mannone, C. 1987, A&AS, 71, 263

Feng, C.-C., Lin, L.-H., Wang, H.-H., & Taam, R. E. 2014, ApJ, 785, 103

Ferdosi, B. J., Buddelmeijer, H., Trager, S. C., Wilkinson, M. H. F., & Roerdink, J. B. T. M. 2011, A&A, 531, A114

Fermani, F., & Schönrich, R. 2013, MNRAS, 432, 2402

Fernie, J. D. 1969, PASP, 81, 707

Ferrers, N. M. 1870, Royal Society of London Philosophical Transactions Series I, 160, 1

Fraternali, F., & Binney, J. J. 2008, MNRAS, 386, 935

Freeman, K., et al. 2013, MNRAS, 428, 3660

Freeman, K. C. 1970, ApJ, 160, 811

Freeman, K. C. 1991, in Dynamics of Disc Galaxies, ed. B. Sundelius, 15

Freeman, K. C. 2012, in Astronomical Society of the Pacific Conference Series, Vol. 458, Galactic Archaeology: Near-Field Cosmology and the Formation of the Milky Way, ed. W. Aoki, M. Ishigaki, T. Suda, T. Tsujimoto, & N. Arimoto, 393

Fuhrmann, K. 2011, MNRAS, 414, 2893

Fux, R. 2001, A&A, 373, 511

Galilei, G. 1989, Sidereus Nuncius, Or The Sidereal Messenger (University of Chicago Press)

Gardner, E., & Flynn, C. 2010, MNRAS, 405, 545

Gerhard, O. 2011, Memorie della Societa Astronomica Italiana Supplementi, 18, 185

Gerin, M., Combes, F., & Athanassoula, E. 1990, A&A, 230, 37

Gilmore, G., et al. 2012, The Messenger, 147, 25

Gilmore, G., & Reid, N. 1983, MNRAS, 202, 1025

Goldreich, P., & Lynden-Bell, D. 1965, MNRAS, 130, 97

Golubov, O., et al. 2013, A&A, 557, A92

Grand, R. J. J., Kawata, D., & Cropper, M. 2014, MNRAS, 439, 623

Grocholski, A. J., & Sarajedini, A. 2002, AJ, 123, 1603

Groenewegen, M. A. T. 2008, A&A, 488, 935

Guedes, J., Callegari, S., Madau, P., & Mayer, L. 2011, ApJ, 742, 76

Hammersley, P. L., Garzón, F., Mahoney, T. J., López-Corredoira, M., & Torres, M. A. P. 2000, MNRAS, 317, L45

Hayden, M. R., et al. 2014, AJ, 147, 116

Helmi, A. 2008, A&A Rev., 15, 145

Helmi, A., Navarro, J. F., Nordström, B., Holmberg, J., Abadi, M. G., & Steinmetz, M. 2006, MNRAS, 365, 1309

Helmi, A., & White, S. D. M. 1999, MNRAS, 307, 495

Henon, M., & Heiles, C. 1964, AJ, 69, 73

Hernquist, L. 1990, ApJ, 356, 359

—. 1993, ApJS, 86, 389

Herschel, W. 1785, Royal Society of London Philosophical Transactions Series I, 75, 213

Holmberg, J., Nordström, B., & Andersen, J. 2007, A&A, 475, 519

Hubble, E. P. 1925, The Observatory, 48, 139

Hyginus. 2014, De Astronomia libri quattuor, `http://www.thelatinlibrary.com/hyginus.html`

Jansky, K. G. 1933, Nature, 132, 66

Jurić, M., et al. 2008, ApJ, 673, 864

Kaasalainen, M. 1994, MNRAS, 268, 1041

Kalnajs, A. J. 1991, in Dynamics of Disc Galaxies, ed. B. Sundelius, 323

Kant, I. 1755, Allgemeine Naturgeschichte und Theorie des Himmels

Kapteyn, J. C. 1892, PASP, 4, 259

Kapteyn, J. C. 1905, in , 257

—. 1909, ApJ, 29, 46

—. 1922, ApJ, 55, 302

Kapteyn, J. C., & van Rhijn, P. J. 1920, ApJ, 52, 23

Katz, N., & Gunn, J. E. 1991, ApJ, 377, 365

Kazantzidis, S., Bullock, J. S., Zentner, A. R., Kravtsov, A. V., & Moustakas, L. A. 2008, ApJ, 688, 254

Keller, S. C., et al. 2007, PASA, 24, 1

Kobayashi, C., Springel, V., & White, S. D. M. 2007, MNRAS, 376, 1465

Kormendy, J., & Kennicutt, Jr., R. C. 2004, ARA&A, 42, 603

Krauss, L. M. 2011, Nuclear Physics B Proceedings Supplements, 221, 136

Kuijken, K., & Tremaine, S. 1991, in Dynamics of Disc Galaxies, ed. B. Sundelius, 71

Kwee, K. K., Muller, C. A., & Westerhout, G. 1954, Bull. Astron. Inst. Netherlands, 12, 211

Laskar, J. 1993, Physica D Nonlinear Phenomena, 67, 257

Lin, C. C., & Shu, F. H. 1964, ApJ, 140, 646

—. 1966, Proceedings of the National Academy of Science, 55, 229

Lindblad, B. 1927, MNRAS, 87, 553

Loebman, S. R., Roškar, R., Debattista, V. P., Ivezić, Ž., Quinn, T. R., & Wadsley, J. 2011, ApJ, 737, 8

López-Corredoira, M., Cabrera-Lavers, A., & Gerhard, O. E. 2005, A&A, 439, 107

López-Corredoira, M., Cabrera-Lavers, A., Mahoney, T. J., Hammersley, P. L., Garzón, F., & González-Fernández, C. 2007, AJ, 133, 154

Lynden-Bell, D., & Kalnajs, A. J. 1972, MNRAS, 157, 1

Lyngå, G. 1987, Publications of the Astronomical Institute of the Czechoslovak Academy of Sciences, 69, 121

Majaess, D. J., Turner, D. G., & Lane, D. J. 2009, MNRAS, 398, 263

Majewski, S. R. 2002, in IAU Symposium, Vol. 187, Cosmic Chemical Evolution, ed. K. Nomoto & J. W. Truran, 185–193

Marasco, A., Fraternali, F., & Binney, J. J. 2012, MNRAS, 419, 1107

Marinacci, F., Fraternali, F., Nipoti, C., Binney, J., Ciotti, L., & Londrillo, P. 2011, MNRAS, 415, 1534

Martig, M., Bournaud, F., Croton, D. J., Dekel, A., & Teyssier, R. 2012, ApJ, 756, 26

Martinez-Valpuesta, I., & Gerhard, O. 2011, ApJ, 734, L20

Mayer, L., Governato, F., & Kaufmann, T. 2008, Advanced Science Letters, 1, 7

Mayer, L., & Wadsley, J. 2004, MNRAS, 347, 277

Mayor, M. 1970, A&A, 6, 60

McCormmach, R. 2012, Weighing the World: The Reverend John Michell of Thornhill, Archimedes (Dordrecht) (Springer)

McMillan, P. J. 2011, MNRAS, 418, 1565

—. 2013, MNRAS, 430, 3276

Mestel, L. 1963, MNRAS, 126, 553

Minchev, I., Boily, C., Siebert, A., & Bienayme, O. 2010, MNRAS, 407, 2122

Minchev, I., Chiappini, C., & Martig, M. 2013a, A&A, 558, A9

—. 2013b, A&A, 558, A9

Minchev, I., Quillen, A. C., Williams, M., Freeman, K. C., Nordhaus, J., Siebert, A., & Bienaymé, O. 2009, MNRAS, 396, L56

Minniti, D., & Zoccali, M. 2008, in IAU Symposium, Vol. 245, IAU Symposium, ed. M. Bureau, E. Athanassoula, & B. Barbuy, 323–332

Miyamoto, M., & Nagai, R. 1975, PASJ, 27, 533

Mo, H. J., Mao, S., & White, S. D. M. 1998, MNRAS, 295, 319

Monari, G., Antoja, T., & Helmi, A. 2013, ArXiv e-prints

Montada, J. P. 2012, in The Stanford Encyclopedia of Philosophy, spring 2012 edn., ed. E. N. Zalta

Morrison, H. 1993, in Astronomical Society of the Pacific Conference Series, Vol. 48, The Globular Cluster-Galaxy Connection, ed. G. H. Smith & J. P. Brodie, 334

Mühlbauer, G., & Dehnen, W. 2003, A&A, 401, 975

Navarro, J. F., Frenk, C. S., & White, S. D. M. 1997, ApJ, 490, 493

Navarro, J. F., Helmi, A., & Freeman, K. C. 2004, ApJ, 601, L43

Ness, M., et al. 2013, MNRAS, 432, 2092

Newberg, H. J., et al. 2002, ApJ, 569, 245

Newton, I. 1687, Philosophiae naturalis principia mathematica (J. Societatis Regiae ac Typis J. Streater)

Noguchi, M. 1987, MNRAS, 228, 635

Nordström, B., et al. 2004, A&A, 418, 989

Ojha, D. K., Bienaymé, O., Mohan, V., & Robin, A. C. 1999, A&A, 351, 945

Oort, J. H. 1927, Bull. Astron. Inst. Netherlands, 3, 275

—. 1928, Bull. Astron. Inst. Netherlands, 4, 269

Oort, J. H., Kerr, F. J., & Westerhout, G. 1958, MNRAS, 118, 379

Perryman, M. A. C., & ESA, eds. 1997, ESA Special Publication, Vol. 1200, The HIPPARCOS and TYCHO catalogues. Astrometric and photometric star catalogues derived from the ESA HIPPARCOS Space Astrometry Mission

Pompéia, L., et al. 2011, MNRAS, 415, 1138

Press, W. H., Teukolsky, S. A., Vetterling, W. T., & Flannery, B. P. 1992, Numerical recipes in FORTRAN. The art of scientific computing

Proctor, R. A. 1869, MNRAS, 30, 50

Quillen, A. C. 2003, AJ, 125, 785

Quillen, A. C., Dougherty, J., Bagley, M. B., Minchev, I., & Comparetta, J. 2011, MNRAS, 417, 762

Quillen, A. C., & Garnett, D. R. 2000, ArXiv Astrophysics e-prints

Quillen, A. C., & Minchev, I. 2005, AJ, 130, 576

Quillen, A. C., Minchev, I., Bland-Hawthorn, J., & Haywood, M. 2009, MNRAS, 397, 1599

Quinn, P. J., Hernquist, L., & Fullagar, D. P. 1993, ApJ, 403, 74

Recio-Blanco, A., et al. 2014, ArXiv e-prints

Reid, M. J., & Brunthaler, A. 2004, ApJ, 616, 872

Reid, M. J., et al. 2014, ApJ, 783, 130

Renzini, A. 1999, in The Formation of Galactic Bulges, ed. C. M. Carollo, H. C. Ferguson, & R. F. G. Wyse, 9

Rix, H.-W., & Bovy, J. 2013, A&A Rev., 21, 61

Robin, A. C., et al. 2012, A&A, 543, A100

Robin, A. C., Reylé, C., Derrière, S., & Picaud, S. 2003, A&A, 409, 523

Roca-Fàbrega, S., Valenzuela, O., Figueras, F., Romero-Gómez, M., Velázquez, H., Antoja, T., & Pichardo, B. 2013, MNRAS, 432, 2878

Romano-Díaz, E., Shlosman, I., Heller, C., & Hoffman, Y. 2008, ApJ, 687, L13

Romero-Gómez, M., Athanassoula, E., Masdemont, J. J., & García-Gómez, C. 2007, A&A, 472, 63

Saha, K., Tseng, Y.-H., & Taam, R. E. 2010, ApJ, 721, 1878

Salaris, M., & Girardi, L. 2002, MNRAS, 337, 332

Salo, H. 1991, A&A, 243, 118

Sandage, A. R., & Eggen, O. J. 1959, MNRAS, 119, 278

Scannapieco, C., et al. 2012, MNRAS, 423, 1726

Schönrich, R., & Binney, J. 2009, MNRAS, 396, 203

Schönrich, R., Binney, J., & Dehnen, W. 2010, MNRAS, 403, 1829

Schwarzschild, K. 1907, Gottingen Nachrichten, 614, 13

Sellwood, J. A. 1985, MNRAS, 217, 127

—. 2010, MNRAS, 409, 145

—. 2014, Reviews of Modern Physics, 86, 1

Sellwood, J. A., & Carlberg, R. G. 2014, ApJ, 785, 137

Sellwood, J. A., & Evans, N. W. 2001, ApJ, 546, 176

Sellwood, J. A., & Moore, E. M. 1999, ApJ, 510, 125

Shapley, H. 1917, ApJ, 45, 118

Shapley, H., & Curtis, H. D. 1921, Bulletin of the National Research Council, Vol. 2, Part 3, No. 11, p. 171-217, 2, 171

Shapley, H., & Shapley, M. B. 1919, ApJ, 50, 42

Siebert, A., et al. 2012, MNRAS, 425, 2335

—. 2011a, MNRAS, 412, 2026

—. 2011b, AJ, 141, 187

Skibba, R. A., et al. 2012, MNRAS, 423, 1485

Skrutskie, M. F., et al. 2006, AJ, 131, 1163

Sofue, Y. 2012, PASJ, 64, 75

Solway, M., Sellwood, J. A., & Schönrich, R. 2012, MNRAS, 422, 1363

Spergel, D. N., Malhotra, S., & Blitz, L. 1996, in Spiral Galaxies in the Near-IR, ed. D. Minniti & H.-W. Rix, 128

Stanek, K. Z. 1995, ApJ, 441, L29

Stanek, K. Z., Mateo, M., Udalski, A., Szymanski, M., Kaluzny, J., & Kubiak, M. 1994, ApJ, 429, L73

Stanek, K. Z., Udalski, A., Szymanski, M., Kaluzny, J., Kubiak, M., Mateo, M., & Krzeminski, W. 1997, ApJ, 477, 163

Steinmetz, M., et al. 2006, AJ, 132, 1645

Stinson, G. S., Brook, C., Macciò, A. V., Wadsley, J., Quinn, T. R., & Couchman, H. M. P. 2013, MNRAS, 428, 129

Tissera, P. B., White, S. D. M., & Scannapieco, C. 2012, MNRAS, 420, 255

Toomre, A. 1964, ApJ, 139, 1217

Toomre, A. 1981, in Structure and Evolution of Normal Galaxies, ed. S. M. Fall & D. Lynden-Bell, 111–136

Trumpler, R. J. 1930, PASP, 42, 214

Vallée, J. P. 2008, AJ, 135, 1301

—. 2014, AJ, 148, 5

van de Hulst, H. C. 1945, Nederlands Tijdschrift voor Natuurkunde, 11, 210

van der Kruit, P., & van Berkel, K. 2001, The Legacy of J.C. Kapteyn: Studies on Kapteyn and the Development of Modern Astronomy, Astrophysics and Space Science Library (Springer Netherlands)

van der Kruit, P. C., & Searle, L. 1981, A&A, 95, 105

Vasiliev, E., & Athanassoula, E. 2012, MNRAS, 419, 3268

Villalobos, Á., & Helmi, A. 2008, MNRAS, 391, 1806

—. 2009, MNRAS, 399, 166

Weinberg, M. D. 1994, ApJ, 420, 597

Weinberg, M. D. 1996, in Astronomical Society of the Pacific Conference Series, Vol. 91, IAU Colloq. 157: Barred Galaxies, ed. R. Buta, D. A. Crocker, & B. G. Elmegreen, 516

Williams, M. E. K., Freeman, K. C., Helmi, A., & RAVE Collaboration. 2009, in IAU Symposium, Vol. 254, IAU Symposium, ed. J. Andersen, Nordströara, B. m, & J. Bland-Hawthorn, 139–144

Williams, M. E. K., et al. 2013, ArXiv e-prints

Wilson, M. L., et al. 2011, MNRAS, 413, 2235

Wright, T. 1750, An Original Theory Or New Hypothesis of the Universe, 1750: A Facsimile Reprint Together with the First Publication of A Theory of the Universe, 1734, History of science library (Macdonald & Co.).: Primary sources (Macdonald and Company)

Yanny, B., et al. 2009, AJ, 137, 4377

York, D. G., et al. 2000, AJ, 120, 1579

Zhao, H., & Mao, S. 1996, MNRAS, 283, 1197

Zhao, H., Rich, R. M., & Spergel, D. N. 1996, MNRAS, 282, 175

Zoccali, M., et al. 2003, A&A, 399, 931

Zwicky, F. 1937, ApJ, 86, 217

# Summary

## The Milky Way

The Milky Way is our Galaxy, the home to the Earth and the Sun. In the night sky, it appears as a band of feeble white light. It has taken thousands of years (at least from the time of the Ancient Greeks) to understand its nature, and to establish its main constituents and its global structure.

The white light of the Milky Way, which appeared to our ancestors as some sort of celestial fluid, is in fact due to a huge number (approximately 100 billion) of stars, so faint and so densely crowding the sky that the human eye cannot resolve them. Most of the stars in the Milky Way are organized in a highly flattened structure resembling a disk (the "Galactic disk"). Because of this highly flattened shape and Earth's position inside it, elemental geometrical intuition can be used to explain why the Milky Way appears as a band on the night sky.

Stars are not the only constituent of the Milky Way. Using telescopes capable to detect radio and infrared waves, it was discovered that the Milky Way is also composed of a large amount of gas and dust, mostly located in giant clouds in the disk. The need to explain the fast motions of stars and gas in the Milky Way (as well as in the other galaxies) has led astrophysicists to propose the existence of "dark matter" which would be responsible for most of the Milky Way's mass. Dark matter would interact with the normal matter only through gravity, which makes it extremely difficult to detect in any other way. In fact, no direct measurement of its properties has been made so far.

The Milky Way is enormous. The Galactic disk extends approximately $10,000$ parsecs (one "parsec" is approximately $30,000$ billion kilometers). The Sun is in its outskirts, at about $8,000 - 8,500$ parsecs from the center of the Galaxy. The Milky Way is kept together by the mutual gravitational attraction of its components. Stars, gas and dust move around its center and, for example, the Sun itself travels approximately 220 kilometers per second on a almost circular trajectory.

The Milky Way, however, is not the only one of its kind. With the help of telescopes, we can observe a great number of stellar systems with similar structures and dimensions, located at immense distances (millions of parsecs away). These stellar systems are called "disk galaxies" (the other important type of galaxies are the "elliptical galaxies"). In most of these disk galaxies, the light distribution is actually more complex and detailed

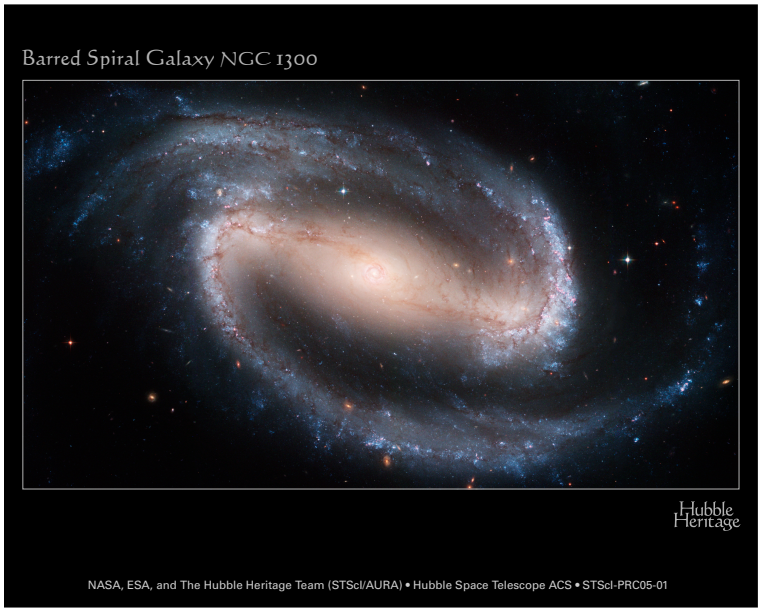


**Figure 1:** NGC1300. An example of disk galaxy with spiral arm and a prominent bar in the center.

observations reveal a number of features, such as a "bar" or "spiral arms" (or both, Fig. 1). Bars are overdensities of stars following a rod shape found in the center of at least 30% of disk galaxies, while spiral arms are formed by stars, gas and dust and extend across a great part of a disk. Both bars and spiral arms rotate around the centers of galaxies. However, while bars rotate "rigidly" (i.e., they do not get deformed by rotation) it is still unclear if spiral arms are long lived structures with a well defined rigid rotation, or transient features appearing and disappearing in the disk.

The Milky Way is similar to most disk galaxies, as it has a bar and spiral arms. However, we do not know much about their characteristics. For example, it is not clear how many spiral arms it has, the shape and mass of the bar, and how fast these structures rotate.

## Velocity of the stars near the Sun

Most of the stars of the Galactic disk move on trajectories that are almost circular and are concentrated inside a narrow layer of about 600 parsecs width around the plane of symmetry of the disk (the "Galactic plane"). These stars form the so-called "thin disk". A smaller fraction of the Galactic disk's stars (near the Sun about 10%) have somewhat different trajectories, more elongated (i.e. less circular) orbits and extend in a wide stratum of about 2,000 parsecs around the Galactic plane, called "thick disk"

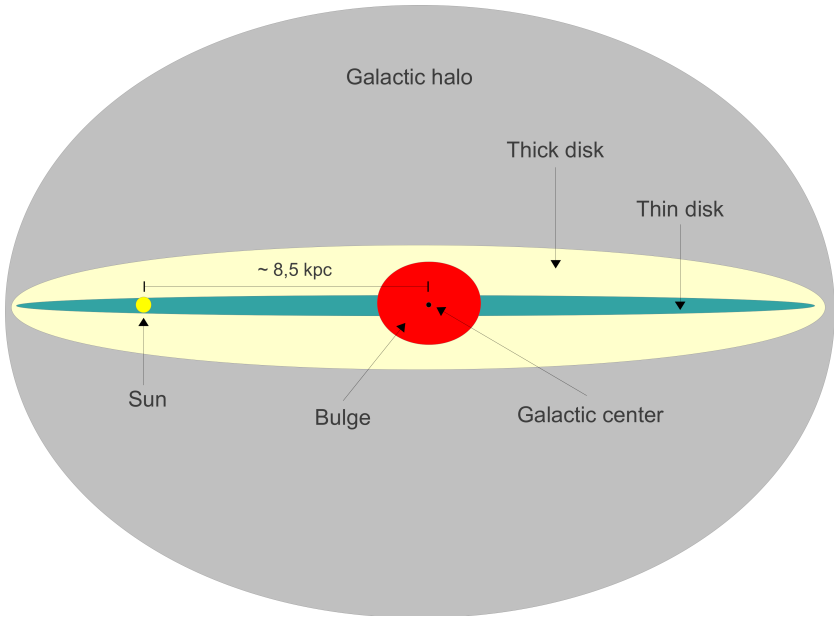


**Figure 2:** A sketch of the Milky Way's main components, with the Galactic disk seen edge on.

(Fig. 2). Because of the different trajectories, stars in the thin and thick disks travel also at different speeds. We characterize this difference in their velocity distribution through the "velocity dispersion" which measures how much variation there is with respect to the mean motion. Therefore, stars in the thin disk, which move in a more ordered way, have a lower velocity dispersion than those in the thick disk. The stars of the thin and thick disks also differ in their age and chemical composition (quantities that can be determined studying the light emitted, which is partially absorbed by the atmosphere of the stars themselves, depending on the type of star). In fact, the stars of the thick disk are on average much older than those of the thin disk and contain much less metals (e.g., chemical elements heavier than hydrogen and helium, such as iron).

The differences between thin and thick disks reveal a distinctness in the way they formed, which is still not completely clear. In our current understanding, the majority stars in the Milky Way's thin disk formed there, and the thin disk would be so narrow because the gas from which stars form was extremely flattened by its rotation combined with the fact that it can cool down and dissipate energy. However, part of the disk could have been thicker (if the gas had turbulent motions for example) in the early stages of its life or some of the thin disk's stars could have been affected by a mechanism that made possible the formation of the thick disk. This mechanism could perhaps have been triggered by the encounter and capture of a smaller galaxy by the Milky Way, or by some reorganization of the stars internal to the Milky Way (e.g., due to the bar and/or the spiral arms).

Independently of the way thin and thick disks formed, we find that the velocity distribution of many stars near the Sun is not smooth, but rather that they "congregate" in different groups, each of which moves in the Milky Way at the same speed (see e.g. Fig. 1.9 of this Thesis). These groups of stars are called "moving groups"[1].

The are several possible causes of the existence of moving groups near the Sun. The simplest hypothesis is that these stars formed together in the same gas cloud and travel at the speed they inherited from the cloud. This can explain the moving groups where the stars have approximately the same age. However, this cannot hold for many moving groups that are composed by stars with very different ages and chemical composition. An alternative mechanism for the formation of moving groups is called "resonant interaction" and is related to bar and spiral arms. This happens when the time that the stars employ to complete an orbit around the center of the Milky Way is similar to the period of rotation of bar or spiral arms: in this way the effects of the bar and spiral arms' gravitational attraction are amplified and groups of stars can be forced to travel at the same speed in the Milky Way. An example of this is the "Hercules moving group" which has been often associated with the resonant interaction between its stars and the Milky Way's bar.

## This Thesis

The resonant interaction between the bar and the Galactic disks has been studied so far only considering stars in the thin disk. However, it is interesting to check for possible effects of the bar on the stars in the thick disk, as the origin of moving groups in this component is usually associated with the destruction of small galaxies in the Milky Way (another process that leads to groups of stars that share the same velocity). This process of accretion or cannibalism is believed to have played a role in the formation of the Milky Way and hence it is important to determine how often this has happened in the past. Therefore, we want to clarify if the bar itself can create moving groups in the thick disk. This question is the main driver of this Thesis work.

In Chapter 2 we explore the ability of the bar to induce moving groups in the thin and thick disks of the Milky Way through resonant interaction. This study is carried out using computer programs able to calculate the trajectory of billions of particles, simulating the motion of stars under the influence of the Milky Way and bar's gravitational attractions. We choose the initial position and speed of the particles in our simulations to be similar to those measured for the thin and thick disks of the Milky Way, and study how the bar shapes their motions. We find that the bar's gravitational field affects the distribution of velocities of stars near the Sun, both in the thin and thick disks. In particular, the effect of the bar is to induce the appearance of two groups of stars near the Sun: one moves inwards and another one moves outwards in the Milky Way. These groups exist for both disks even at large distances from the Galactic plane.

In Chapter 3 we analyze in more detail how the bar's gravitational attraction influences the trajectories of stars. We classify the stars' orbits with a technique that calculates the times they need to complete one revolution around the center and oscillate in and out in the Milky Way (called "orbital periods", see Fig. 3). In particular, with

[1] Notice that while the stars in moving groups travel at the same speed, they are not necessarily placed at a small distances in space.

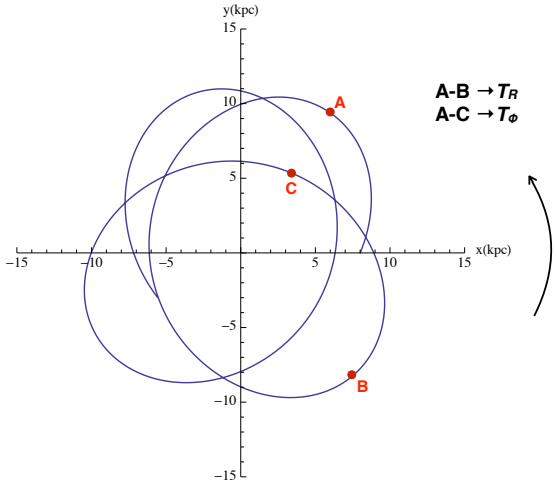


**Figure 3:** An example of orbit similar to those of the stars in the Milky Way's disk. It takes a time $T_\phi$ to the star to perform a complete rotation around the center of the Galaxy (e.g., from point A to point C) and a time $T_R$ (shorter thant $T_\phi$) to travel from its maximum distance from the center of the Galaxy ("apocenter") to its minimum distance ("pericenter") and again to the apocenter (e.g., from point A to point B). $T_R$ and $T_\phi$ are the orbital periods.

this technique we identify the stars that are most affected by the bar by looking at the ratios of their orbital periods. The simulations in Chapter 2, perhaps surprisingly, show that a similar fraction of the stars in the thin and thick disks are in resonance with the bar.

In Chapter 4, we compare the results of the simulations in Chapter 2 with recent observations of the speed of stars in the Galactic disk, at distances up to about $2,000$ parsecs from the Sun. These observations show how those disk stars that are closer to the Milky Way center tend to move outwards faster than those located at larger distances (giving rise to what we call a "radial velocity gradient"). Moreover, the stars' vertical speeds (i.e., directed perpendicular to the Galactic disk) also present trends, similar to compression and rarefaction waves ("vertical velocity gradient"). We find that the bar could be responsible for the radial velocity gradient. The mechanism that produces it is the same that leads to the creation of moving groups as described in Chapter 2. However, in our models the bar does not induce any vertical velocity gradient.

## The future of the Milky Way Astronomy: the *Gaia* satellite

On 19 December 2013 a Soyuz rocket was launched to space from Kourou, in French Guyana. This rocket carried on board the *Gaia* satellite that is now revolving around the Sun on a stationary orbit at 150, 000, 000 km from the Earth. The *Gaia* satellite is a space observatory controlled from Earth containing instruments whose main aim is the determination of the position and motions of the stars in the Milky Way. The greatest strength of *Gaia* is the so-called "astrometry', i.e., the accurate determination of the position of the stars in the sky and how they move with time. The aim of astrometry is to reconstruct the path on the sky of the stars, whence it is possible, to derive both the stars' distances ("parallaxes") and transversal velocities ("proper motions"). To perform this task the instruments have to be extremely precise and unaffected by the Earth's atmosphere, as the farther a star is, the smaller its parallax and proper motions become. To give an idea of *Gaia*'s instrumental precision the following example, taken from *Gaia*'s official website (`http://sci.esa.int/gaia/`), is illustrative: "for the brightest stars the goal is to measure their position in space to an accuracy equivalent to the size of a Euro coin on the Moon as seen from Earth".

*Gaia* is now starting its operations (the first data release is planned for mid 2016) and its results are expected to be a giant leap forward in our knowledge of the Milky Way. *Gaia* will measure the astrometry of about 1 billion stars of the Milky Way across the whole sky, producing catalogs of their positions and motions of the stars of unprecedented precision and completeness[2].

The positions and motions of the stars in the Milky Way represent the *Holy Grail* for those astrophysicists interested in understanding the Galaxy, because these are the main ingredients of the dynamical models. With *Gaia* and in the near future we will probably find the answers to many questions regarding the structure, mass and formation of the Milky Way. Such questions are related to more fundamental ones, like the existence and the nature of dark matter and the evolution of our Universe.

Our understanding of the main topics treated in this Thesis itself will surely benefit from the *Gaia* data. For example, we will be able to establish if the stars of the Hercules moving group are really due to the bar. With *Gaia* we will be able to measure with great precision the speed of stars even quite far from the Sun, and check if the variations in their motions with location in the Galaxy are compatible with the bar that is responsible for Hercules. A similar test can be attempted with the velocity gradients, as the extension and quality of data will probably be sufficient to recognize if such gradients are due to the bar, spiral arms or both. With *Gaia* we expect to finally shed light on the characteristics of the Milky Way's bar and spiral arms whose properties are, to date, still quite undetermined.

[2] However, the motions in the direction of the observer's line-of-sight will be measured only for roughly 15% of all observed stars.

# Nederlandse Samenvatting

## De Melkweg

De Melkweg is ons sterrenstelsel, het thuis van de Aarde en de Zon. Op de nachtelijke hemel verschijnt het als een band van zwak wit licht. Het heeft duizenden jaren gekost (ten minste sinds de tijd van de oude Grieken) om de aard ervan te begrijpen, om de belangrijkste bestanddelen en de globale structuur vast te stellen.

Het witte licht van de Melkweg, dat onze voorouders een soort hemelse vloeistof leek, komt in feite van een enorm aantal (circa 100 miljard) sterren, zo zwak en zo dicht opeen gepakt dat het menselijk oog ze niet van elkaar kan onderscheiden. Het merendeel van de sterren in de Melkweg is georganiseerd in een zeer platte structuur die gelijkenis met een schijf vertoont (de "Galactische schijf"). Door deze afgeplatte vorm en de positie van de Aarde erin, kan elementaire geometrische intuïtie verklaren waarom de Melkweg als een band op de nachtelijke hemel verschijnt.

Sterren zijn niet het enige bestanddeel van de Melkweg. Met telescopen die radio- en infraroodgolven kunnen detecteren, werd ontdekt dat de Melkweg ook uit een grote hoeveelheid gas en stof bestaat, meestal in de vorm van grote wolken in de schijf. De noodzaak om de snelle bewegingen van sterren en gas in de Melkweg (evenals in andere sterrenstelsels) te verklaren heeft astrofysici er toe geleid om ook het bestaan van "donkere materie" te opperen, welke verantwoordelijk zou zijn voor het grootste deel van de massa van de Melkweg. Donkere materie zou alleen op gewone materie door middel van de zwaartekracht inwerken, waardoor het zeer moeilijk te detecteren is. Het is een feit dat er tot nu toe geen directe metingen van de eigenschappen van de donkere materie zijn gedaan.

De Melkweg is enorm. De Galactische schijf strekt zich ongeveer $10,000$ parsecs uit (een "parsec" is ongeveer $30,000$ miljard kilometer). De Zon bevindt zich op ongeveer $8,000-8,500$ parsecs van het centrum van de Melkweg, in het buitengebied. De Melkweg wordt bij elkaar gehouden door de zwaartekracht van alle componenten. Sterren, gas en stof zich bewegen rond het middelpunt en de Zon zelf reist bijvoorbeeld ongeveer 220 kilometer per seconde op een bijna cirkelvormige baan.

De Melkweg is niet de enige in zijn soort. Dankzij telescopen kunnen we een groot aantal sterrenstelsels met soortgelijke structuren en afmetingen waarnemen, die op enorme afstanden (miljoenen parsecs) staan. Deze stellaire systemen worden "schijfsterrenstel-

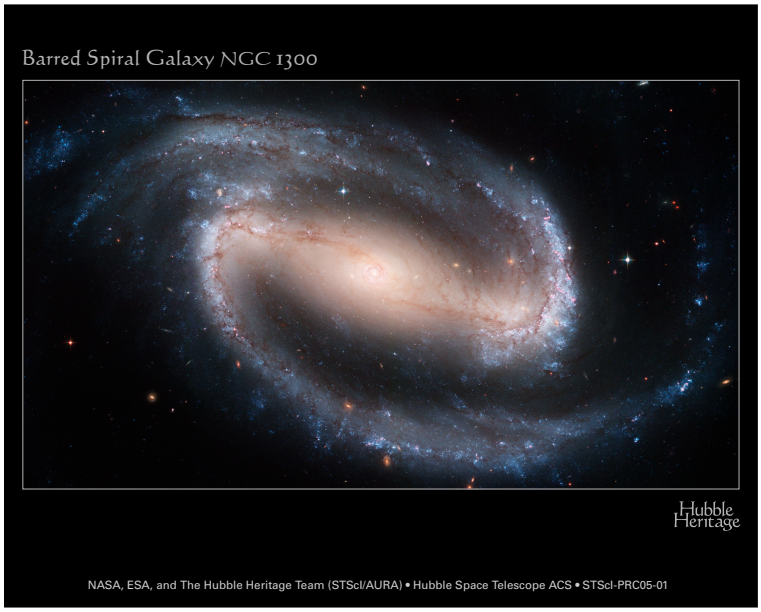


**Figuur 4:** NGC1300. Een voorbeeld van een schijfsterrenstelsel met spiraalarmen en een prominente balk in het centrum.

sels" genoemd (het andere belangrijke type sterrenstelsels zijn de "elliptische sterrenstelsels"). In de meeste schijfsterrenstelsels is de lichtverdeling eigenlijk complexer en uit gedetailleerde observaties blijkt dat er meerdere componenten zijn, zoals een "balk" of "spiraalarmen" (of beide, Fig. 4). Balken zijn verdikkingen van sterren in de vorm van een staaf die gevonden worden in de centra van bijna 30% van de schijfsterrenstelsels. Spiraalarmen worden gevormd door sterren, gas en stof en strekken zich uit over een groot deel van de schijf. Zowel balken als spiraalarmen draaien rond de centra van sterrenstelsels. Echter, terwijl balken "star" draaien (dat wil zeggen, ze vervormen niet door rotatie) is het nog steeds onduidelijk of spiraalarmen lang levende structuren zijn met een goed gedefinieerde starre rotatie, of vergankelijke entiteiten die verschijnen en verdwijnen in de schijf.

De Melkweg is vergelijkbaar met de meeste schijfsterrenstelsels, want het heeft een balk en spiraalarmen. Desondanks weten we niet veel over hun kenmerken. Het is bijvoorbeeld niet duidelijk hoeveel spiraalarmen de Melkweg heeft, wat de vorm en de massa van de balk is, en hoe snel deze structuren roteren.

## Snelheid van de sterren in de buurt van de Zon

De meeste sterren van de Galactische schijf bewegen zich voort op banen die bijna cirkelvormig zijn en die geconcentreerd zijn in een smalle laag van ongeveer 600 parsecs

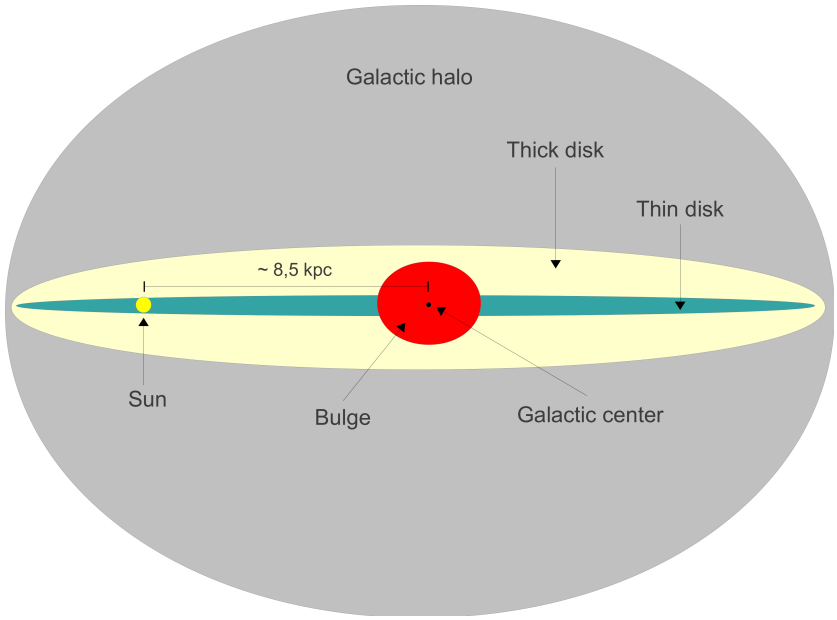


**Figuur 5:** Een schets van de belangrijkste onderdelen van de Melkweg, met de Galactische schijf gezien vanaf de zijkant.

dikte, rond het symmetrievlak van de Galactische schijf (het "Galacticsche vlak"). Deze sterren vormen de zogenaamde "dunne schijf". Een kleinere fractie van de sterren in de Galactische schijf (bijna 10% in de buurt van de Zon) hebben andere banen, meer langwerpige (dus minder cirkelvormige), en strekken zich uit in een brede laag van ongeveer 2,000 parsec rond het Galactische vlak, genaamd de "dikke schijf" (Fig. 5). Door hun verschillende banen, bewegen sterren in de dunne en dikke schijf met verschillende snelheden. Wij karakteriseren dit verschil in de verdeling van snelheden door middel van de "snelheidsdispersie" welke de hoeveelheid variatie meet ten opzichte van de gemiddelde snelheid. Sterren in de dunne schijf, die zich in een meer geordende manier bewegen, hebben een lagere snelheidsdispersie dan de sterren in de dikke schijf.

De sterren van de dunne en de dikke schijf verschillen ook in leeftijd en chemische samenstelling (welke kunnen worden bepaald door het bestuderen van het licht opgestraald, dat gedeeltelijk kan worden geabsorbeert door de atmosferen van de sterren zelf, afhankelijk van het type ster). Sterren van de dikke schijf zijn gemiddeld ouder dan die van de dunne schijf en bevatten veel minder metalen (chemische elementen zwaarder dan waterstof en helium, zoals bijvoorbeeld ijzer).

De verschillen tussen de dunne en dikke schijf laten zien dat er een verschil is in de manier waarop deze gevormd werden, dat nog steeds niet volledig duidelijk is. Met onze huidige kennis denken we dat de meeste sterren in de dunne schijf van de Melkweg ook daar gevormd werden, en dat de dunne schijf zo dun is omdat het gas waaruit de sterren waren gemaakt zeer afgeplat was door rotatie gecombineerd met het feit dat gas kan

afkoelen en energie verliezen. Echter, een deel van de schijf zou dikker geweest kunnen zijn in de vroege stadia van zijn bestaan (bijvoorbeeld in het geval dat het gas turbulente bewegingen had) of een deel van de sterren van de dunne schijf zou beïnvloed kunnen zijn door een mechanisme dat de vorming van de dikke schijf mogelijk zou maken. Dit mechanisme zou misschien veroorzaakt kunnen zijn door de botsing en vangst van een kleiner sterrenstelsel door de Melkweg, of door een reorganisatie van de sterren binnen de Melkweg zelf (bijvoorbeeld als gevolg van de invloed van de balk en/of de spiraalarmen).

Los van de manier waarop dunne en dikke schijf gevormd werden, zien we dat de snelheidsverdeling van veel sterren in de buurt van de Zon niet glad is, maar dat deze "klonteren" in verschillende groepen, die elke met eenzelfde snelheid in de Melkweg beweegt (zie bijvoorbeeld Fig. 1.9 van dit Proefschrift). Deze groepen van sterren worden "bewegende groepen" genoemd[3].

Er zijn verschillende mogelijke oorzaken voor het bestaan van de bewegende groepen in de buurt van de Zon. De meest envoudige hypothese is dat deze sterren samen zijn gevormd in dezelfde gaswolk en hun snelheid van deze gaswolk hebben geërfd. Dit kan de bewegende groepen verklaren waarbij de sterren ongeveer dezelfde leeftijd hebben. Dit kan echter niet gelden voor veel bewegende groepen die uit sterren met zeer verschillende leeftijden en chemische samenstellingen bestaan. Een alternatief mechanisme voor de vorming van bewegende groepen noemen we "resonante interactie" en is gerelateerd aan de balk en de spiraalarmen. Dit gebeurt wanneer de omlooptijd van de sterren in hun baan rond het centrum van de Melkweg vergelijkbaar is met de rotatieperiode van de balk of de spiraalarmen: in dat geval worden de effecten van de aantrekkingskracht van de balk en de spiraalarmen versterkt en kunnen groepen van sterren worden gedwongen om met dezelfde snelheid in de Melkweg te reizen. Een voorbeeld hiervan is de "Hercules bewegende groep" welke vaak geassocieerd wordt met de resonante interactie tussen de sterren en de balk van de Melkweg.

## Dit Proefschrift

De resonante interactie tussen de balk en de Galactische schijven is tot nu toe alleen onderzocht door naar de dunne schijf te kijken. Het is echter interessant om te kijken naar mogelijke effecten van de balk op de sterren in de dikke schijf, aangezien de oorsprong van groepen in dit component meestal wordt geassocieerd met de vernietiging van kleine sterrenstelsels in de Melkweg (een ander proces dat leidt tot groepen van sterren die dezelfde snelheid delen). Dit proces van aanwas of kannibalisme wordt verondersteld een rol te hebben gespeeld in de vorming van de Melkweg en daarom is het belangrijk om te bepalen hoe vaak dit in het verleden is gebeurd. Daarom willen wij onderzoeken of de balk zelf groepen kan maken in de dikke schijf. Deze vraag is de belangrijkste motivatie voor dit Proefschrift.

In Hoofdstuk 2 onderzoeken we de mogelijkheden van de balk om door resonante interactie bewegende groepen te creëren in de dunne en dikke schijven van de Melkweg. Dit onderzoek wordt uitgevoerd met behulp van computerprogramma's die de banen van miljarden deeltjes kunnen berekenen, en zo de bewegingen van sterren onder de invloed van de zwaartekracht van de Melkweg en de balk simuleren. We kiezen de initiële positie

[3] Merk op dat hoewel de sterren in bewegende groepen reizen met dezelfde snelheid, deze zich niet noodzakelijk dicht bij elkaar hoeven te bevinden

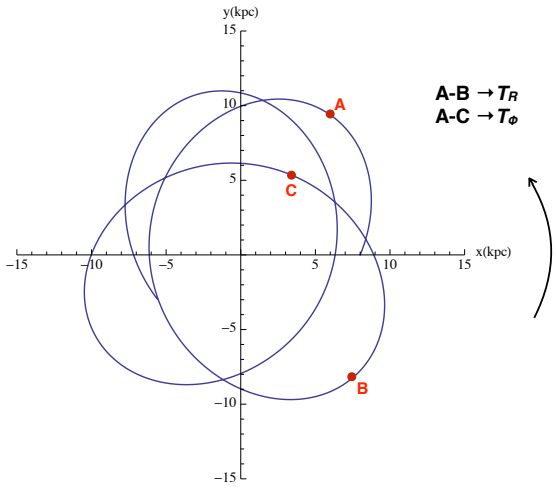


**Figuur 6:** Een voorbeeld van een baan vergelijkbaar met die van de sterren in de schijf van de Melkweg. Het kost de ster een tijd $T_\phi$ om een volledige omwenteling rond het centrum van de Melkweg uit te voeren (bijvoorbeeld van punt A naar punt C) en een tijd $T_R$ (korter dan $T_\phi$) om van de maximale afstand van het centrum van de Melkweg ("apofocus") naar de minimale afstand ("perifocus") en terug naar apofocus (bijvoorbeeld van punt A naar punt B) te reizen. $T_R$ en $T_\phi$ zijn de omlooptijden.

en snelheid van de deeltjes in onze simulaties in overeenkomst met gemeten waarden voor de dunne en dikke schijf van de Melkweg en we bestuderen hoe de balk hun bewegingen verandert. We vinden dat het zwaartekrachtsveld van de balk de snelheidsdistributie van de sterren in de buurt van de Zon beïnvloedt, zowel in de dunne als dikke schijf. De balk veroorzaakt met name het ontstaan van twee groepen van sterren in de buurt van de Zon: één die naar binnen beweegt, en een andere die naar buiten beweegt in de Melkweg. Deze groepen bestaan in beide schijven, zelfs op grote afstand van het Galactische vlak. In Hoofdstuk 3 analyseren we in meer detail hoe de zwaartekracht van de balk de banen van sterren beïnvloedt. We classificeren de banen van de sterren met een techniek die de tijd berekent die ze nodig hebben om een omwenteling rond het centrum te maken en de tijd die ze nodig hebben om naar binnen en naar buiten in de Melkweg te oscilleren (deze zijn genaamd "omlooptijden", zie Fig. 6). Voornamelijk met deze techniek identificeren we de sterren die het meest beïnvloed zijn door de balk, door te kijken naar de verhoudingen van hun omlooptijden. De simulaties in Hoofdstuk 2 tonen, wellicht verrassend, dat vergelijkbare fracties van de sterren in de dunne en dikke

schijf in resonantie zijn met de balk.

In Hoofdstuk 4 vergelijken we de resultaten van de simulaties in Hoofdstuk 2 met recente metingen van de snelheden van sterren in de Galactische schijf, op afstanden tot ongeveer 2,000 parsec van de Zon. Deze observaties laten zien hoe de sterren van de schijf die zich dichter bij het centrum van de Melkweg bevinden meestal sneller bewegen dan die op grotere afstand (wat aanleiding geeft tot wat we een "radiale snelheidsgradiënt" noemen). Bovendien, de verticale snelheden van de sterren (loodrecht gericht op de Galactische schijf) laten ook een trend zien, vergelijkbaar met compressie- en verdunningsgolven ("verticale snelheidsgradiënt"). Wij laten zien dat de balk verantwoordelijk kan zijn voor de radiale snelheidsgradiënt. Het mechanisme dat dit produceert is hetzelfde als dat wat leidt tot het ontstaan van de bewegende groepen, zoals beschreven in Hoofdstuk 2. In onze modellen veroorzaakt de balk echter geen verticale snelheidsgradiënt.

## De toekomst van Sterrenkunde met de Melkweg: de *Gaia* satelliet

Op 19 december 2013 werd vanuit Kourou, in Frans Guyana, een Soyuz raket de ruimte in gelanceerd. Deze raket had de *Gaia* satelliet aan boord, die nu rond de Zon draait in een stationaire baan op 150,000,000 km vanaf de Aarde. De *Gaia* satelliet is een ruimteobservatorium bestuurd vanaf de Aarde met instrumenten waarvan het belangrijkste doel is het bepalen van de positie en de bewegingen van de sterren in de Melkweg. De grootste kracht van *Gaia* is de zogenaamde "astrometrie", dat wil zeggen, de nauwkeurige bepaling van de stand van de sterren aan de hemel en hoe deze bewegen met de tijd. Het doel van astrometrie is om het pad van sterren aan de hemel te reconstruëren, waarmee het mogelijk is om zowel afstanden ("parallaxen") als transversale snelheden ("eigenbewegingen") van de sterren te bepalen. Om dit te doen, moeten de instrumenten uiterst precies zijn en niet worden beïnvloed door de atmosfeer van de Aarde, aangezien hoe verder weg een ster staat, hoe kleiner de parallax en de eigenbewegingen worden. Om een idee te geven van de instrumentale precisie van *Gaia*, hebben we het volgende voorbeeld, genomen van de officiële website van *Gaia* (`http://sci.esa.int/gaia/`), ter illustratie: "voor de helderste sterren is het doel om hun positie in de ruimte te meten met een nauwkeurigheid welke even groot is als een Euro-muntstuk op de Maan gezien vanaf de Aarde".

*Gaia* begint nu zijn activiteiten (de eerste gegevens worden mid-2016 uitgebracht) en er wordt verwacht dat de resultaten een grote sprong voorwaarts zullen zijn in onze kennis over de Melkweg. *Gaia* zal de astrometrie van ongeveer 1 miljard sterren van de Melkweg over de hele hemel meten, waarbij het catalogi van de posities en bewegingen van deze sterren zal produceren met ongekende precisie en volledigheid[4].

De posities en bewegingen van de sterren in de Melkweg vertegenwoordigen de *Heilige Graal* voor de astrofysici die geïnteresseerd zijn in het begrijpen van de Melkweg, omdat dit de belangrijkste ingrediënten zijn van de dynamische modellen. Met *Gaia*, en in de nabije toekomst, zullen we waarschijnlijk de antwoorden op veel vragen over de structuur, massa en de vorming van de Melkweg vinden. Deze vragen zijn gerelateerd aan meer

[4] De bewegingen in de richting van de waarnemer zullen maar voor ongeveer 15% van alle waargenomen sterren worden gemeten.

fundamentele vraagstukken, zoals het bestaan en de aard van donkere materie en de evolutie van ons heelal.

Ons begrip van de belangrijkste onderwerpen behandeld in dit Proefschrift zal zeker profiteren van de gegevens van *Gaia*. We zullen bijvoorbeeld vast kunnen stellen of de Hercules bewegende groep door de balk veroorzaakt wordt. Met *Gaia* zullen we met grote precisie de snelheid van de sterren kunnen meten, zelfs vrij ver weg van de Zon, en zo kunnen controleren of de variaties in bewegingen met de locatie in de Melkweg verenigbaar zijn met een model waar de balk verantwoordelijk is voor Hercules. Eenzelfde test kan met de snelheidsgradiënten worden getracht, want de omvang en kwaliteit van de data zal waarschijnlijk voldoende zijn om te herkennen of die gradiënten door de balk, de spiraalarmen of beide veroorzaakt worden. Met *Gaia* verwachten we eindelijk licht te werpen op de karakteristieken van de balk en de spiraalarmen van de Melkweg, eigenschappen die zelfs vandaag de dag nog erg onzeker zijn.

# Acknowledgements

*L'attimo della dolce angoscia fuggiva, oh, che altro può fare un attimo? ma il succedente gli succedeva: l'integrale dei fuggenti attimi è l'ora.*

C.E. Gadda

I start by acknowledging the person that first conceived this Thesis: my Promoter Prof. dr. Amina Helmi. Amina, thank you for your decision to allocate part of your ERC grant in this interesting project and to choose me for its completion. Thank you also for the remarkable amount of time and care you dedicated to it. It was a honor to work with you and hopefully there will be more occasions in the future. I am impressed by the quantity and quality of your work, even in quite different topics. Once you told me that Tim de Zeeuw told you that Martin Schwarzschild told him, that problems should be tackled "starting where the gradient of difficulty is steeper". I think this phrase best describes the way you face work.

A huge part of this work owes to my Copromoter, Dr. Teresa Antoja. Teresa, thank you for all the time you spent for this project. You have always been gentle and, since the first time we met, I wished I could work with you. When your office was still in Groningen, the Kapteyn Institute's floors were consumed by a continuous procession, when yours truly was looking for you eager for advice. Sorry for all the precious time you had to waste for me. Despite this you never ceased to be a good friend. It was a pleasure to work with you: you are a talented astronomer and I wish we will have many more collaborations in the future.

My gratitude goes also to the European Research Council for founding this project, and to all those who financed it directly or indirectly. Moreover, thanks to the Rijksuniversiteit Groningen, the city of Groningen and the Netherlands for their hospitality in the last four years.

I wish to thank the reading committee of this Thesis, Prof. dr. Piet van der Kruit, Prof. dr. Koen Kuijken, and Prof. dr. Marc Verheijen, for carefully reading this Thesis and for their precious comments. I consider the rare privilege of having three important astronomers reading my work a special accomplishment in itself.

This Thesis greatly benefited from the help and advice of a number of astronomers. I wish to thank Prof. dr. Matthias Steinmetz who contributed to the realization of

Chapter 4, Dr. Mary Williams that kindly provided part of the data used in Chapter 4 and Dr. Hugo Buddelmeijer for the density estimator code used in Chapters 2 and 4. During these four years I had several stimulating discussions with experts in the field of dynamics. Particularly interesting were those with Prof. dr. James Binney, Prof. dr. Benoit Famaey, Prof. dr. Francesca Figueras, Dr. Ivan Minchev, Dr. Arnaud Siebert, and Dr. Eugene Vasiliev. Prof. dr. Francesca Figueras and the *Gaia* group were very welcoming during my stay at the Barcelona University in July 2014. Many thanks also to my former advisor Prof. dr. Luca Ciotti. A special mention goes also to Prof. dr. Mariano Mendez and Dr. Kyle Westfall for filling many gaps in my knowledge of Statistics.

Amina should also be praised for assembling a team of astronomers of remarkable quality (the *Galactica* group). I have never been in a room discussing with so many smart and talented people at the same time, as in our Thursday's meetings. Carlos, Else, Facundo, Hans, Hao, Kyle, Laura, Maarten, Pim, Robyn, Shoko, Tjitske, I have learned a lot from you all. You have been exceptional colleagues and friends. Whenever in need, I could pass from your offices or send you an email and find you ready to leave whatever you were doing to listen to me. I already understood this back in 2009, when I had to decide whether my PhD would have been in Groningen or in Leiden: this group for sure made Groningen particularly attractive. I would have many nice stories to mention about each of you, but I have to leave it now to our memories. A special *dank jullie vriendelijk* goes to Maarten and Tjitske for gracefully accepting to correct my *Samenvatting*. Maarten, you are a good friend and a genuine talent for Physics, I wish you a great future together with your newly forming family. Tjitske, because of your good nature, intelligence and tact it is always nice to have something to do with you. Plus, you and Maarten are excellent ice skaters.

This work would not have been possible without the help of the administrative and technical staff of the Kapteyn Astronomical Institute, especially Wim Zwitser and Eite Tiesinga for what concerns the computational support.

The working environment of the Kapteyn Astronomical Institute is one of the nicest I have ever seen. I have already mentioned my research group. I would also like to thank my office mates Fabian, Guido, Guobao, Jeffrey, and Sander, always helpful and friendly. Moreover, I would like to thank several other colleagues for their pleasant company and friendship, especially Andrea, Antonino, Beth, Burcu, Davide, Federico, Filippo, Francesco, Gergő, Katinka, Laura, Marisa, Mark, Mustafa, Anastasia, Patrick, Silvia, Stefano, Wouter, Yanping. With some of you I literally "measured my life with coffee spoons", as T.S. Eliot wrote. Burcu and Katinka, your Thesis defense will be only few days after mine and I wish you the best of the luck with it. Very interesting was also the time I spent in the corridors chatting with Prof. dr. Renzo Sancisi, about several topics, sometimes even Astronomy.

A warm embrace goes also to all my friends outside the Kapteyn Institute. In particular to those that I met in the parish of the *Jozefkathedraal*: thanks to Pastoor Wagenaar, to Andrea, Anne-Silvie, Christina, David, Gosia, Hania, Katarina, Klara, Kurian, Luca, Lucia, Lucia, Luise, Maciek, Magda, Marysia, Mathilde, Olga, Paweł, Thomas, and Yves-Sean. Paweł, *dziękuję bardzo* for many things, but one in particular. *Hartelijk bedankt* to all the *koorleiden*, with whom I enjoyed singing in the last two years, in particular to the *dirgent/organist* Sjoerd, the *voorzitter* Ben and the fellow *bassen* Anton, Leo, and Menno. Thanks to my housemates and neighbors, in particular to Katja. Thanks to Ger-

ard and Liesbeth that found the first apartment where I have lived in Groningen. Thanks to all the fellow tennis players at the *ACLO* sport center, and in particular to Estelle, that also read and corrected some mistakes in the Summary of this Thesis. Thanks to Gosia and Basia, that (together with Ewa) read and suggested me some changes in the *Samenvatting*. *Grazie* Nicola for your hospitality every time I came to Leiden.

Finally, *grazie mille* to my Family for all the love, material and moral comfort they give me, in the moments of joy and pain. To my Mother and Father, to my Brother (also for the creation of the beautiful cover of this Thesis), to my Grandparents. And to *moja ukochana dziewczyna, lily na polu,* Ewa.

Giacomo Monari
Barcelona/Porretta Terme, August 2014